



## 저작자표시-비영리-변경금지 2.0 대한민국

이용자는 아래의 조건을 따르는 경우에 한하여 자유롭게

- 이 저작물을 복제, 배포, 전송, 전시, 공연 및 방송할 수 있습니다.

다음과 같은 조건을 따라야 합니다:



저작자표시. 귀하는 원저작자를 표시하여야 합니다.



비영리. 귀하는 이 저작물을 영리 목적으로 이용할 수 없습니다.



변경금지. 귀하는 이 저작물을 개작, 변형 또는 가공할 수 없습니다.

- 귀하는, 이 저작물의 재이용이나 배포의 경우, 이 저작물에 적용된 이용허락조건을 명확하게 나타내어야 합니다.
- 저작권자로부터 별도의 허가를 받으면 이러한 조건들은 적용되지 않습니다.

저작권법에 따른 이용자의 권리는 위의 내용에 의하여 영향을 받지 않습니다.

이것은 [이용허락규약\(Legal Code\)](#)을 이해하기 쉽게 요약한 것입니다.

[Disclaimer](#)

**Thesis for a Ph. D. Degree**

**Stratospheric sudden warming and  
its predictability modulated by  
tropical sea surface temperature variability**

**적도 해수면 온도 변동성에 의해 조절되는  
성층권 돌연승온 및 그에 따른 예측성**

**February 2021**

**School of Earth and Environmental Sciences**

**Graduate School**

**Seoul National University**

**Kanghyun Song**

**Stratospheric sudden warming and  
its predictability modulated by  
tropical sea surface temperature variability**

**By  
Kanghyun Song**

**A Dissertation submitted to the Faculty of the  
Graduate School of the Seoul National University  
in partial fulfillment of the requirements  
for the Degree of Doctor of Philosophy**

**Degree Awarded:  
December 2020**

**Advisory committee:**

**Professor Wookap Choi, Chair  
Professor Seok-Woo Son, Advisor  
Professor Baek-Min Kim  
Professor Joowan Kim  
Professor Andrew Charlton-Perez**

**Stratospheric sudden warming and  
its predictability modulated by  
tropical sea surface temperature variability**

적도 해수면 온도 변동성에 의해 조절되는  
성층권 돌연승온 및 그에 따른 예측성

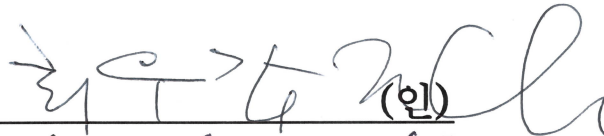
지도교수 손 석 우

이 논문을 이학박사 학위논문으로 제출함  
2020년 12월

서울대학교 대학원  
지구환경과학부  
송 강 현

송강현의 이학박사 학위논문을 인준함  
2020년 12월

위 원 장

 (인)

부위원장

손 석 우 (인)

위 원

김 백 민 (인)

위 원

김 주 완 (인)

위 원

Andrew Charlton-Perce (인) 

## **Abstract**

This study examines that the role of the El Niño/Southern Oscillation (ENSO) in the stratospheric sudden warming (SSW) events in both the Northern Hemisphere (NH) and the Southern Hemisphere (SH). The NH SSW events occur favorably only during El Niño winters, not La Niña winters, which is a contrast result from the literature. The SSW frequency during La Niña winters is quite dependent on the choice of SSW definitions, and this has been changed on the decadal timescale. The nonstationary relationship during La Niña winters is not the result of satellite data assimilation or interannual-to-decadal variability, such as Pacific decadal oscillation. It could result from SSW or ENSO internal variability. The SH SSW events, which are detected only twice in the historical records from 1958, can also be modulated by ENSO. Especially, the second SH SSW event in 2019 is under dramatic interannual conditions such as a record-breaking Indian ocean dipole (IOD), easterly phase of quasi-biennial oscillation (QBO), and central Pacific El Niño. Among those interannual variabilities, ENSO is the strongest driver for the 2019 SH SSW event in the cold-SST model experiments. In these experiments, we reduce or remove the anomalous sea surface temperature or atmospheric initial conditions from the observational data, especially over the IOD, QBO, and ENSO locations. The central Pacific El Niño amplifies the tropospheric wave activity with enhanced South Pacific high

anomalies, explained by the teleconnection modulation. The above results in both the NH and SH SSW events suggest that the ENSO is one of the key drivers to modulate the stratospheric extreme. This relationship is applied to the subseasonal-to-seasonal (S2S) prediction of SSW events in the NH, aiming to improve the stratospheric and tropospheric prediction skills. However, this study with Global/Regional Integrated Model systems cannot find any significant improvement in the prediction skills with respect to the different ENSO phases. It is not found in other interannual variabilities, such as QBO or SSW type. As a result, this study finds that the key role of ENSO in both the NH and SH SSW event. The possibility of SSW events in both hemispheres is increased during El Niño winters. However, this relationship does not hold for the SSW prediction in the S2S timescale.

**Keywords:** stratospheric sudden warming event, El Niño/Southern Oscillation, subseasonal-to-seasonal prediction

**Student number:** 2016-30115

# Table of Contents

<b>Abstract .....</b>	<b>i</b>
<b>Table of Contents .....</b>	<b>iii</b>
<b>List of Tables .....</b>	<b>v</b>
<b>List of Figures.....</b>	<b>vi</b>
<b>1. Introduction .....</b>	<b>1</b>
<b>2. Data, methods, and model .....</b>	<b>8</b>
<b>2.1. Data .....</b>	<b>8</b>
<b>2.2. SSW, ENSO, PDO, and QBO detections .....</b>	<b>10</b>
<b>2.3. GRIMs description.....</b>	<b>18</b>
<b>2.4. Experimental design .....</b>	<b>20</b>
<b>2.5. Evaluation metrics .....</b>	<b>24</b>
<b>2.6. S2S operational models.....</b>	<b>29</b>
<b>3. Role of ENSO in the NH SSW event .....</b>	<b>30</b>
<b>3.1. SSW frequency for ENSO phase .....</b>	<b>30</b>
<b>3.2. Sensitivity test for the ENSO-SSW relationship .....</b>	<b>42</b>
<b>3.3. Decadal changes in the ENSO-SSW relationship .....</b>	<b>44</b>
<b>4. Role of ENSO in the SH SSW event .....</b>	<b>53</b>
<b>4.1. 2019 SH SSW event.....</b>	<b>53</b>
<b>4.2. Key driver of the 2019 SH SSW event .....</b>	<b>59</b>
<b>5. Role of ENSO in the NH SSW predictability .....</b>	<b>71</b>
<b>5.1. Model mean biases of GRIMs .....</b>	<b>71</b>

5.2. SSW prediction .....	75
6. Summary and discussion.....	97
References.....	102
국문초록 .....	112
감사의 글 .....	114



## **List of Tables**

Table 1. Definitions of SSW used in this study.

Table 2. Definitions of ENSO used in this study.

Table 3. The SSW events examined in this study and their prediction skills. The SSW type is denoted in the third and fourth columns with “D” for the displacement and “S” for the split event. In the fifth column, the background state is indicated by “EN” for the El Niño, “LN” for the La Niña, and “NE” for the neutral winter. The QBO phases are denoted with “EQBO” for the easterly QBO and “WQBO” for the westerly QBO winters. The prediction skill is defined as the maximum forecast lead time when a reversal of the 10-hPa zonal-mean zonal wind at 60°N ([U10]) is detected, or when MSSS of 10-hPa geopotential height over 35°-90°N is greater than zero.

Table 4. Experiment designs.

Table 5. Mean and standard deviation of SSW prediction skills (unit: day). The numbers in parenthesis denote the number of SSW events for each SSW type and the background state.

Table 6. Same as Table 5 but for four SSW types.

## List of Figures

- Figure 1. (a) Initial zonal-mean zonal wind ( $[U]$ ) [unit:  $\text{m s}^{-1}$ ] and (b-d) sea surface temperature (SST) [unit: K] for  $\tau=18$  forecast. The initial and boundary conditions for CTL are indicated by the contour. The difference between sensitivity experiments (NoQBO, ColdSST, ColdInd, and ColdPac) and CTL is shaded. Contour intervals are 10.
- Figure 2. (a) Standard deviation of geopotential height anomaly during December-February and (b) its zonal mean. Green lines denote the reference latitude of  $35^\circ\text{N}$ . The Gaussian curve is gray.
- Figure 3. Latitudinal profile of 10-hPa zonal-mean zonal wind anomalies during El Niño, La Niña, and ENSO-neutral winters: (a) seasonal-mean and (b) daily standard deviation. As described in section 2, NNR and CPC ENSO index are used here.
- Figure 4. (a) Number of SSW events and (b) its frequency during El Niño, ENSO-neutral, and La Niña winters. In (b), the values that are statistically significant at the 90% and 95% confidence levels are denoted with one and two asterisks, respectively. NNR and CPC ENSO index are used. See the text for the details.
- Figure 5. Temporal evolution of 10-hPa zonal-mean zonal wind at (a)  $60^\circ\text{N}$  and (b)  $65^\circ\text{N}$  during El Niño winters. Only the winters when SSW events are detected by the U65 definition but not by the U60 definition are considered. The onset date of each SSW event is denoted by X mark.
- Figure 6. Temporal evolution of (left) 10-hPa zonal-mean zonal wind and (right) 100-hPa eddy heat flux during U65 SSW events for (top) El Niño, (middle) La Niña winters, and (bottom) their differences. The values that are significantly different from long-term climatology at the 95% confidence level are shaded. Zero wind line is indicated by red contour in the left column. The reference latitudes of  $60^\circ\text{N}$  and  $65^\circ\text{N}$ , and SSW onset date are indicated by horizontal and vertical lines, respectively.
- Figure 7. Latitudinal profile of 100-hPa eddy heat flux integrated from lag -15 day to the onset of U65 SSW events for (a) El Niño, (b) La Niña winters, and (c) their difference. Heat fluxes of zonal-wavenumber one ( $k=1$ ) and two ( $k=2$ ) waves are denoted with dashed and dotted lines, respectively. The reference latitudes of  $60^\circ\text{N}$  and  $65^\circ\text{N}$  are indicated by a horizontal

line.

Figure 8. SSW frequency during ENSO winters in (a) NNR and (b) JRA-55 datasets. Two different SSW definitions, i.e., U60 and U65 definitions, and three different ENSO indices, i.e., CPC, SIMPLE and CPCv5, are applied. Note that SSW statistics for NNR and CPC ENSO index (left box of a) are identical to those in Fig. 4b.

Figure 9. (a) 31-years SSW frequency and (b) SSW number during ENSO winters for JRA-55 (dotted) and ERA20C (solid). The blue and red indicate El Niño and La Niña winters, respectively.

Figure 10. 21-years SSW frequency during ENSO winters for JRA-55C (dotted) and JRA-55 (solid). The blue and red indicate El Niño and La Niña winters, respectively.

Figure 11. Correlation between polar-cap averaged geopotential height (PCI) at 10 hPa and SST over the Pacific Ocean for (a) JRA-55 and (b) ERA20C. The boxes indicate the area of NPSST index and ENSO index.

Figure 12. (a) SSW frequency, (b) SSW number, and (c) NPSST winters during NPSST winters in JRA-55 (dotted) and ERA20 (solid). The blue and red lines indicate the  $-NPSST$  and  $+NPSST$  winters, respectively.

Figure 13. Scatter plot between DJF-mean  $NI\tilde{N}O3.4$  index and PDO index for JRA-55 dataset from 1958 to 2018. Open circle indicates the SSW winters.

Figure 14. Temporal evolution of (a) 10-hPa zonal-mean zonal wind ( $[U10]$ ) at  $50^\circ S$ , (b) polar-cap (south of  $60^\circ S$ ) averaged geopotential height ( $Z$ ) anomaly, and (c) vertical component of zonal-mean wave activity flux ( $Fz$ ) at 100 hPa averaged over  $45^\circ-75^\circ S$ . The vertical lines indicate the 2019 SSW onset. Spatial distribution of time-mean (d) 100-hPa  $Fz$  [unit:  $m^2 s^{-2}$ ], (e) 200-hPa  $Z$  [unit: m], and (f) vertical structure of  $Z$  averaged over  $45^\circ-75^\circ S$  [unit: m]. The time average is conducted from 20 days before (lag -20) to the SSW onset (lag 0). (e, f) Climatological and anomalous  $Z$  are indicated by the shading and the contour, respectively.

Figure 15. (a) Zonal-mean zonal wind ( $[U]$ ) [unit:  $m s^{-1}$ ] and (b) sea-surface temperature (SST) anomaly [unit: K] in August, 2019. (c)  $[U10]$  anomaly, (d) IOD, (e)  $NI\tilde{N}O4$  timeseries in August. Each index is

obtained from the red line and boxes in (a,b). The dashed lines in (c–e) indicate the range of each standard deviation.

Figure 16. Temporal evolution of zonal-mean zonal wind at 10 hPa ( $[U10]$ ) averaged over  $40^{\circ}$ – $60^{\circ}$ S for (a) S2S models and GRIMs. (b) Same as (a) but for GRIMs experiments. (c) MSSS evolution is shown for six different GRIMs experiments. All forecasts are initialized on August 29, 2019 except for JMA model, which provides only the forecast on August 28, 2019. See the legend for the color information. Black lines indicate the reference from JRA-55. The vertical line indicates the SSW onset.

Figure 17. (a) Polar-cap averaged geopotential height ( $Z$ ), (b) MSSS, (c) zonal-mean MSE, and (d) eddy MSE at 10 hPa. All variables are averaged for  $\pm 3$  days with respect to the SSW onset. The zonal-mean and eddy MSE are normalized. The different colors denote the six experiments. Black horizontal lines in (a,b) are the reference values, JRA-55 and MSSS=0, respectively. The vertical dotted line indicates  $\tau=16$ . The lag indicates the days in advance of the SSW onset.

Figure 18. The vertical component of 3-D wave flux ( $F_z$ ) at (a) 100 and (b) 200 hPa averaged over  $45^{\circ}$ – $75^{\circ}$ S from 10 days before to the SSW onset in  $\tau=16$  forecast. Black line is JRA-55. The meaning of colors is the same as other Figures.

Figure 19. Climatological (shading) and anomalous (contour) geopotential height ( $Z$ ) at 200 hPa averaged from 10 days before to the SSW onset in  $\tau=16$  forecast. The variable is a deviation from the zonal mean. The model results for six different experiments are denoted as green contours. Black contours indicate JRA-55.

Figure 20. Same as Fig. 19 but for vertical structure of geopotential height ( $Z$ ) averaged over  $45^{\circ}$ – $75^{\circ}$ S.

Figure 21. Zonal mean zonal wind ( $[U]$ ) biases at (a) 10-day and (b) 20-day ensemble forecast in CTR runs. The shading denotes  $[U]$  differences between GRIMs and JRA-55. 100-hPa EPz at (c) 10-day and (d) 20-day ensemble forecast in control runs and JRA-55 are shown as solid and dotted lines, respectively.

Figure 22. Area mean biases over  $35$ – $90^{\circ}$ N (a, c) without and (b, d) with the bias correction for all simulations. The top and bottom panels show 10-hPa

and 850-hPa geopotential height biases, respectively.

Figure 23. Time evolution of (a) 10-hPa zonal-mean zonal wind at 60°N ([U10]) and (c) MSSS of 10-hPa geopotential height over 35°N-90°N for the 2008 SSW event. The forecasts at different lead times are denoted with different colors (see the labels on the right of the middle panel). The observed [U10] is shown in thick black lines in (a). Note that MSSS for the maximum lead time of successful forecast is denoted with open circles, while that for the minimum lead time for the unsuccessful forecast is denoted with crosses. (e) Two-dimensional MSSS with a prediction skill in a horizontal line. The thick contour indicates the zero line of MSSS. (b,d,f) Same as (a,c,e) but for the 1989 SSW event. In all panels, the vertical lines denote the SSW onset.

Figure 24. (a) MSE normalized by  $\overline{\text{MSE}_0}$  for the 2008 SSW event and (c,e) its zonal-mean and eddy components. In all panels, a solid black contour indicates the line of  $\text{MSE}/\overline{\text{MSE}_0}=1$ , corresponding to  $\text{MSSS}=0$ . (b,d,f) Same as (a,c,e) but for the 1989 SSW event.

Figure 25. Same as Fig. 24f, but for the eddy-phase and eddy-amplitude errors and (b,d) for the eddy errors by the zonal-wavenumber one and two.

Figure 26. (a) The vertical component of 3-D wave activity flux at 100 hPa (Fz100) averaged over 45°N-75°N during the 1989 SSW event. Colored lines and symbols are the same as Fig. 23b (i.e., open circle and cross for  $\tau=10$  and  $\tau=11$  forecasts, respectively). (b) Fz100 averaged over 45°N-75°N, and (c) 10-days averaged Fz100 right before the onset from JRA-55. The shading in (b) denotes the Fz100 differences between  $\tau=11$  and  $\tau=10$  forecasts.

Figure 27. Relationship between (a) the zonal-mean and eddy errors, (c) the eddy-phase and eddy-amplitude errors, and (e) the zonal-wavenumber one and two for the top six SSW events. Event number, indicated in different symbols, corresponds to the one in Table 3. (b,d,f) Same as (a,c,e) but for the bottom six SSW events. The forecasts at different lead times are denoted in purple and blue. See the Figure legend.

Figure 28. (a,d) Vertical structure of MSSS in  $\tau=10$  and  $\tau=23$  forecasts with a function of forecast day (j) for the 2008 SSW event, (b,e) for the 1989 SSW event, and (c,f) their differences. The green line denotes  $\text{MSSS}=0$ . The missing values are shaded in gray. The vertical lines denote the SSW

onset.

Figure 29. Vertical structure of MSSS as a function of forecast day ( $j$ ) for (a) the successful (HIT) and (b) unsuccessful SSW predictions (MISS). Their difference is shown in (c). Green lines in (a,b) MSSS=0, and the shading in (c) denotes the value that is statistically significant at the 95% confidence level.

Figure 30. Same as Fig. 29, but for the MSE decomposition into (a-c) the zonal-mean and (d-f) eddy components. The eddy components by (g-i) zonal wavenumber one and two.

# 1. Introduction

The polar stratosphere is dominated by a strong westerly wind during the winter that forms in autumn and decays in spring. This stratospheric wind is modulated by both the physical and dynamical processes. Normally, the mean state of the polar vortex is related to the seasonal cycle of solar radiation. The absence of solar energy at the polar stratosphere induces the strong meridional gradient of air temperature at the subpolar region. This temperature gradient is balanced to the vertical zonal wind shear, so-called a thermal wind balance, resulting in the westerly wind. This counter-clockwise circumpolar wind is called the polar vortex or the polar night jet.

The polar vortex variability is generally dominated by the dynamical process, especially wave dynamics. The polar vortex is occasionally broken, accompanying an erupt increase of the polar temperature. The temperature rises to about 40 K only for two weeks. This dramatic event is named stratospheric sudden warming (SSW). The SSW event is firstly uncovered by a radiosonde observation in the 1950s (See the SSW history in Butler et al. 2015). Since that, it has been revealed that the SSW dynamics and its influences on both the stratosphere and the troposphere. The SSW events are modulated by the planetary-scale waves from the troposphere into the stratosphere. The important role of the planetary-scale

waves in SSW events is generally agreed in the literature, but its development is still controversial. Among two main explanations, the first concerns the role of the tropospheric wave sources (e.g., Matsuno 1971). The second focuses on the modulation of low stratospheric state in wave development, as wave resonance condition (e.g., Tung and Lindzen 1979). The former is mainly accepted for various SSW studies. The present study is also based on this first explanation.

Although driven by the tropospheric waves, SSW events significantly impact the underlying tropospheric circulation anomalies for up to two months in the Northern Hemisphere (NH). For the NH SSW events, the surface temperature and the tropospheric circulation responses are explained by the negative northern annular mode (NAM). For instance, the eddy-driven jet moves to the equator, and the storm tracks are also shifted to the equator during the negative NAM (e.g., Baldwin and Dunkerton 2001).

The SSW events, caused by the planetary-scale waves from the troposphere, can be affected by the large-scale phenomena at the troposphere, such as El Niño-Southern Oscillation (ENSO), which is the dominant interannual variability in the tropics (Horel and Wallace 1981; van Loon and Labitzke 1987). More precisely, the mean state of the polar vortex in NH becomes anomalously weak during El Niño winters, while it is strong during La Niña winters (van Loon and Labitzke 1987; Manzini et al. 2006; Calvo et al. 2008; Iza et al. 2016). However, the above



relationship does not hold for subseasonal variability of the NH polar vortex, such as the SSW event. Some studies found that the SSW events occur more frequently during El Niño and La Niña winters than during ENSO-neutral winters [Butler and Polvani 2011 (BP11); Butler et al. 2014 (BPD14)].

The ENSO-SSW relationship documented in BP11, however, is somewhat questionable. Polvani et al. (2017) recently reported that while the increased SSW events during El Niño winters are robust, relative changes of SSW events during La Niña winters are dependent on the choice of sea surface temperature (SST) dataset. Modeling studies also do not support the ENSO-SSW relationship in the literature. Taguchi and Hartmann (2006) reported that SSW events occur twice more frequently during El Niño winters than during La Niña winters in their model simulation, although the model underestimated the stratospheric variability. To better understand the ENSO-SSW relationship in NH, part 1 of the present study revisits the SSW statistics in long-term reanalysis datasets. Specifically, seven different definitions of SSW, which have been used in the literature, are adopted for two different reanalysis and SST datasets. Furthermore, the decadal changes in the ENSO-SSW relationships are investigated by using the same dataset and additionally extended reanalysis dataset.

Most SSW events are observed in NH, and they occur approximately once per year or every two years (e.g., Butler et al. 2015; Song and Son 2018).

Compared to the NH, the polar vortex variability is relatively weak in the Southern Hemisphere (SH). Although weak, the polar vortex variability in the austral spring can significantly affect the tropospheric circulation and weather conditions, such as hot and dry extremes in Australia (Lim et al. 2018, 2019) and Antarctic sea-ice variability (Wang et al. 2019). As extreme stratospheric events in the NH, a major SSW event in the SH was observed in 2002 for the first time in the observational record (e.g., Baldwin et al. 2003). This dramatic event was driven by a burst of strong planetary-scale waves in the stratosphere. The amplified wave in the stratosphere likely results from a self-tuned resonance in the stratosphere (e.g., Esler et al. 2006) or an upward-propagating wave from the troposphere (e.g., Nishii and Nakamura 2004). The former suggests the important role of the stratospheric mean state in the 2002 SSW event, while the latter argues that tropospheric forcing, associated with blocking high over the South Atlantic Ocean, led to the SSW event.

Since the first SSW event in 2002, a record-high temperature in the Antarctic stratosphere has been observed once again in 2019 from late August to early September (Lim et al. 2020a). Compared to the SSW event in the NH and the 2002 SSW event in the SH, this event accompanied the polar vortex break at relatively low latitudes (Rao et al. 2020); for instance, zonal-mean zonal wind at 50°S turns easterly from the westerly direction but not at 60°S. This polar vortex weakening

is partly explained by the accumulated wave activity in the stratosphere from the troposphere (Lim et al. 2020a). A robust downward influence on the 2019 SSW event was observed from late October to the end of December. This downward coupling promoted a negative Southern Annular Mode in the troposphere, followed by precipitation and surface air temperature variabilities across the SH (Lim et al. 2020a,b). It was further discovered that the effects of the 2019 SSW event are not limited to the troposphere but also extend into the ionosphere (Yamazaki et al. 2020).

The key driver of the 2019 SSW event has not been clarified, although some possible factors are investigated (Shen et al. 2020). The vertically propagating waves responsible for the 2019 SSW event in the SH could have been generated and modulated by several atmospheric and oceanic conditions in 2019. August-September 2019 is characterized by the easterly phase of the quasi-biennial oscillation (QBO) in the stratosphere, the record-high Indian Ocean Dipole (IOD), and the central Pacific El Niño-like sea surface temperature (SST) anomaly (Rao et al. 2020). It has been documented that the easterly phase of the QBO (EQBO) condition could lead to vortex displacement in zonal wavenumber one. Similarly, high and low anomalies over the South Pacific and Indian Oceans, resulting from the positive IOD and warm SST over the central Pacific, could enhance the vertically propagating planetary-scale waves in the SH. Based on these relations,

Rao et al. (2020) evaluated the prediction skill of the 2019 SSW events by the operational models participating in the subseasonal-to-seasonal (S2S) prediction project. Although the possible role of stratospheric and tropospheric conditions is suggested, the main driver of the SSW event remains to be determined. This is revealed in part 2 of this study by using the global forecast model.

The SSW downward influences are often maintained for up to two months in the extratropics. As such, SSW has been regarded as one of the potential sources to improve S2S timescale prediction (Vitart et al. 2017). The S2S timescale prediction is recently concerned for the seamless prediction (Hoskins 2013), but SSW prediction was already considered as a potential source for improved tropospheric prediction in the literature. With the SSW prediction limit from 2 days to a month (Tripathi et al. 2015a; Song et al. 2020), previous studies indeed uncovered that the tropospheric prediction skills are improved when SSW events are organized at the stratosphere (Sigmond et al. 2013; Tripathi et al. 2015b).

The prediction skills of the NH SSW events are possibly dominated by the interannual variability, such as ENSO, because it can modulate the SSW occurrence. However, the possible impact of ENSO in the SSW prediction skills has not been examined in the literature. In part 3 of this study, the SSW prediction skills are evaluated by using the global forecast model, and it is further investigated for different ENSO winters. Additionally, this study considers the

prediction skills for different QBO phases, which is another interannual variability in the stratospheric tropics.

## **2. Data, methods, and model**

### **2.1. Data**

Japanese 55-year Reanalysis (Kobayashi et al. 2015; hereafter JRA-55) is the one of long-record datasets covering the period from the pre-satellite era to the recent. In this dataset, many kinds of observational data are assimilated such as conventional surface observation, aircraft observation, and satellite observation. The JRA-55 dataset contains the periods of both no satellite data before 1972 (pre-satellite era) and abundant satellite data after 1979. This inhomogeneity has been a problem in using a long-term reanalysis dataset. In order to provide a more time-consistent dataset, Japan Meteorological Agency launched a project aiming to produce a reanalysis dataset without satellite data assimilation after 1972. The project is named JRA-55 conventional (Kobayashi et al. 2014; hereafter JRA-55C). The JRA-55C has exactly the same data assimilation system as JRA-55, but the satellite dataset is not included in JRA-55C. Because of the period of the satellite dataset, JRA-55C starts in November 1972 ending in December 2012. The JRA-55 and JRA-55C datasets are used for the basic-statistical analysis as well as SSW definition. In the investigation of decadal changes in the ENSO-SSW relationship, a long-term reanalysis dataset is further used. It is the European Centre for Medium-range Weather Forecasts (ECMWF)'s first atmospheric reanalysis of the

20th century from 1900-2010 (hereafter ERA20C) (Poli et al. 2013).

For ENSO, the Extended Reconstructed Sea Surface Temperature version 3b and 5b (ERSSTv3 and ERSSTv5) data (Smith et al. 2008; Huang et al. 2017) from the National Oceanic and Atmospheric Administration (NOAA)/Climate Prediction Center (CPC) are used. The ERSSTv5 is a monthly sea surface temperature dataset in the globe taken from the International Comprehensive Ocean-Atmosphere Dataset (ICOADS).

## 2.2. SSW, ENSO, PDO, and QBO detections

Various definitions of SSW have been used in the literature (Butler et al. 2015; Martineau and Son 2015; Palmeiro et al. 2015). As summarized in Table 1, SSW has been identified by using the zonal-mean zonal wind at a selected latitude, the area-averaged zonal wind or geopotential height, the leading mode of variability, or the combination of multiple variables. Although 10 hPa is the most common level, 50 hPa or even 100 hPa has also been used to quantify polar vortex variability. The most widely-used definitions, i.e., the so-called World Meteorological Organization (WMO) definition and its simplified version (Charlton and Polvani 2007), are based on 10-hPa zonal-mean zonal wind reversal at 60°N. Since 60°N does not necessarily represent the edge of the polar vortex, zonal-mean zonal wind at 65°N (Butler et al. 2015) or at any latitude from 55°N to 70°N has also been used (Palmeiro et al. 2015).

Following Butler et al. (2015), seven different SSW definitions, which include the one used in BP11 and BPD14 (i.e., U60 definition), are considered in this study (Table 1). They are WMO, U60, U65, U6090, Z6090, EOF, and 2DM definitions. Here the WMO, U60, Z6090, and 2DM definitions are identical to the U&T, CP07, ZPOL, and MOM definitions in Butler et al. (2015), respectively. The detected SSW events for each definition are listed in Table ES2 of Butler et al. (2015). An exception is the U60 SSW event on January 7, 1968. This event is



excluded in this study because it is not detected as the SSW event in the latest version of NNR [personal communication with A. H. Butler; see also the footnote posted on page 3 of Butler et al. (2014)].

Both the WMO and U60 definitions consider the reversal of zonal-mean zonal wind at 60°N and 10 hPa. Although the former has an additional constraint of the meridional temperature gradient change, these two definitions exhibit similar frequency and onset date of SSW events. The U65 and U6090 definitions are similar to the U60 definition but use the zonal-mean zonal wind at 65°N and area-averaged zonal wind over 60-90°N, respectively. The Z6090 definition utilizes polar-cap geopotential height anomaly. Unlike other definitions, the EOFU definition employs a statistical method. In this definition, the onset of SSW is detected by using the leading mode of extratropical variability of zonal-mean zonal wind at 50 hPa. The last definition, 2DM, is based on two-dimensional moment diagnostics. Specifically, it detects SSW events by computing an aspect ratio and centroid latitude of the polar vortex in 10-hPa geopotential height fields. Since this definition focuses on the morphology of the polar vortex, it may not be directly compared with other definitions that are based on zonal-mean diagnostics.

It should be noted that the number of SSW events differs substantially among the definitions (Table 1). While the U6090 definition detects the largest number of SSW events (37), the EOFU definition detects the smallest number of SSW events

(26). When only 10-hPa definitions are considered (i.e., the first five definitions in Table 1), the WMO definition shows a minimum SSW frequency.

For evaluation of SSW prediction, we consider only mid-winter (December to February) SSW events to avoid final warming events. The SSW events are defined as following CP07. For the analysis period for the winters from 1979/80-2011/12, a total of 18 mid-winter SSW events are detected, as listed in Table 3. The evaluation is conducted after the pre-satellite era (before 1980) because of the possible effect of satellite data inhomogeneity. They are listed in Table 3 with the background state in terms of ENSO and QBO phase.

The SSW events can be classified into two types, i.e., vortex-displacement (D) and vortex-split (S) SSW events. Displacement events are characterized by the polar vortex shifting toward low latitudes, while split events show the polar vortex dividing into two daughter vortices (e.g., CP07). The former events are associated with zonal wavenumber one ( $k=1$ ) wave activities, but the latter events show zonal wavenumber two ( $k=2$ ) waves that amplify immediately before the SSW events. Here, the SSW classification is based on the diagnosis from CP07, defining S and D types by using potential vorticity and its gradient. Furthermore, the SSW events are classified into four types (DD, DS, SS, and SD) based on their evolution before and after the SSW onset date (Choi et al. 2019; hereafter CKC19).

The ENSO is determined by the NIÑO-3.4 index (i.e., SST anomaly averaged over 5°N-5°S and 170°-120°W). To objectively define its phase, two thresholds are adopted (Table 2). First, NCEP/CPC convention, referred to as the CPC definition, is used as in BPD14. Specifically, El Niño and La Niña winters are defined as the winters when the seasonal-running mean NIÑO-3.4 index consecutively surpasses  $\pm 0.5$  K for at least five seasons. Other winters are simply set to the ENSO-neutral winters. A total of 19 and 18 winters are identified as El Niño and La Niña winters, respectively. If ERSSTv5 is used (CPCv5), 20 El Niño and 18 La Niña winters are identified. Second, ENSO is also simply defined by the seasonal-mean NIÑO-3.4 index from November to March (NDJFM). In this definition, referred to as the SIMPLE definition, El Niño and La Niña winters are defined when the NDJFM-averaged NIÑO-3.4 index surpasses  $\pm 0.5$  K as in BP11. This definition results in somewhat different ENSO winters from the CPC definition. A total of 16 and 20 winters are identified as El Niño and La Niña winters, respectively.

The CPC definition for the ERSSTv3b data is set as the reference in this study. The SIMPLE definition is used to test the sensitivity of SSW statistics to the ENSO definition. Although not shown, different threshold values (e.g.,  $\pm 0.6$  K and  $\pm 0.7$  K) are also tested for both CPC and SIMPLE definitions. It turns out that the overall results are not sensitive to the threshold values [BP11; see also Taguchi

(2015)]. Note that the ENSO winters in an evaluation of SSW prediction in GRIMs are based on NCEP/CPC convention for ERSSTv5 from 1980 to 2012.

To identify PDO winters without empirical orthogonal function (EOF) statistics, North Pacific SST (NPSST) is calculated. It is based on area-averaged SST over the mid-latitude where the maximum correlation is found between the polar vortex variability and SST during the boreal winters. The positive and negative NPSST winters are defined when DJF-mean NPSST  $\geq 0.5$  std. and  $\leq -0.5$  std., respectively. Although not shown, the NPSST index is highly correlated with the PDO index ( $r \sim 0.9$ ).

The QBO winters are determined by the sign of the 50-hPa zonal wind during the boreal winters (Naujokat 1986). The selected SSW events are well distributed between the two phases of ENSO and QBO. A total of six and nine SSW events are detected during El Niño and La Niña winters, respectively. Likewise, nine SSW events are identified during EQBO and WQBO winters.

Table 1. Definitions of SSW used in this study.

SSW definition (# of the detected events)	Description
WMO (33)	SSW is detected when the zonal-mean zonal wind at 60°N and 10 hPa drops below 0 m s <sup>-1</sup> . The event that does not show a reversal of meridional temperature gradient within 10 days of a wind reversal is excluded (e.g., Kruger et al. 2005).
U60 (35)	Same as the WMO definition except for no consideration of temperature gradient change (e.g., Charlton and Polvani 2007).
U65 (44)	Same as U60 except for zonal-mean zonal wind reversal at 65°N (e.g., Butler et al. 2015).
U6090 (46)	Same as U60 except for polar-cap (60-90°N) averaged zonal wind reversal (e.g., Butler et al. 2015).
Z6090 (37)	SSW is detected when geopotential height anomaly averaged over 60-90°N at 10 hPa exceeds three standard deviations of January-February-March (JFM) mean (e.g., Thompson et al. 2002).
EOFU (26)	SSW is detected when the principal component of the leading Empirical Orthogonal Function (EOF) of zonal-mean zonal wind over 20-90°N at 50 hPa decreases below minus three standard deviations (e.g., Limpasuvan et al. 2004).
2DM (28)	SSW is detected by calculating an aspect ratio and a centroid latitude of two-dimensional vortex moment from 10-hPa geopotential height (e.g., Seviour et al. 2013).

Table 2. Definitions of ENSO used in this study.

ENSO definition	Description
CPC	ENSO is detected when seasonal-running mean NIÑO3.4 index consecutively surpasses $\pm 0.5$ K for at least five seasons, following NCEP/CPC convention.
SIMPLE	ENSO is detected when NDJFM-mean NIÑO3.4 index surpasses $\pm 0.5$ K.

Table 3. The SSW events examined in this study and their prediction skills. The SSW type is denoted in the third and fourth columns with “D” for the displacement and “S” for the split event. In the fifth column, the background state is indicated by “EN” for the El Niño, “LN” for the La Niña, and “NE” for the neutral winter. The QBO phases are denoted with “EQBO” for the easterly QBO and “WQBO” for the westerly QBO winters. The prediction skill is defined as the maximum forecast lead time when a reversal of the 10-hPa zonal-mean zonal wind at 60°N ([U10]) is detected, or when MSSS of 10-hPa geopotential height over 35°-90°N is greater than zero.

SSW events	Onset date	SSW type		Background state	Prediction skill	
		CP07	CKC19		wind reversal	MSSS ( $\geq 0$ )
1	29 FEB 1980	D	DD	EN, EQBO	14 days	15 days
2	04 DEC 1981	D	DD	NE, EQBO	12 days	14 days
3	24 FEB 1984	D	DD	LN, WQBO	12 days	12 days
4	01 JAN 1985	S	SS	LN, EQBO	6 days	10 days
5	23 JAN 1987	D	DD	EN, WQBO	11 days	19 days
6	08 DEC 1987	S	DS	EN, WQBO	4 days	16 days
7	21 FEB 1989	S	SS	LN, WQBO	3 days	10 days
8	15 DEC 1998	D	DS	LN, EQBO	10 days	18 days
9	26 FEB 1999	S	DD	LN, EQBO	11 days	11 days
10	11 FEB 2001	S	DS	LN, WQBO	7 days	19 days
11	31 DEC 2001	D	DD	NE, EQBO	8 days	21 days
12	18 JAN 2003	S	DS	EN, WQBO	2 days	15 days
13	05 JAN 2004	D	DD	NE, EQBO	13 days	15 days
14	21 JAN 2006	S	DD	LN, EQBO	6 days	17 days
15	24 FEB 2007	D	SD	EN, WQBO	6 days	12 days
16	22 FEB 2008	D	DD	LN, EQBO	20 days	23 days
17	24 JAN 2009	S	SS	LN, WQBO	10 days	12 days
18	09 FEB 2010	S	DS	EN, WQBO	7 days	15 days

### 2.3. GRIMs description

The Global/Regional Integrated Model system (GRIMs; Hong et al. 2013), which is the operational model of the Republic of Korea Air Force, is used in this study. This model is a hydrostatic spectral atmospheric model aiming to provide both short-term weather forecasts and climate predictions on global and regional scales. The standard physics packages described in Hong et al. (2013) are used. These packages consist of the short-wave and long-wave radiation schemes, WRF single-moment class 1 microphysics scheme, simplified Arakawa-Schubert convection scheme, gravity wave drag by orography and convection, and YSU boundary layer scheme. The diurnal variation in sea surface temperature is also taken into account by incorporating an ocean mixed layer and a surface energy budget for skin temperature. See Hong et al. (2013) for details. The model resolution is set to T126 with 64 hybrid sigma-pressure levels (Koo and Hong 2013). The model top is 0.3 hPa.

All input data are obtained from JRA-55. The three-dimensional geopotential height, zonal wind, meridional wind, air temperature, and specific humidity at  $2.5^{\circ} \times 2.5^{\circ}$  horizontal resolution are used for model initializations. The boundary conditions consist of sea surface temperature, sea ice concentration, and water-equivalent of accumulated snow depth at a  $1.25^{\circ} \times 1.25^{\circ}$  horizontal resolution. More details on the model and its initialization are also described in Hong et al.



(2013).

For each SSW event, the model is initialized every day, starting 25 days before the SSW onset (forecast lead time  $\tau=25$  day) to the onset ( $\tau=0$  day), and integrated for 30 days. In other words, a total of 26 initializations are utilized. A simple time-lagged ensemble forecast is conducted with five different starting times (i.e., 00 UTC,  $\pm 06$  UTC, and  $\pm 12$  UTC). For instance, the ensemble forecast initialized on 5 January 2004 has five ensemble members that consist of realizations at 12 UTC on 4 January ( $-12$  hours), 18 UTC on 4 January ( $-6$  hours), 00 UTC on 5 January (0 hour), 06 UTC on 5 January ( $+6$  hours), and 12 UTC on 5 January ( $+12$  hours). These five members are simply averaged to obtain the ensemble-mean forecast. Only the daily-averaged ensemble-mean forecasts (hereafter the forecasts) are examined. Note that the GRIMs results in part 2 are based on a single ensemble member.

## 2.4. Experimental design

The model experiments are designed to examine a key driver(s) of the 2019 SSW event. The six experiments are particularly set with different initial and/or boundary conditions. They are CTL, NoQBO, ColdSST, ColdInd, ColdPac, and ColdSST+NoQBO experiments (Table 4). The control experiment, CTL, simply uses the JRA-55 initial and boundary conditions. The NoQBO experiment is the same as the CTL experiment except that the QBO-related zonal-mean initial conditions are removed from the zonal-mean of each initial condition. The QBO-related signals are obtained by linear regression of the zonal-mean variables in August against an equatorial zonal-mean zonal wind at 10 hPa from 1958 to 2019. The zonal wind of NoQBO initial condition is shown in Fig. 1a along with the CTL initial condition. The EQBO in the tropical stratosphere and the related signals in the extratropical stratosphere are linearly removed from the initial condition (shading in Fig. 1a). Although not shown, the same procedure is applied to other variables. The sensitivity tests to SST are carried out in the ColdSST, ColdInd, and ColdPac experiments (Table 4). In the ColdSST experiment, reduced SST is prescribed. As shown in Fig. 1b, reduced SST is colder than the observed SST on the globe. Two other SST-sensitivity experiments, referred to as ColdInd (Fig. 1c) and ColdPac (Fig. 1d), are further conducted to verify the influence of the SST over the Indian and the Pacific Oceans, selected over 130°E-80°W and

60°-100°E for the south of 20°N, respectively. Lastly, the combined effect of NoQBO initial and ColdSST boundary conditions is tested in ColdSST+NoQBO.

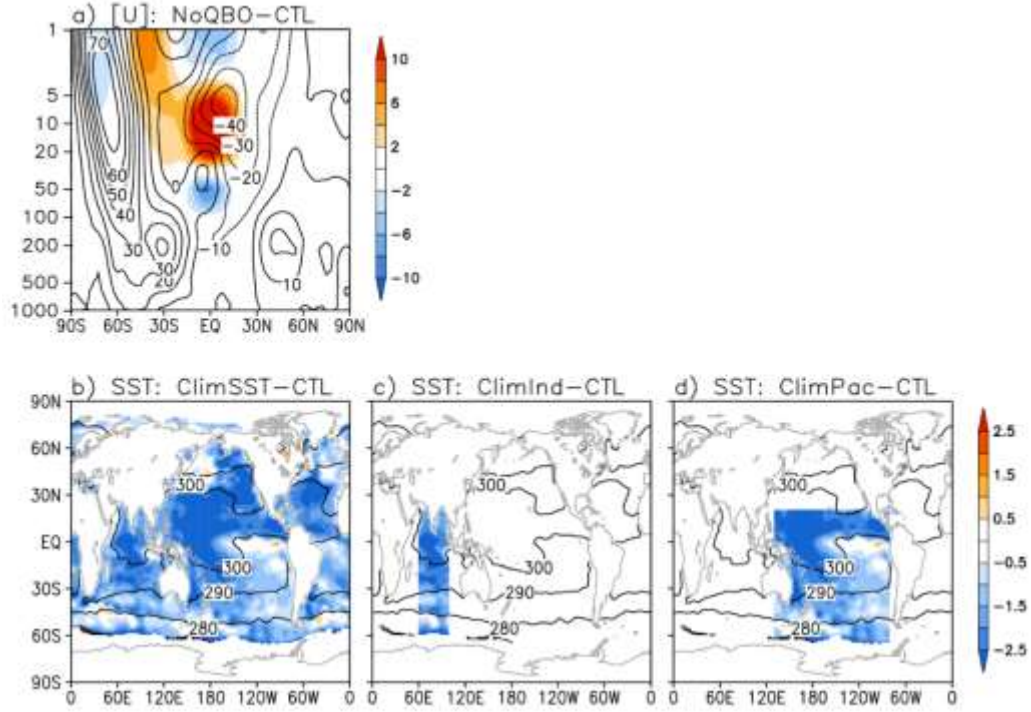


Figure 1. (a) Initial zonal-mean zonal wind ( $[U]$ ) [unit:  $\text{m s}^{-1}$ ] and (b-d) sea surface temperature (SST) [unit: K] for  $\tau=18$  forecast. The initial and boundary conditions for CTL are indicated by the contour. The difference between sensitivity experiments (NoQBO, ColdSST, ColdInd, and ColdPac) and CTL is shaded. Contour intervals are 10.

Table 4. Experiment designs.

Experiment	Description	
	Initial condition	Boundary condition
CTL	Six-hourly atmospheric variables	Daily SST, SIC, and WEASD
NoQBO	Same as CTL except that QBO-related signal is removed in the zonal-mean quantities	Same as CTL
ColdSST	Same as CTL	Same as CTL except for reduced SST
ColdInd	Same as CTL	Same as CTL except for reduced SST over the Indian Ocean
ColdPac	Same as CTL	Same as CTL except for reduced SST over the Pacific Ocean
ColdSST+NoQBO	Same as NoQBO	Same as ColdSST

## 2.5. Evaluation metrics

The SSW prediction skill has often been evaluated by testing the timing of the zonal-mean zonal wind reversal at 60°N and 10 hPa (hereafter U10). This approach, which is based on the SSW definition, is straightforward but has a threshold problem (Kim et al. 2017; Song and Son 2018). For instance, the model successfully predicts the rapid deceleration of the zonal wind, although the prediction of the sign change fails. More importantly, the wind reversal metric does not consider the spatial structure of the polar vortex.

To overcome these caveats, recent studies have used the mean squared error (MSE) and/or anomaly correlation coefficient of the stratospheric geopotential height field (Mukougawa and Hirooka 2004; Stan and Straus 2009; Ichimaru et al. 2016). Following these studies, we quantify the SSW prediction skill with the skill score of MSE, the mean squared skill score (MSSS), for 10-hPa geopotential height (Z10). Here, only the extratropical geopotential height field, poleward of 35°N, is considered in the MSSS calculation. The daily Z10 variance rapidly increases from 35°N to the pole, and the mean-variance averaged over 35°N-90°N accounts for approximately 85% of the Z10 variance in the Northern Hemisphere during the boreal winter (Fig. 2). This result is obtained from zonal-mean Z10 variance fitted to the one-tail Gaussian function. Wind reversal is also evaluated in the present study, but it is simply used for comparison with previous studies.

For fair comparison to previous research (e.g., Marshall and Scaife 2010), a successful SSW prediction is identified when wind reversal is detected on any forecast day regardless of its timing.

The MSSS is defined as below (e.g., Goddard et al. 2013).

$$MSSS(j, \tau) = 1 - \frac{MSE_M(j, \tau)}{MSE_{\bar{O}}(j, \tau)} \quad (1)$$

$$\text{where } MSE_M(j, \tau) = \frac{\sum_{i=1}^N \left( Z_{M,i}(j, \tau) - Z_{O,i}(j, \tau) \right)^2 \cos \theta_i}{\sum_{i=1}^N \cos \theta_i} \quad \text{and} \quad (2)$$

$$MSE_{\bar{O}}(j, \tau) = \frac{\sum_{i=1}^N \left( \overline{Z_{O,i}}(j, \tau) - Z_{O,i}(j, \tau) \right)^2 \cos \theta_i}{\sum_{i=1}^N \cos \theta_i}. \quad (3)$$

Here,  $j$  and  $\tau$  in parentheses indicate the forecast day, ranging from 0 to 30 days, and the forecast lead time from 25 to 0 days with respect to the SSW onset. The subscripts M and O denote the model forecast and the observation (JRA-55), respectively.  $Z$  is the geopotential height at the selected pressure level (10 hPa in this study). Each grid point is indicated by  $i$ , and the total number ( $N$ ) of grid points over 35°N-90°N is 3312 (longitude×latitude=144×23=3312). The corresponding latitude ( $\theta_i$ ) is in degrees. The overbar in Eq. (3) indicates the daily climatology corresponding to the model forecast at  $j$  and  $\tau$ .

The MSEM is defined as the square of the geopotential height differences between the forecast and the observation with a latitudinal weighting (Eq. 2). Since  $MSE\bar{O}$  represents the spatial variance in extratropical Z10 in JRA-55 (Eq. 3), MSSS quantifies the model error normalized by this variance on a selected forecast day. In Eq. (1), the climatological  $MSE\bar{O}$  ( $\overline{MSE\bar{O}}$ ) is used to compute the MSSS instead of  $MSE\bar{O}$  because  $MSE\bar{O}$  varies from one year to another. This interannual variation significantly modulates MSSS. For instance, the same model error, MSEM, can be translated into a large MSSS for strong SSW events with large  $MSE\bar{O}$  but a small MSSS for weak SSW events with small  $MSE\bar{O}$ . This does not allow a fair comparison between different SSW events, especially during different ENSO and QBO phases. To reduce this effect, climatological  $MSE\bar{O}$  is utilized in Eq. (1).

In this study, the successful SSW prediction is identified when MSSS remains positive until the SSW onset. In order to quantify the maximum predictability to each SSW onset, named to the SSW prediction skill, it is defined as the maximum forecast lead time ( $\tau_{max}$ ) among successful SSW predictions. Note that all forecasts for  $\tau \leq \tau_{max}$  must satisfy the successful SSW prediction condition ( $MSSS \geq 0$  until the SSW onset). This metric differs from the prediction limit, which is set as the maximum forecast day ( $j$ ) for  $MSSS \geq 0$  in each forecast. The prediction skill is determined in each SSW event, but the prediction limit is



calculated in each forecast.

To better understand the nature of the prediction error, the MSEM is decomposed into zonal-mean and eddy errors. The zonal-mean component explains the zonal-mean error in geopotential height, while the eddy component is related to the zonally asymmetric geopotential height error.

$$MSE_M(j, \tau) = [MSE_M(j, \tau)] + MSE_M(j, \tau)^* \quad (4)$$

$$\text{where } [MSE_M(j, \tau)] = \frac{\sum_{i=1}^N ([Z_{M,i}(j, \tau)] - [Z_{O,i}(j, \tau)])^2 \cos \theta_i}{\sum_{i=1}^N \cos \theta_i},$$

$$MSE_M(j, \tau)^* = \frac{\sum_{i=1}^N (Z_{M,i}(j, \tau)^* - Z_{O,i}(j, \tau)^*)^2 \cos \theta_i}{\sum_{i=1}^N \cos \theta_i}.$$

The square bracket and asterisk denote the zonal-mean and the deviation from the zonal-mean value, respectively. In Eq. (4), the eddy error can be further expressed as a sum of eddy-amplitude and eddy-phase errors, as shown in Stan and Straus (2009):

$$MSE_M(j, \tau)^* = \sum_{k=1}^{N_k} \{MSE_M(j, \tau, k)_{amp}^* + MSE_M(j, \tau, k)_{phs}^*\} \quad (5)$$

where  $k$  and  $N_k$  denote the zonal wavenumber and maximum wavenumber, respectively.

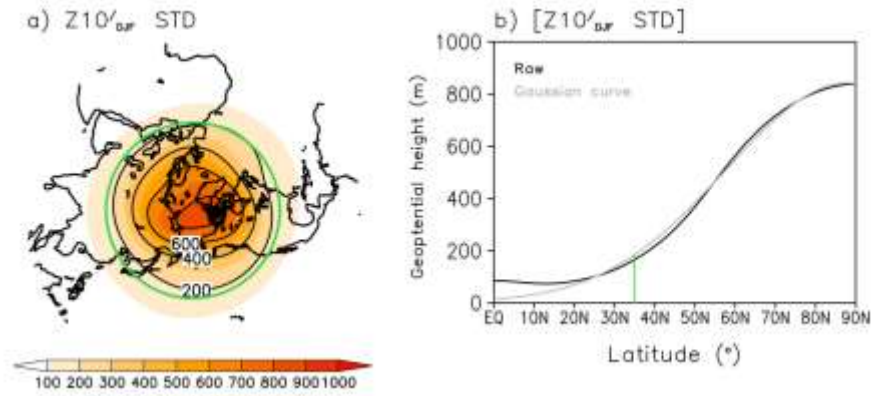


Figure 2. (a) Standard deviation of geopotential height anomaly during December-February and (b) its zonal mean. Green lines denote the reference latitude of 35°N. The Gaussian curve is gray.

## **2.6. S2S operational models**

The real-time forecasts of nine models, which were archived for the S2S prediction project (Vitart et al., 2017), are compared to GRIMs. Here, the China Meteorological Administration Beijing Climate Centre (CMA), European Centre for Medium-range Weather Forecasts (ECMWF), Institute of Atmospheric Sciences and Climate National Research Council of Italy (ISAC-CNR), Japan Meteorological Agency (JMA), Météo-France/Centre National de Recherche Meteorologiques (METEO), National Centers for Environmental Prediction (NCEP), United Kingdom Meteorological Office (UKMO), Environment and Climate Change Canada (ECCC), and Korea Meteorological Administration (KMA) models are evaluated with all possible ensemble members. The Hydro-Meteorological Centre of Russia (HMCR) and Australian Bureau of Meteorology (BOM) models are excluded because the atmospheric variables at 10 hPa are not available for the HMCR model, and the BOM model shows the poor prediction of the wind deceleration in contrast to other S2S models. The real-time forecasts initialized on 29 August 2019, which is a common initialization date, are used. Exceptionally, the JMA forecast starts on 28 August 2019. The 30-day forecasts are only shown in this study.

### **3. Role of ENSO in the NH SSW event**

#### **3.1. SSW frequency for ENSO phase**

The literature reveals that the mean state of the polar vortex in the NH is modulated by ENSO phases. More precisely, it becomes anomalously weak during El Niño winters, while it is strong during La Niña winters. This is well presented in Fig. 3.

Figure 4 presents SSW statistics for seven SSW definitions. The NNR dataset, along with the CPC ENSO index, is used. In this Figure, both the number of SSW events and their relative frequency is shown as in Taguchi (2015). The frequency is defined by dividing the number of SSW events by the number of selected winters for a given ENSO phase. Since multiple SSW events could occur in one winter, SSW frequency could be greater than 100%.

The WMO and U60 definitions show similar SSW statistics. As described in Butler and Polvani (2011; hereafter BP11) and Butler et al. (2014; hereafter BPD14), SSW events occur more frequently not only during El Niño winters but also during La Niña winters, with a slightly higher frequency during El Niño winters. More quantitatively, SSW frequency is about 70%~80% during ENSO winters, but only 35% during ENSO-neutral winters (Fig. 4b). This result, which is essentially an incremental extension of BP11 and BPD14 to 2013/2014 winter,

reaffirms the non-monotonic relationship between ENSO and SSW frequency in the U60 definition (BP11 and BPD14).

More frequent SSW events during El Niño winters are also found in other definitions. Although not always statistically significant, all seven definitions consistently show a higher SSW frequency during El Niño winters than ENSO-neutral winters. However, La Niña winters do not show any systematic relationship. While La Niña-winter SSW frequency is higher than normal in some definitions (i.e., WMO and U60), it is comparable (i.e., U65 and U6090) or slightly lower than normal in other definitions (i.e., Z6090 or EOFU). The 2DM definition even shows more frequent SSW events during La Niña winters than during other winters.

The above results suggest that the ENSO-SSW relationship, especially the ratio of La Niña-winter SSW frequency to ENSO-neutral-winter SSW frequency, is dependent on the details of the SSW definition. Their relationship can be roughly grouped into two groups. The first group, consisting of the WMO, U60, and 2DM definitions, shows more frequent SSW events during ENSO winters than during ENSO-neutral winters, whereas the second group, which includes the U65, U6090, Z6090, and EOFU definitions, shows more frequent SSW events only during El Niño winters. In the latter group, La Niña-winter SSW frequency is not statistically separable from ENSO-neutral-winter SSW frequency even at the 90% confidence

level. A direct comparison between these two groups is not straightforward because each definition utilizes different variables and methodology. The physical and dynamical explanations of the detected ENSO-SSW relationship are also not easy.

For a direct comparison, two representative definitions are chosen in this study. They are U60 and U65 definitions. These two definitions differ only in the reference latitude. By shifting the reference latitude only five degrees poleward, the U65 definition detects four and six more SSW events during El Niño and ENSO-neutral winters, but essentially the same (one less) SSW events during La Niña winters (Fig. 4). The net result is a comparable SSW frequency between ENSO-neutral and La Niña winters in the U65 definition. This contrasts with more frequent SSW events during La Niña than ENSO-neutral winters in the U60 definition.

What causes the different ENSO-SSW relationship between the U60 and U65 definitions? Figure 5 presents the temporal evolution of 10-hPa zonal-mean zonal wind at 60°N (Fig. 5a) and 65°N (Fig. 5b) during the four El Niño winters when SSW events are detected by the U65 definition but not by the U60 definition. The two common SSW events (blue and red Xs in Fig. 5a) appear at almost the same dates. However, in the U65 definition, four additional SSW events are further detected (Xs in Fig. 5b). These events exhibit near-zero zonal-mean zonal wind at

60°N, but not easterly. For instance, the U65 SSW event in February 1958 (second red X in Fig. 5b) results from zonal wind deceleration at 65°N from 16 to -2 m s<sup>-1</sup> over two weeks. A similar deceleration is also found at 60°N. However, the deceleration is weaker (13 m s<sup>-1</sup> to 1 m s<sup>-1</sup>) and does not end up with a wind reversal (Fig. 5a). A similar result is also found in January 1977 and February 1995 (yellow and green Xs in Fig. 5b). Although the zonal wind deceleration is strong at 60°N, the zonal wind does not cross the zero line. In these two cases, minimum zonal winds at 60°N are 0.02 m s<sup>-1</sup> and 0.3 m s<sup>-1</sup>, respectively. These results clearly indicate that different El Niño-winter SSW events between the U60 and U65 definitions are simply caused by the threshold problem. If the U60 definition uses a threshold wind speed of a few m s<sup>-1</sup> rather than 0 m s<sup>-1</sup> (wind reversal), its SSW statistics becomes quantitatively similar to that of the U65 definition. This result implies that the minor warming event in one definition can be a major warming event in other definition by slightly changing the reference latitude or threshold value. Although not shown, the essentially same results are found during ENSO-neutral winters.

The above threshold behavior does not exist in La Niña-winter SSW events at least in the U60 and U65 definitions (Fig. 4). This difference is partly caused by the different latitudinal extent of wind reversal during El Niño- and La Niña-winter SSW events (compare red lines in Figs. 6a,c). The lowest latitude of wind reversal,

within 20 days after the onset of U65 SSW events, is  $46.0^{\circ}\text{N} \pm 7.4^{\circ}$  during La Niña winters but  $53.5^{\circ}\text{N} \pm 8.5^{\circ}$  during El Niño winters ( $55.6^{\circ}\text{N} \pm 7.8^{\circ}$  for ENSO neutral winters). This result indicates that the wind reversal during La Niña winters is wider in latitude ( $\sim 46^{\circ}\text{N}$  to the pole) than that during El Niño winters ( $\sim 54^{\circ}\text{N}$  to the pole). Given the fact that the wind-reversal latitude varies widely among the events, the detection of El Niño-winter (and ENSO-neutral-winter) SSW events can be sensitive to the choice of the reference latitude of  $60^{\circ}\text{N}$  or  $65^{\circ}\text{N}$ . However, La Niña-winter SSW events, which are associated with a wider latitudinal wind reversal, can be well detected by both the U60 and U65 definitions.

Figure 6 illustrates the temporal evolution of 10-hPa zonal-mean zonal wind and 100-hPa zonal-mean eddy heat flux as a function of time lag with respect to U65 SSW onset dates. Here, eddy heat flux is used to quantify vertically propagating wave energy that can lead to the SSW event (e.g., Polvani and Waugh 2004). The background wind (earlier than lag -10 days) in El Niño winters is weaker than that in La Niña winters (Fig. 6e; see also Fig. 3a). Such a difference that is statistically significant at the 95% confidence level is consistent with a stronger planetary-scale wave activity during El Niño winters than during La Niña winters from lag -40 to -20 days [right column of Fig. 4; see also Taguchi and Hartmann (2006) and Calvo et al. (2008)]. The relatively weak polar vortex then may allow an easy wind reversal by moderate wave forcing. In fact, maximum



wave activity associated with El Niño-winter SSW events is relatively weaker than that of La Niña-winter SSW events from lag -15 to 0 days (compare Figs. 6b and 6d; see also Fig. 7).

Another important difference in wave activity, shown in Figs. 6b,d, is the central latitude of wave activity. The maximum wave activity is found at somewhat higher latitudes during El Niño-winter SSW events (Fig. 6b) than during La Niña-winter SSW events (Fig. 6d). Although not statistically significant, their difference clearly exhibits a dipole pattern of about  $\sim 70^\circ\text{N}$  before the onset of the SSW events (Fig. 6f). More quantitatively, the maximum eddy heat flux, integrated over 40 days before the wind reversal at the lowest latitude, is found at  $\sim 70.1^\circ\text{N}$  during El Niño-SSW events but at  $\sim 61.0^\circ\text{N}$  during La Niña-SSW. Here, only SSW events that are used in computing wind-reversal latitudes are considered.

This result, which is further summarized in Fig. 7 for lag -15 to 0 days, is consistent with the different extent of wind reversal during El Niño and La Niña winters. In other words, a rather weak wave forcing at higher latitudes likely leads to a narrow wind reversal during El Niño-winter (and ENSO-neutral-winter) SSW events. This contrasts with a broad wind reversal by strong wave forcing at relatively lower latitudes during La Niña-winter SSW events. Although the linear relationship between the minimum wind-reversal latitude and the maximum heat-flux latitude is rather weak (correlation coefficient of 0.25), this result suggests

that wave-driving latitude is one of the factors that determine the latitudinal width of the wind reversal.

The different wave activity, shown in Figs. 6b,d, results from the different contributions of  $k=1$  and  $k=2$  waves. Figure 7 shows that El Niño-winter SSW events are largely driven by  $k=1$  waves, whereas La Niña-winter SSW events are led by both  $k=1$  and  $k=2$  waves. This difference, which could explain the different latitudinal extent of wind reversal between El Niño- and La Niña-winter SSW events, is consistent with previous studies. Garfinkel et al. (2012) showed that  $k=1$  waves are enhanced at high latitudes during El Niño winters. During La Niña winters,  $k=2$  waves are strengthened at low latitudes. By integrating the stratosphere-resolving model with prescribed SST anomalies, Taguchi and Hartmann (2006) showed that  $k=1$  waves are enhanced around  $65^{\circ}\text{N}$  in response to El Niño-like SST forcing. In contrast, during La Niña winters,  $k=2$  wave amplitude becomes stronger around  $55^{\circ}\text{N}$ . Calvo et al. (2008) also documented a stronger planetary-scale wave activity during El Niño winters than during La Niña winters, particularly in high latitudes.

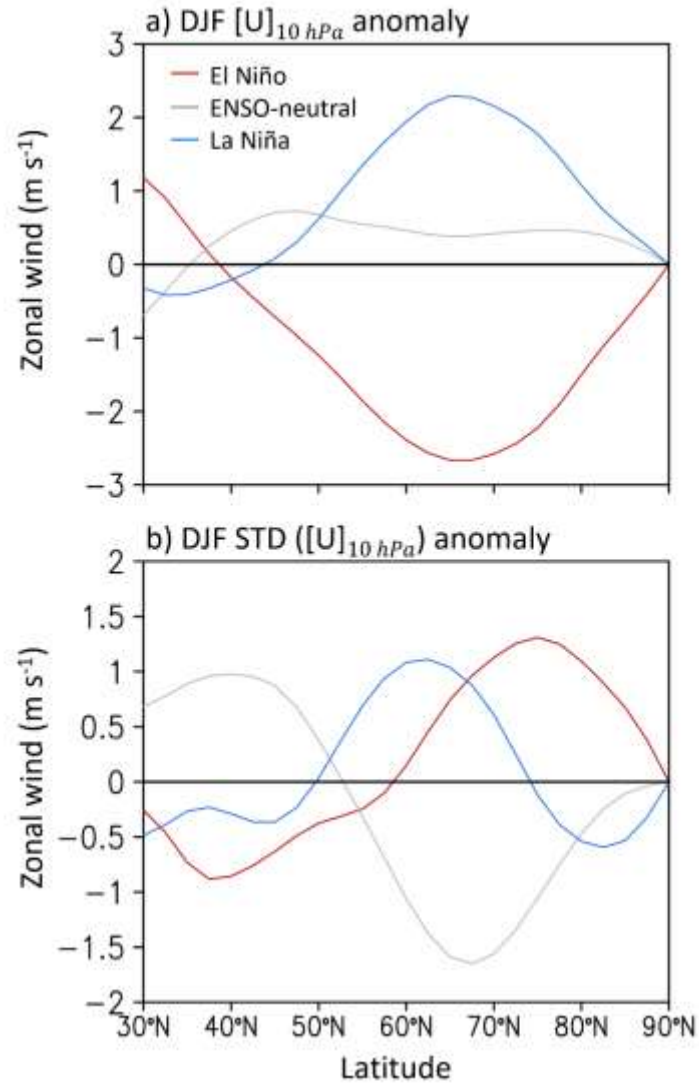


Figure 3. Latitudinal profile of 10-hPa zonal-mean zonal wind anomalies during El Niño, La Niña, and ENSO-neutral winters: (a) seasonal-mean and (b) daily standard deviation. As described in section 2, NNR and CPC ENSO index are used here.

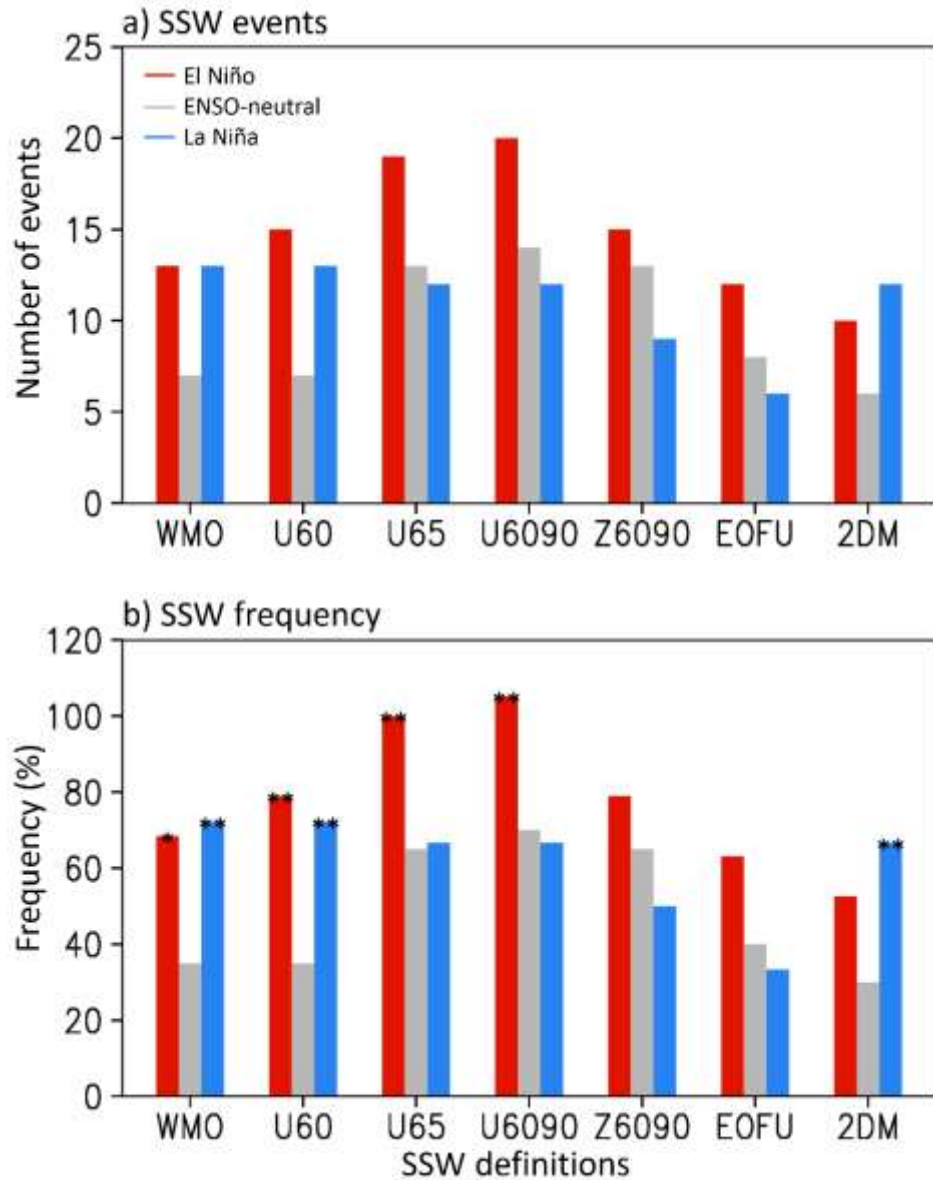


Figure 4. (a) Number of SSW events and (b) its frequency during El Niño, ENSO-neutral, and La Niña winters. In (b), the values that are statistically significant at the 90% and 95% confidence levels are denoted with one and two asterisks, respectively. NNR and CPC ENSO index are used. See the text for the details.

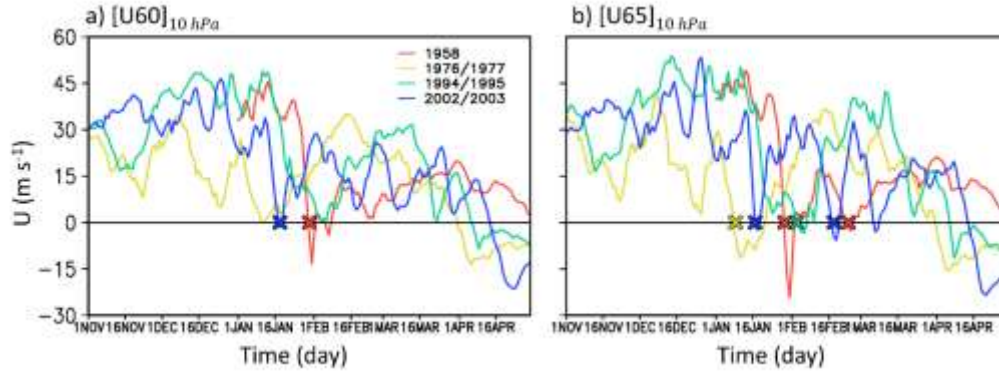
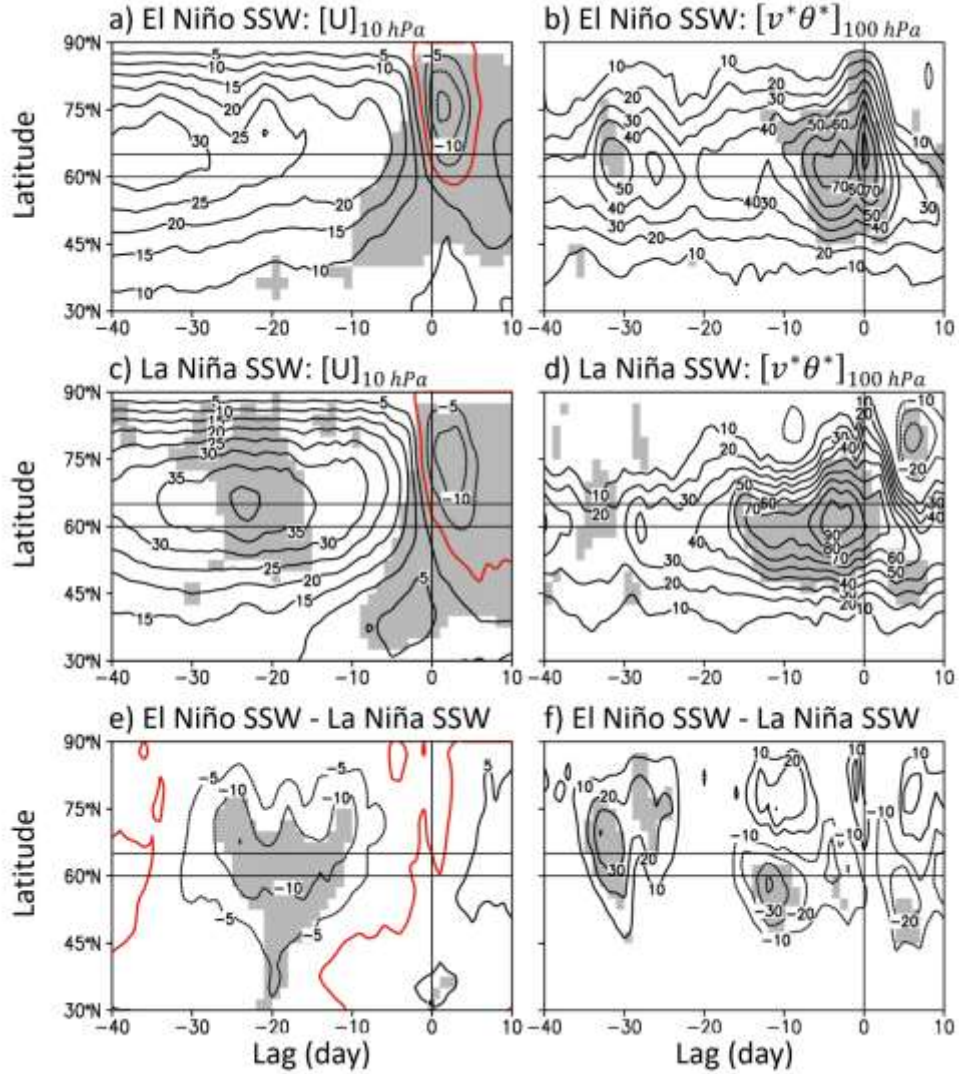


Figure 5. Temporal evolution of 10-hPa zonal-mean zonal wind at (a) 60°N and (b) 65°N during El Niño winters. Only the winters when SSW events are detected by the U65 definition but not by the U60 definition are considered. The onset date of each SSW event is denoted by X mark.



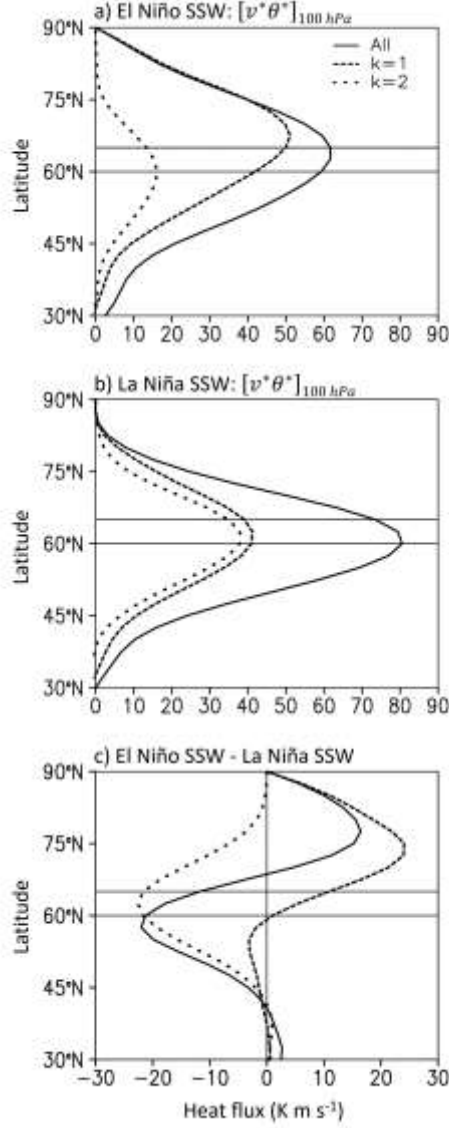


Figure 7. Latitudinal profile of 100-hPa eddy heat flux integrated from lag -15 day to the onset of U65 SSW events for (a) El Niño, (b) La Niña winters, and (c) their difference. Heat fluxes of zonal-wavenumber one ( $k=1$ ) and two ( $k=2$ ) waves are denoted with dashed and dotted lines, respectively. The reference latitudes of 60°N and 65°N are indicated by horizontal line.

### 3.2. Sensitivity test for the ENSO-SSW relationship

The sensitivity of the above results to the choice of reanalysis datasets, ENSO indices, and SST datasets is examined in this section. The overall results are summarized in Fig. 8 for both U60 and U65 definitions. It is evident from Fig. 8a that the relative ratio of ENSO-winter to ENSO-neutral-winter SSW frequency does not change much when different ENSO indices are used (CPC vs. SIMPLE definitions). Its sensitivity to the choice of SST data (CPC vs. CPCv5) is also relatively minor.

Here, it is important to note that statistical significance is somewhat sensitive to the datasets. La Niña-winter SSW frequency slightly decreases when the SIMPLE ENSO index is used, while ENSO-neutral-winter SSW frequency slightly increases (top-middle box in Fig. 8). This makes statistically indistinguishable SSW frequency between La Niña and ENSO neutral winters.

The ENSO-SSW relationship is also only weakly sensitive to the choice of reanalysis datasets (compare Fig. 8a and 8b). However, the statistical significance becomes lower in JRA-55 than in NNR. The significant values obtained in the SIMPLE ENSO index also become statistically insignificant if the analysis period is shortened or only one SSW event is counted for a given winter. These results indicate that the ENSO-SSW relationship, reported in this study, is only marginally significant.



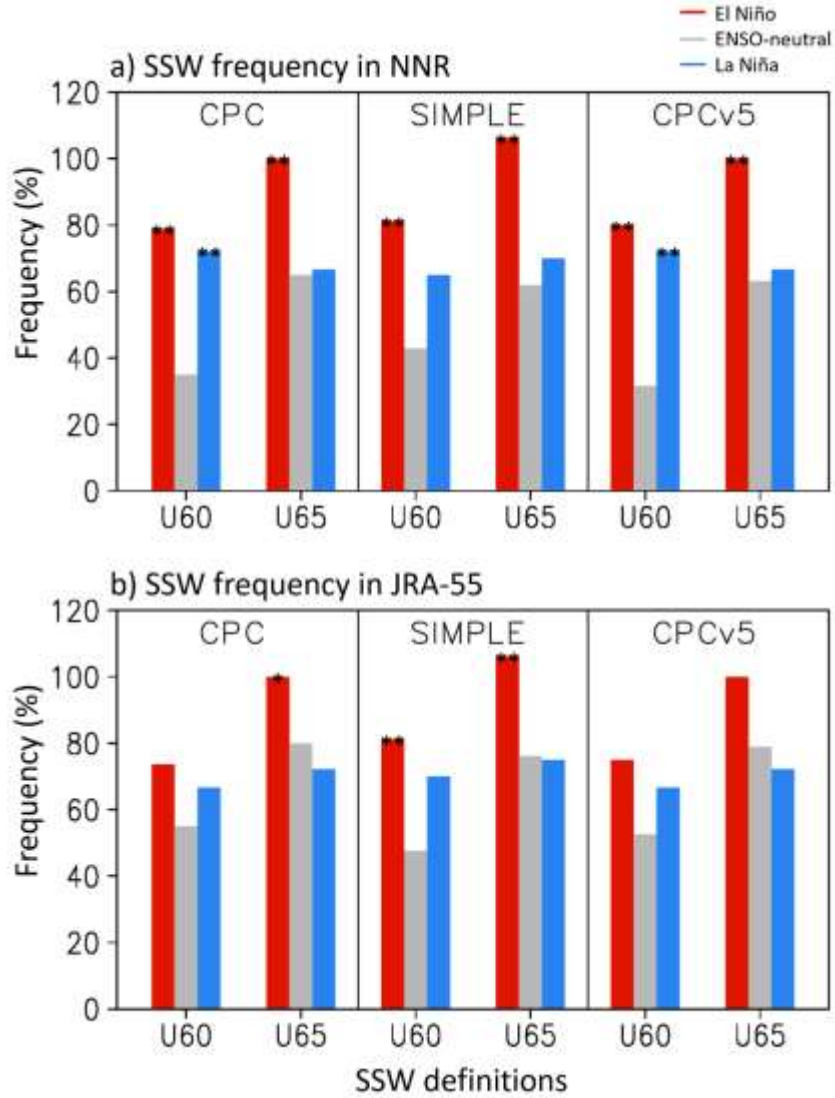


Figure 8. SSW frequency during ENSO winters in (a) NNR and (b) JRA-55 datasets. Two different SSW definitions, i.e., U60 and U65 definitions, and three different ENSO indices, i.e., CPC, SIMPLE, and CPCv5, are applied. Note that SSW statistics for NNR and CPC ENSO index (left box of a) are identical to those in Fig. 4b.

### **3.3. Decadal changes in the ENSO-SSW relationship**

This study finds that a nonlinear ENSO-SSW relationship is only detected for WMO or U60 definitions, while the other definitions, U65, U6090, Z6090, and EOFU definitions, show the linear ENSO-SSW relationship. It is more reasonable to conclude that El Niño-winter SSW frequency is higher than other winters. However, the recent study (Hu et al. 2017) suggested that the relationship between ENSO and the seasonal-mean polar vortex has been changed during a recent decade. This time-dependent relationship is also observed in the polar vortex variability, such as SSW frequency (Domeison et al. 2019). They found that the frequent SSW events during El Niño winters are only evident in the past decade, and it is recently broken.

To clarify the recently-broken ENSO-SSW relationship, this study separates the ENSO-SSW relationship into El Niño and La Niña winters. Figure 9 shows the SSW frequency on the 31-years moving window during two different ENSO winters for JRA-55 and ERA20C reanalysis datasets. The solid lines in Fig. 9 are from ERA20C, and the dotted one is the result of JRA-55. The El Niño-winter SSW frequency has a probability of about 100% and independent of the time-varying. On the other hand, the La Niña-winter SSW frequency dramatically varies with a range from 20% to 100% in both datasets (Fig. 9a). For the period from the 1900s to the 1950s, the SSW frequency decreases gradually, but the sign of this

trend becomes positive from negative after the 1950s. It can be mostly explained by the changes in the number of SSW events for each ENSO phase (Fig. 9b).

To find a cause of decadal changes in SSW frequency during La Niña winters, the effect of satellite data assimilation is investigated by comparing JRA-55 and JRA-55C (dotted lines in Fig. 10). For JRA-55C, the SSW frequency is reduced during El Niño winters before 1990 and during La Niña winters after 1990. Except for this, the recent increase of La Niña-winter SSW frequency is also observed in JRA-55C. According to our results, the satellite data inhomogeneity is not a main factor of the broken ENSO-SSW relationship. Note that the 21-years window is adopted here because of the relatively short record.

We find that only La Niña-winter SSW frequency shows the decadal changes. Less SSW frequency and events are detected in the mid-1900s. These long-term changes are well matched to the PDO changes (not shown). Figure 11 shows the correlation between polar-cap averaged geopotential height at 10 hPa and SST for both JRA-55 and ERA20C during the boreal winter on the monthly time scale. As expected, tropical SST is positively correlated with the polar vortex variability, in which the polar vortex weakening is related to the warm SST condition over the tropics (El Niño). Another center is located at the mid-latitude, but the polar vortex variability is negatively correlated with the SST condition. The mid-latitude correlation pattern is well matched to the PDO pattern (not shown). The cold

condition of mid-latitude SST is related to the polar vortex weakening and dominant in a positive PDO phase. To define the interannual-to-decadal variation of PDO without EOF analysis, SST anomalies over the North Pacific region (NPSST) (black box over the mid-latitude in Fig. 11) are averaged.

Figure 12 shows the decadal changes in the PDO-SSW relationship with respect to the different PDO winters. Hereafter, NPSST is the same as the negative PDO winters. During the whole period, the SSW frequency is more favorable during -NPSST winters than +NPSST winters. This is observed in both JRA-55 and ERA20C datasets, but the different SSW frequency between NPSST winters is less evident in JRA-55 dataset and a recent decade (Fig. 12a). The difference observed in JRA-55 is mostly the same as a result in the literature (Woo et al. 2015), suggesting ~80% frequency during +PDO (-NPSST) and ~60% frequency during -PDO (+NPSST). The SSW frequency is calculated by dividing the SSW number by the NPSST number in each phase. Each component is shown in Figs. 12b,c. The decadal changes in the SSW number are well matched to that of NPSST winters during the negative NPSST phase. However, the SSW number during +NPSST winters is not following the number of NPSST winters (compare Fig. 12b and 12c). More precisely, the SSW numbers are detected around five for all periods during +NPSST winters, while the number of +NPSST winters varies from five to 18. Our findings indicate that the SSW occurrence is highly related to -

NPSST winters (+PDO) but not in +NPSST winters. The recent increase of the SSW number during -NPSST winters is possibly related to the recent increase of La Niña-winter SSW frequency.

Is the nonstationary ENSO-SSW relationship related to the PDO modulation in the SSW occurrence? If the recent increase of La Niña-winter SSW frequency is just a statistical result due to the PDO-SSW relationship, La Niña-winter SSW events occur more frequently during the recent positive PDO winters. Figure 13 shows the linear relationship between ENSO and PDO winters. ENSO and PDO are closely related to each other. During El Niño winters, positive PDO winters are more detected, and negative PDO winters are coherent with La Niña winters. In other words, positive PDO (-NPSST) is not directly related to La Niña winters. Indeed, no La Niña winters are observed during positive PDO winters (not shown). This indicates that the decadal changes in SSW frequency are associated with PDO winters, but it does not mean that PDO is the cause of the recently-broken ENSO-SSW relationship.

The present study clarifies the ENSO-SSW relationship and its decadal change. With various sensitivity tests, SSW events frequently occur only during El Niño winters, not other winters. The frequent SSW events during La Niña winters, suggested by the literature, is dictated by the threshold problem of wind reversal definition. The modeling results in the literature paves our findings.

Furthermore, the recently-broken ENSO-SSW relationship is detected only during La Niña winters, but this is not a result of changes in SSW dynamics during La Niña winters from the past to the recent. The changes in La Niña winters-SSW frequency is related to the increase of SSW events during -NPSST winters (+PDO winters) during a recent decade. Indeed, the SSW events are favorable during -NPSST winters for the whole data period from 1900 to 2010 compared to +NPSST winters. During -NPSST winters, the Aleutian low, which is a precursor of SSW events, is more deepening than during +NPSST winters. As Song and Son (2018) suggested, an increase of SSW events is observed during El Niño winters or -NPSST (+PDO) winters, no other winters, and the recently-broken ENSO-SSW relationship is simply a result of the increase of -NPSST winters.

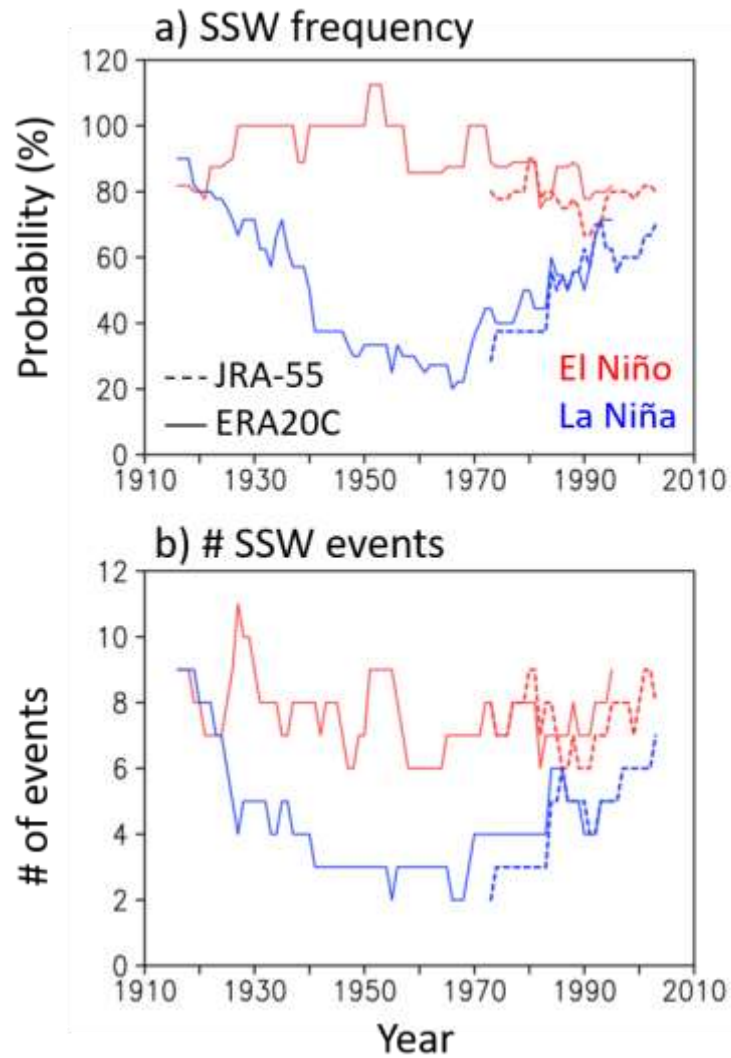


Figure 9. (a) 31-years SSW frequency and (b) SSW number during ENSO winters for JRA-55 (dotted) and ERA20C (solid). The blue and red indicate El Niño and La Niña winters, respectively.

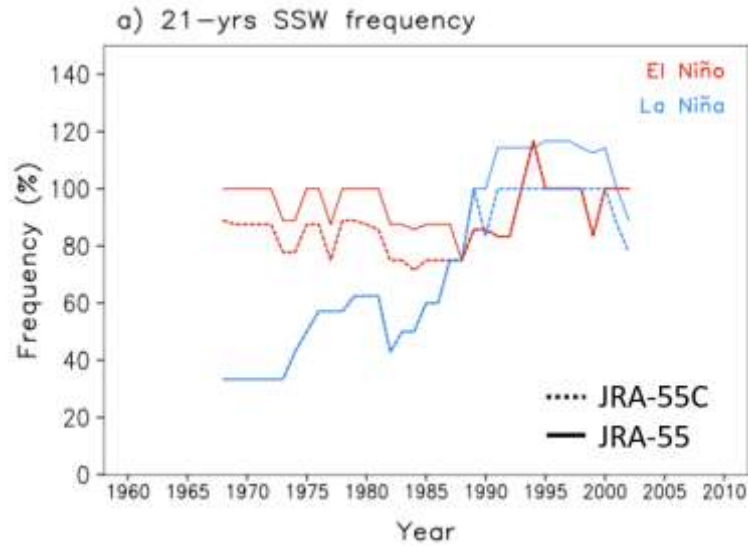


Figure 10. 21-years SSW frequency during ENSO winters for JRA-55C (dotted) and JRA-55 (solid). The blue and red indicate El Niño and La Niña winters, respectively.

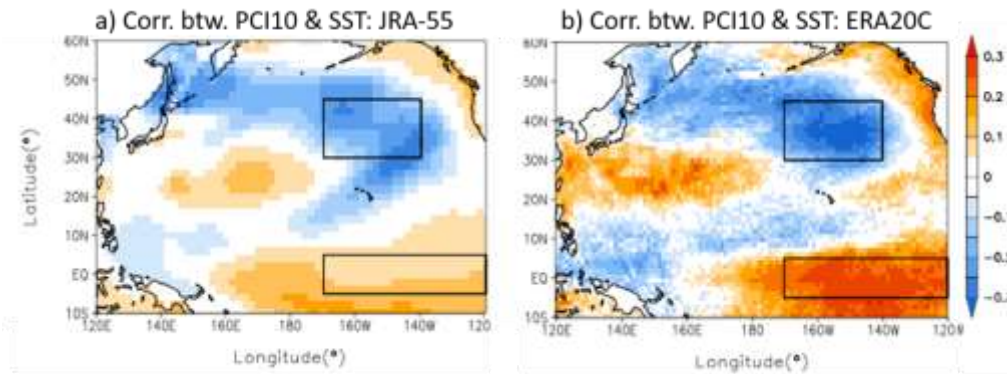


Figure 11. Correlation between polar-cap averaged geopotential height (PCI) at 10 hPa and SST over the Pacific Ocean for (a) JRA-55 and (b) ERA20C. The boxes indicate the area of NPSST index and ENSO index.



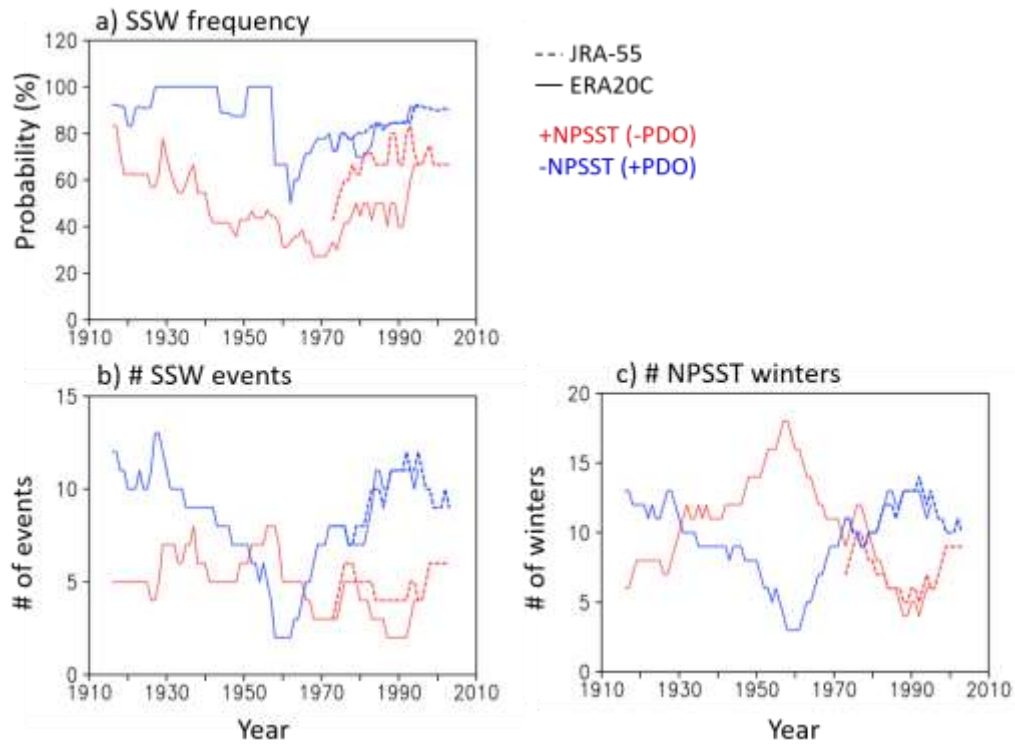


Figure 12. (a) SSW frequency, (b) SSW number, and (c) NPSST winters during PDO winters in JRA-55 (dotted) and ERA20 (solid). The blue and red lines indicate the +PDO and -PDO winters, respectively.

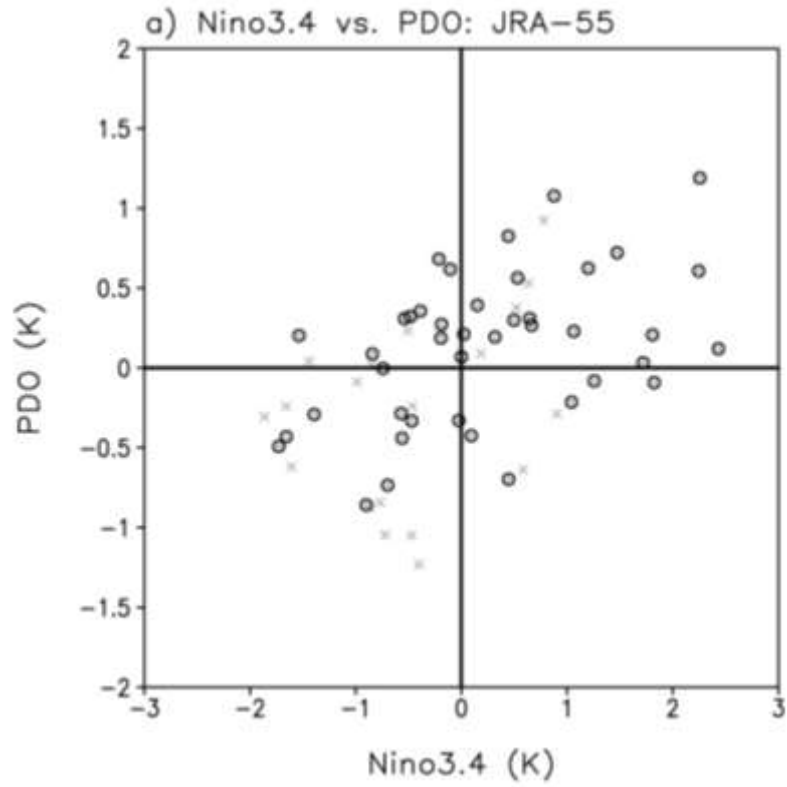


Figure 13. Scatter plot between DJF-mean NIÑO3.4 index and PDO index for JRA-55 dataset from 1958 to 2018. Open circle indicates the SSW winters.

## 4. Role of ENSO in the SH SSW event

### 4.1. 2019 SH SSW event

Figure 14a shows the temporal evolution of the 10-hPa zonal-mean zonal wind ( $[U10]$ ) at  $50^\circ\text{S}$  as a function of the calendar date. The zonal winds typically turn from the westerly to the easterly from October to November, but in 2002 and 2019, the wind reversal appears in September (red and blue lines, respectively, in Fig. 14a). These early wind reversals are identified as the SSW events.

The wind deceleration in 2019 is more dramatic than that in 2002, decreasing from  $70 \text{ m s}^{-1}$  to the easterly direction. Its onset date, September 16, is also earlier than that of 2002. As documented in the literature,  $[U10]$  at  $60^\circ\text{S}$  does not become easterly from the westerly direction in 2019, characterizing the 2019 SSW event in the SH as a relatively low-latitude SSW event (Rao et al. 2020). The positive  $Z$  over the polar region increases to a value larger than 1600 m around the SSW onset. The high anomaly, corresponding to polar vortex weakening, persists for up to three months in the stratosphere, and it affects the troposphere in the late austral spring (November to December) (Fig. 14b). The circulation anomalies lead to hot and dry conditions over Australia in the late spring (Lim et al. 2020a).

Lim et al. (2020a) suggest that the 2019 SSW event is driven by accumulated wave activity from the troposphere. Figure 14c shows the vertical component of

the zonal-mean wave flux ( $F_z$ ) averaged over the mid-latitudes ( $45^\circ$ – $75^\circ$ S). Here,  $F_z$  is based on the calculation of Takaya and Nakamura (2002), and its zonal-mean component is the same as the vertical component of the Eliassen-Palm flux (i.e., positive meridional eddy heat flux). Amplified wave activities are observed from 30 days before to 3 days after the SSW onset. The horizontal distribution of  $F_z$ , averaged from 20 days before the SSW onset, shows enhanced wave activities over two regions, i.e., the South Pacific ( $180^\circ$ E– $60^\circ$ W) and the South Indian ( $60^\circ$ – $120^\circ$ E) Oceans, which likely drive the SSW event (Fig. 14d).

The enhanced upward wave propagation can often be explained by the constructive linear interference between the climatological and anomalous  $Z$  (Smith and Kushner 2012). Figure 14e shows the climatological (shading) and anomalous (contour)  $Z$  at 200 hPa by removing the zonal mean. The wave activities are enhanced over the regions where the zonally-asymmetric  $Z$  anomaly is in phase with a climatological one (Figs. 14d,e). Although the locations with the maximum and minimum  $Z$  anomalies are slightly shifted to the east compared to the climatological one, the sign of  $Z$  is generally in phase between the climatology and anomalies. Such  $Z$  anomalies could be led by the Rossby wave train lying across the South Pacific (e.g., Renwick and Revell 1999). In particular, a high anomaly can be formed when a positive IOD and warm SST over the central Pacific are observed (Lim et al. 2020b; Rao et al. 2020). To examine the possible

constructive linear interference, the vertical structure of  $Z$  is illustrated in Fig. 14f. The climatological  $Z$  is vertically tilted to the west, indicating the upward propagating Rossby wave. This climatology is accurately overlaid with the  $Z$  anomaly in the stratosphere. The tropospheric high anomaly lies on the climatological high over the Pacific Ocean, although its peak is slightly shifted to the east.

As described by Rao et al. (2020), the 2019 SSW event is possibly related to the background flow and surface boundary conditions. Figure 15a shows the zonal-mean zonal wind ( $[U]$ ) in August 2019. A strong westerly is observed in the SH polar stratosphere, and the tropical zonal wind is the easterly at 10 hPa, indicating EQBO. The observed zonal gradient of the SST over the Indian Ocean is negative, corresponding to a positive IOD. The warm SST over the Pacific Ocean seems to be a central Pacific El Niño-like pattern (Fig. 15b). They are monitored by the dipole mode index (hereafter IOD index; Saji et al. 1999) and the NIÑO4 index.

Figures 15c–e show the temporal evolution of the QBO, IOD, and NIÑO4 indices in August. Each index is identified by a 10-hPa zonal wind anomaly over  $15^{\circ}\text{S}$ – $15^{\circ}\text{N}$  for the QBO index (red line in Fig. 15a), the difference between the western SST ( $50^{\circ}$ – $70^{\circ}\text{E}$  and  $10^{\circ}\text{S}$ – $10^{\circ}\text{N}$ ) and eastern SST ( $90^{\circ}$ – $110^{\circ}\text{E}$  and  $10^{\circ}$ – $0^{\circ}\text{S}$ ) over the Indian Ocean for the IOD index (red boxes in Fig. 15b), and the SST

anomaly over the central Pacific Ocean ( $160^{\circ}\text{E}$ – $150^{\circ}\text{W}$  and  $5^{\circ}\text{S}$ – $5^{\circ}\text{N}$ ) for the NIÑO4 index (red box in Fig. 15b). The 2019 QBO is identified as the EQBO, based on the one standard deviation (dashed line in Fig. 15c), but its amplitude is not very strong relative to other EQBO years ( $\sim 18 \text{ m s}^{-1}$ ). The 2019 IOD is quite abnormal with an amplitude of  $\sim 1.4 \text{ K}$ , which is the record-high IOD during 1958–2019 (Fig. 15d). The warm SST condition is observed over the central Pacific Ocean with an amplitude of  $\sim 0.9 \text{ K}$ .

In summary, the 2019 SSW event is likely driven by planetary-scale wave activity originating from the troposphere, interacting with background wind in the stratosphere. The anomalous wave activity is led by the high and low anomalies over the South Pacific and the South Indian Oceans, respectively, which constructively interfere with the climatological high and low. These processes are possibly related to the EQBO, central Pacific El Niño-like SST, and the highest IOD.

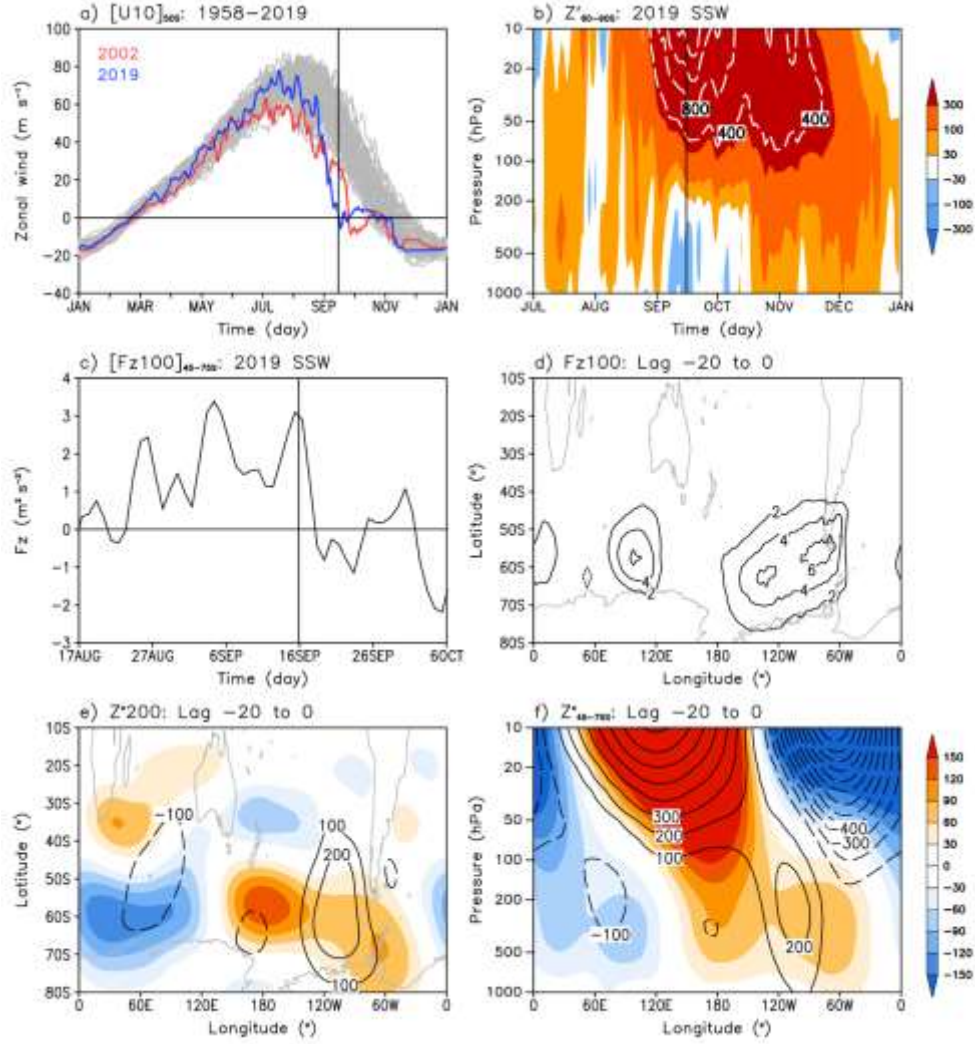


Figure 14. Temporal evolution of (a) 10-hPa zonal-mean zonal wind ( $[U10]$ ) at 50°S, (b) polar-cap (south of 60°S) averaged geopotential height ( $Z$ ) anomaly, and (c) vertical component of zonal-mean wave activity flux ( $Fz$ ) at 100 hPa averaged over 45°–75°S. The vertical lines indicate the 2019 SSW onset. Spatial distribution of time-mean (d) 100-hPa  $Fz$  [unit:  $m^2 s^{-2}$ ], (e) 200-hPa  $Z$  [unit: m], and (f) vertical structure of  $Z$  averaged over 45°–75°S [unit: m]. The time average is conducted from 20 days before (lag -20) to the SSW onset (lag 0). (e, f) Climatological and anomalous  $Z$  are indicated by the shading and the contour, respectively.

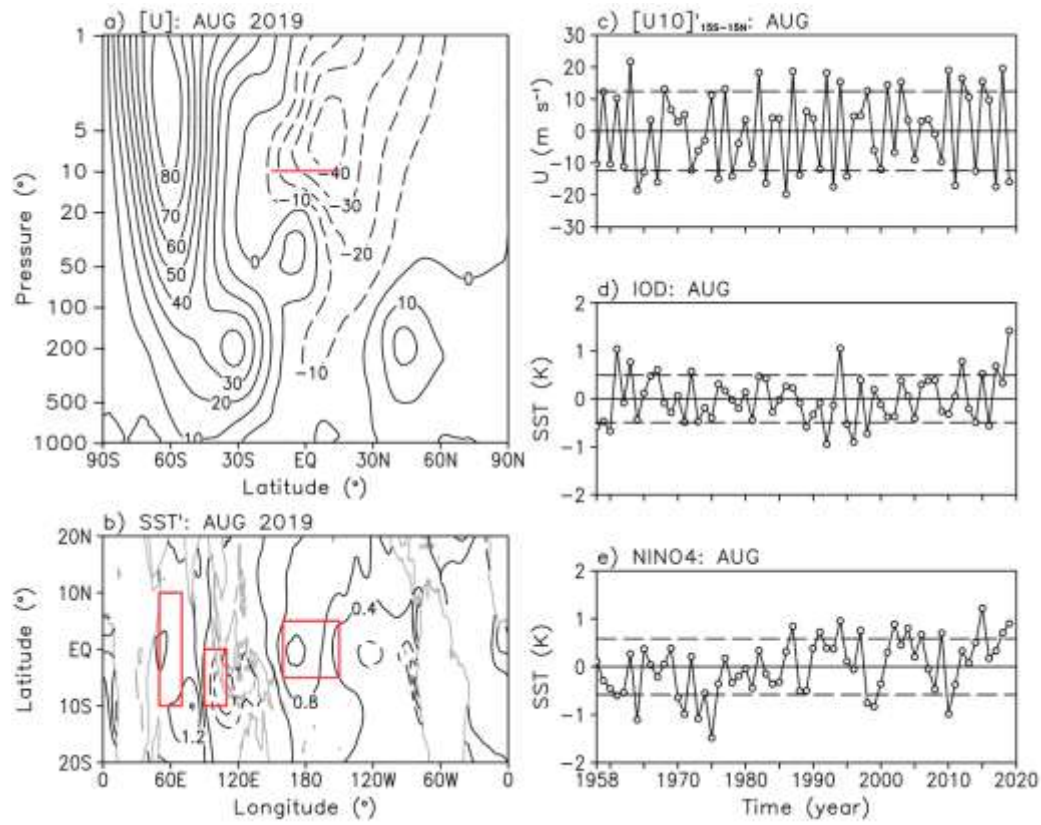


Figure 15. (a) Zonal-mean zonal wind ( $[U]$ ) [unit:  $\text{m s}^{-1}$ ] and (b) sea-surface temperature (SST) anomaly [unit: K] in August, 2019. (c)  $[U10]$  anomaly, (d) IOD, (e) NINO4 timeseries in August. Each index is obtained from the red line and boxes in (a,b). The dashed lines in (c–e) indicate the range of each standard deviation.



## 4.2. Key driver of the 2019 SH SSW event

Figures 16a,b display the temporal evolution of [U10] averaged over 40°–60°S for the S2S models and GRIMs experiments. The reference from JRA-55 is also shown in black. As discussed in Fig. 14a, the strong westerly at 10 hPa starts to decelerate in late August, and it becomes easterly on September 16 (vertical lines in Figs. 16a,b). Most S2S models reasonably capture this wind deceleration, except for the BOM model, although the predicted [U10] does not reverse to the easterly around the SSW onset (Fig. 16a). The inter-model spread gradually increases. The models with better prediction skills, e.g., the ECMWF, UKMO, and KMA models, are typically the high-top models. Not surprisingly, the low-top models such as the BOM model poorly predict the 2019 SSW event (Rao et al. 2020). Among the high-top models, the ECMWF, ECCO, and KMA models better predict the wind deceleration (blue, yellow, and orange lines, respectively, in Fig. 16a).

The GRIMs with the high-top version reliably predicts the wind deceleration. Its prediction skill is within a prediction range of 10 S2S models (red line in Fig. 16a). Figure 17b further shows the predicted [U10] from the six GRIMs experiments: the CTL, ColdSST, ColdInd, ColdPac, NoQBO, and ColdSST+NoQBO experiments. The predicted [U10] is reliable in the first-week prediction of all the experiments, but it starts to diverge after the 7th forecast day

(September 5). For instance, the wind decelerations in the ColdSST, ColdPac, and ColdSST+NoQBO experiments (purple, blue, and sky blue, respectively) stop at  $20 \text{ m s}^{-1}$ , while those in the CTL, NoQBO, and ColdInd experiments keep decreasing to  $10 \text{ m s}^{-1}$  or less (red, pink, and yellow, respectively). The key difference between the good predictions (CTL, NoQBO, and ColdInd) and the poor predictions (ColdSST, ColdPac, and ColdSST+NoQBO) is whether the observed SST over the Pacific Ocean is prescribed. In other words, when the Pacific SST is prescribed with the climatology, polar vortex weakening is poorly predicted. This result indicates that the Pacific SST is the crucial factor in capturing the polar vortex weakening during the 2019 SSW event. Note that the ColdInd experiment shows an even better prediction skill than the CTL experiment, and the NoQBO experiment also shows a slightly improved prediction performance. However, this result is not consistently found in the other initializations. This finding is discussed in the following Figure.

To better quantify the prediction error, the MSSSs for all the GRIMs experiments are shown in Fig. 16c. Given that the SSW characteristics are dependent on its zonally asymmetric feature (e.g., Charlton and Polvani 2007), the MSSS has the advantage of considering both the zonal-mean and eddy components. The separation between the good and poor prediction groups becomes more apparent. The MSSS in both groups slowly decreases from 1.0 to

0.0 until the 7th forecast day. The poor prediction group, however, shows a rapid decrease in the MSSS after a week, reaching -7.0 on September 20, which is much larger than the MSSS of the good prediction group with a minimum MSSS ranging from -1.0 to -3.0. Consistent with [U10] prediction, the spatial pattern in the polar vortex weakening is not well predicted in the experiments with the climatological Pacific SST.

The GRIMs predictions are further evaluated with other initializations ( $\tau=20$  to 5) (Fig. 17). The 10-hPa Z over the south of 60°S and the MSSS, both averaged over  $\pm 3$  days with respect to the SSW onset, are shown in Fig. 17. For instance, the MSSS at  $\tau=5$  in Fig. 18b indicates the MSSS averaged from September 13 to 19 in the model forecast initialized at five days before the SSW onset on September 16. All the experiments underestimate the polar vortex weakening (compare the colored lines to the black horizontal line in Fig. 17a). Again, the good prediction group better predicts the polar vortex weakening than the poor prediction group. Their differences are particularly pronounced in the  $\tau=16$  to 13 forecasts. This gap, which reaches 437 gpm, gradually decreases as the onset of the SSW event approaches because the effect of the boundary condition diminishes in the short-term forecast.

The MSSS and its zonal-mean and eddy components are illustrated in Figs. 17b–d. Consistent with Fig. 16c, all forecasts in the good prediction group show a

larger MSSS than a poor prediction group. The MSSS becomes nearly zero for  $\tau \leq 14$  forecasts in the good prediction group, while it is found at relatively short forecast lead times ( $\tau \leq 9$ ) in the poor prediction group. Their difference is more evident in the zonal-mean component than in the eddy component (Figs. 17c,d). The zonal-mean errors are larger in the poor prediction group than in the good prediction group for all forecast lead times, and the spread within each group is rather small. In contrast, the separation in the eddy errors is less clear, especially for the long forecast lead times ( $\tau \geq 16$ ), and the inter-experiment error spread is large.

The polar vortex prediction errors by both the zonal-mean and eddy components could be related to the wave activities that drive the 2019 SSW event. Figure 18 shows the upward propagating wave activity flux,  $F_z$  at 100 and 200 hPa, averaged for 10 days before the SSW onset in the JRA-55 and  $\tau=16$  forecast. The latitudinal average over  $45^\circ\text{--}75^\circ\text{S}$  is applied. At 100- and 200-hPa levels, vertically propagating waves are observed over the two main regions, the South Indian ( $90^\circ\text{--}130^\circ\text{E}$ ) and the South Pacific Oceans ( $180^\circ\text{E}\text{--}80^\circ\text{W}$ ) (black line in Fig. 18). A third peak also appears over the South Atlantic Ocean ( $0^\circ\text{--}30^\circ\text{E}$ ) at 200 hPa, but a large amount of this wave energy is deposited between 100 and 200 hPa, i.e., a decrease in  $F_z$  from  $\sim 5$  to  $\sim 2 \text{ m}^2 \text{ s}^{-2}$ . The wave activities over the Pacific and Indian Oceans maintain their amplitude between the two levels ( $\sim 6 \text{ m}^2 \text{ s}^{-2}$ ),

and they disappear in the upper stratosphere (not shown). This finding reveals that the vertically propagating waves over the Pacific and Indian Oceans are broken in the lower and middle stratosphere, leading to the polar vortex weakening.

The wave activities are reasonably predicted in the GRIMs experiments, especially in the good prediction group (red, pink, and yellow lines in Fig. 18). The wave activities over the South Pacific Ocean are well captured in the good prediction group, although the maximum peaks are shifted to the west by  $\sim 60^\circ$  and  $\sim 30^\circ$  at 100 and 200 hPa, respectively. They are substantially underestimated in the poor prediction group. The predicted waves over the South Indian Ocean do not differ from one experiment to another (colored lines in Fig. 18). They are consistently underestimated in all model experiments with the westward shift in their peaks. These results indicate that the key difference between the good and poor prediction groups is the prediction of wave activities over the South Pacific Ocean, which explains why the SSW prediction skill is sensitive to the Pacific SST.

The successful prediction of the tropospheric  $Z$  plays a crucial role in the polar vortex weakening in the S2S model forecasts (Rao et al. 2020). This finding also holds for the GRIMs forecasts. Figure 19 shows the 200-hPa  $Z$  by removing the zonal mean for  $\tau=16$  forecasts in six different experiments (green lines in Fig. 19). A clear difference between good and poor prediction groups appears over the South Pacific Ocean, where the vertically propagating waves are predicted

differently by the experiments. The anomalous high over the South Pacific Ocean, where the climatological high is observed, is reliably predicted in a good prediction group (Figs. 19a,c,e), although it is slightly shifted to the west compared to JRA-55 (compare green to black contours). The poor prediction group fails to predict the high anomaly over the South Pacific Ocean (Figs. 19b,d,f). All experiments overestimate the low anomalies at the west of the high anomalies ( $120^{\circ}$ – $180^{\circ}$ E) except for the ColdPac experiment. The dipole pattern over the South Indian Ocean, where the climatological low is observed (blue in Fig. 19), is relatively well predicted in all experiments.

To find the relationship between the tropospheric anomalies and the vertically propagating waves over the South Pacific Ocean, the vertical structure of the predicted and observed Zs is additionally investigated (Fig. 20). When the westward tilt of Z anomalies is in phase with the climatology, upward-propagating waves are anticipated to amplify the so-called constructive linear interference (Smith and Kushner 2012). As displayed in Fig. 14f, constructive linear interference is observed during the 2019 SSW event (black contours in Fig. 20). This finding is well captured by the good prediction group (compare green lines in Figs. 20a,c,e to those in Figs. 20b,d,f). A reliable prediction of the tropospheric high over the South Pacific Ocean is important in this linear interference. The good prediction group successfully predicts its amplitude, while the poor prediction

group fails to predict it. Consistent with the 200-hPa Z and 100-hPa Fz predictions, the predicted high anomaly in the troposphere is slightly shifted to the west of JRA-55. Although not shown, the same results are essentially found in the other forecasts ( $13 \leq \tau \leq 16$ ) when the good and poor prediction groups are well separated.

The present study reveals that the well-predicted Pacific high, related to the Pacific SST, leads to favorable conditions for enhanced local wave activity and improved SSW prediction in 2019. This tropospheric high anomaly might be associated with the Rossby wave train from the central Pacific, which lies across the South Pacific. Our findings suggest that the 2019 SSW event in the SH is driven by tropospheric wave activity, likely induced by the central Pacific El Niño-like SST.

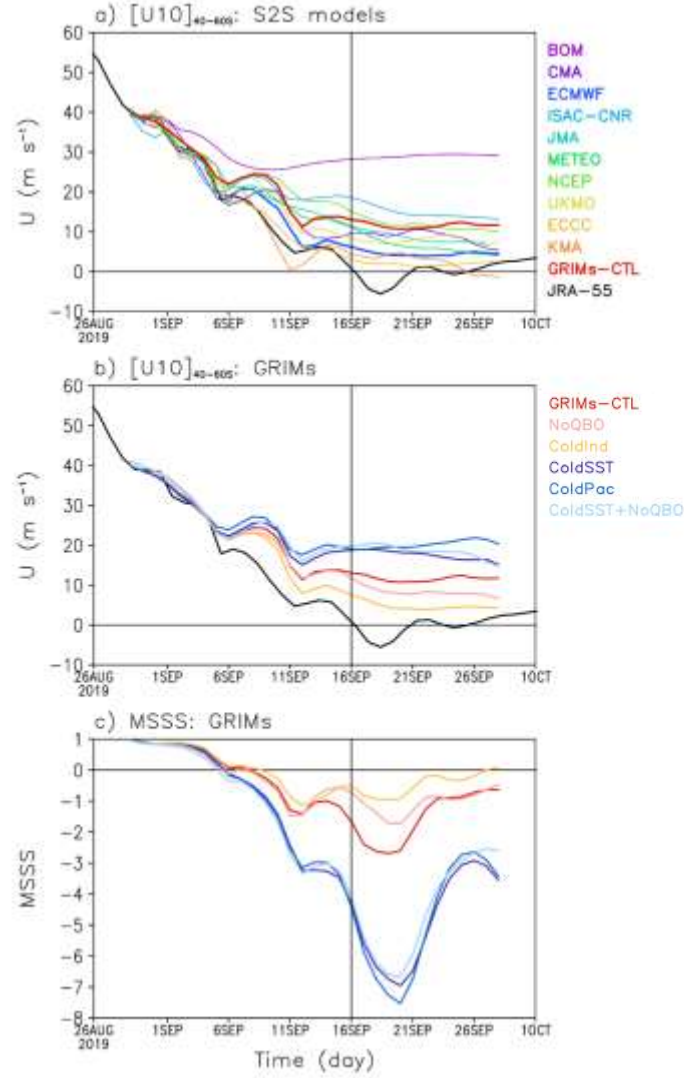


Figure 16. Temporal evolution of zonal-mean zonal wind at 10 hPa ( $[U10]$ ) averaged over  $40^{\circ}$ – $60^{\circ}$ S for (a) S2S models and GRIMs. (b) Same as (a) but for GRIMs experiments. (c) MSSS evolution is shown for six different GRIMs experiments. All forecasts are initialized on August 29, 2019 except for JMA model, which provides only the forecast on August 28, 2019. See the legend for the color information. Black lines indicate the reference from JRA-55. The vertical line indicates the SSW onset.



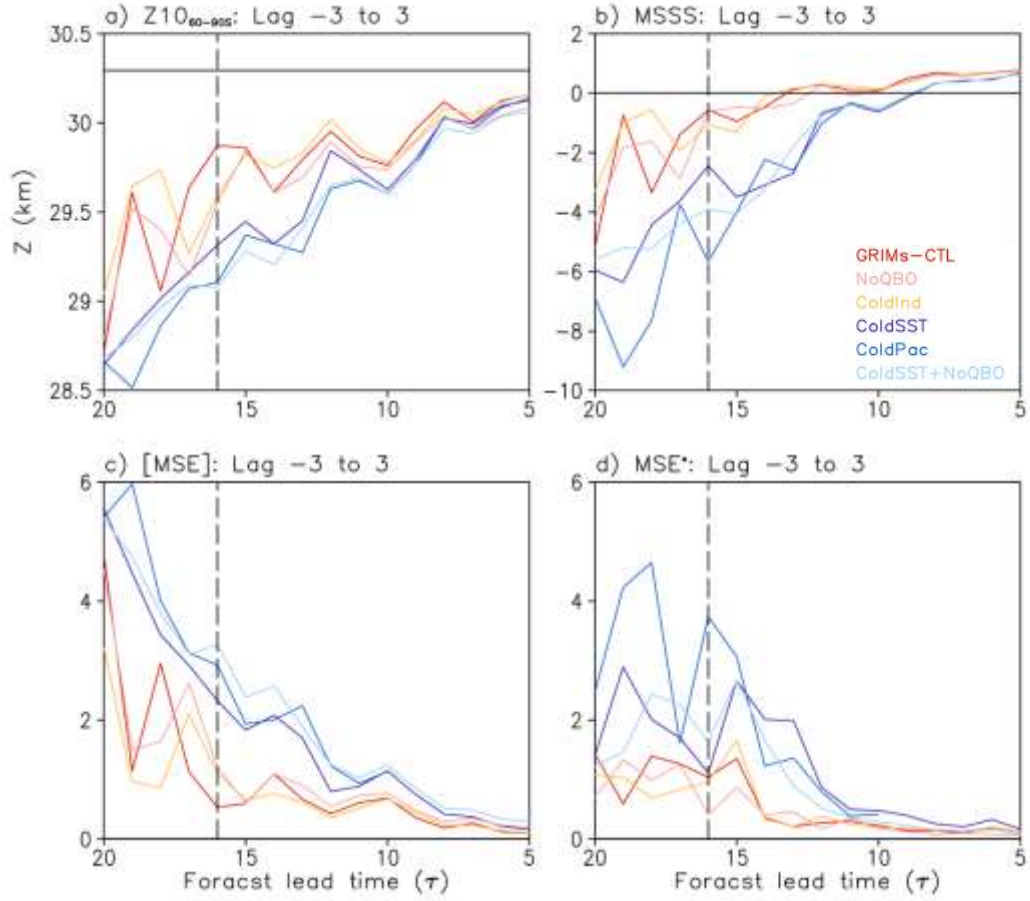


Figure 17. (a) Polar-cap averaged geopotential height ( $Z$ ), (b) MSSS, (c) zonal-mean MSE, and (d) eddy MSE at 10 hPa. All variables are averaged for  $\pm 3$  days with respect to the SSW onset. The zonal-mean and eddy MSE are normalized. The different colors denote the six experiments. Black horizontal lines in (a,b) are the reference values, JRA-55 and MSSS=0, respectively. The vertical dotted line indicates  $\tau=16$ . The lag indicates the days in advance of the SSW onset.

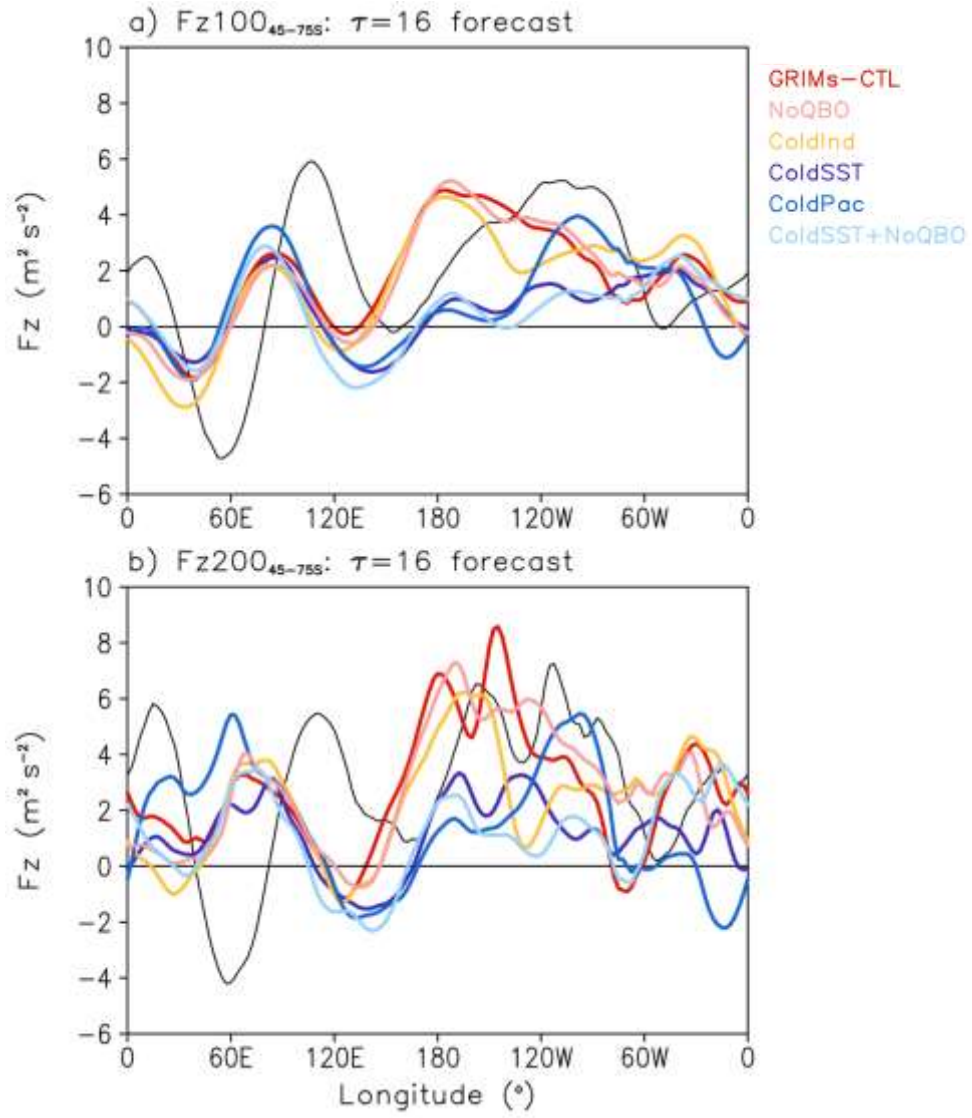


Figure 18. The vertical component of 3-D wave flux ( $Fz$ ) at (a) 100 and (b) 200 hPa averaged over  $45^{\circ}$ – $75^{\circ}$ S from 10 days before to the SSW onset in  $\tau=16$  forecast. Black line is JRA-55. The meaning of colors is the same as other Figures.

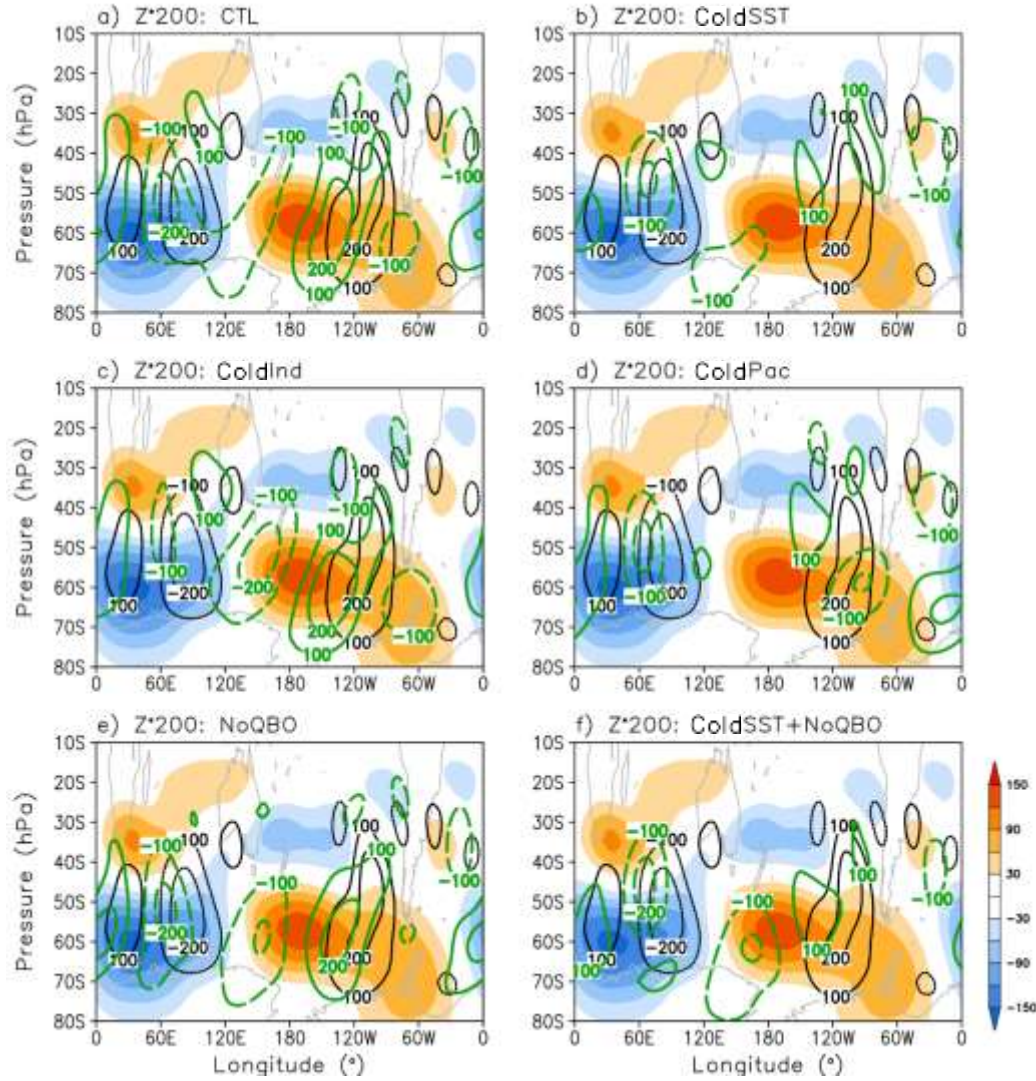


Figure 19. Climatological (shading) and anomalous (contour) geopotential height (Z) at 200 hPa averaged from 10 days before to the SSW onset in  $\tau=16$  forecast. The variable is a deviation from the zonal mean. The model results for six different experiments are denoted as green contours. Black contours indicate JRA-55.

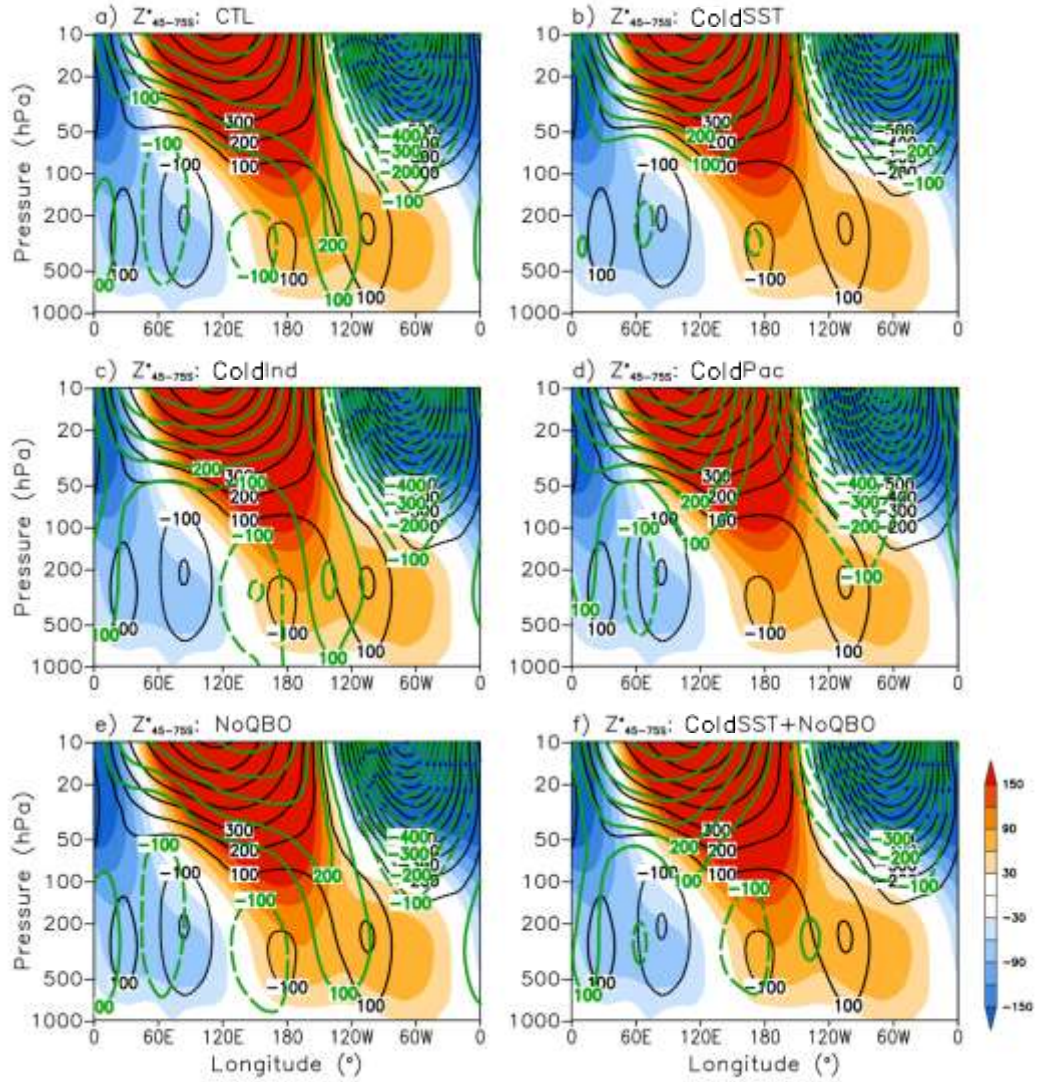


Figure 20. Same as Fig. 19 but for vertical structure of geopotential height (Z) averaged over 45°–75°S.



## **5. Role of ENSO in the NH SSW predictability**

### **5.1. Model mean biases of GRIMs**

The model drift is common in general circulation models (Charlton-Perez et al. 2013), and GRIMs is not an exception. Figures 21a,b show the zonal-mean zonal wind in JRA-55 (contour) and GRIMs biases from JRA-55 (shading) for all CTR runs (468 initializations for 18 SSW events) at  $j=10$  and 20 days. The positive biases are detected in the polar region in both hemispheres, and this becomes large with a function of the integration time step. This indicates the underestimated westerly in the SH and the overestimated easterly in the NH. The strengthened polar vortex in the stratosphere could be related to the estimation of wave activity in GRIMs. Indeed, overall wave activity presented by GRIMs is weaker than JRA-55 (Figs. 21c,d). At  $j=20$  days, the weak wave activity is more evident, and this directly explains the more strengthened polar vortex. In contrast to the stratosphere, the tropospheric biases are quite small. Although weak, the maximum tropospheric jet is observed at the relatively low latitude in GRIMs.

The polar vortex biases over the NH are quantified by averaging the geopotential height biases over 35-90°N. The model biases for all forecasts are shown at two different altitudes in Figs. 22a,c. It is observed that the stratospheric biases are quite strong compared to the tropospheric one. Especially, the

stratospheric biases are always negative for all forecasts (grey lines in Fig. 22a). In other words, GRIMs always predicts the stronger polar vortex than the observed one. This is a limitation of SSW prediction by GRIMs. The strong bias is also important in model development, but this prevents us from finding the causes of failure SSW prediction. The present study removes this strong bias from each forecast (black line in Fig. 22a). The forecast-mean bias is simply subtracted from each forecast bias (Figs. 22b,d). The overestimate of the polar vortex disappears after the bias correction (Fig. 22b). The impact of tropospheric bias correction is relatively weak (compare Fig. 22c to 22d). Hereafter, bias correction is applied for all analyses.

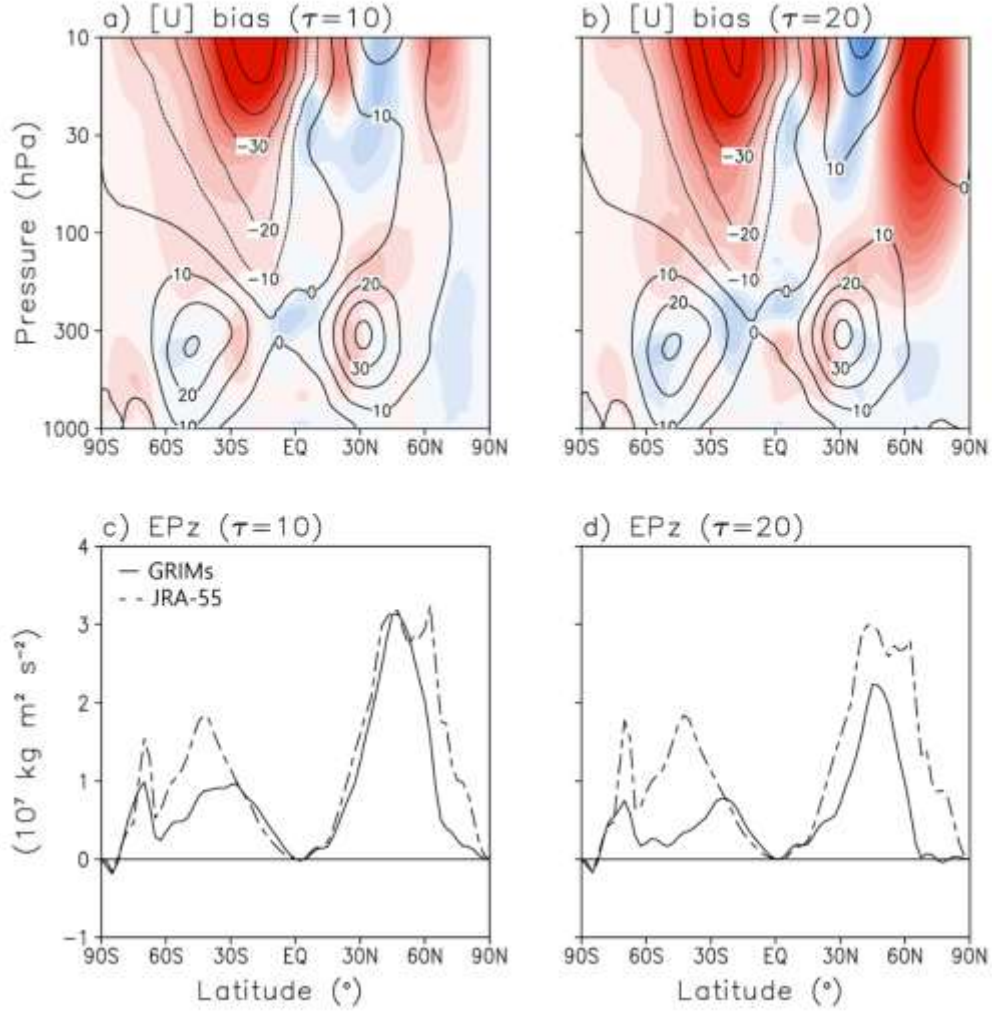


Figure 21. Zonal mean zonal wind ( $[U]$ ) biases at (a) 10-day and (b) 20-day ensemble forecast in CTR runs. The shading denotes  $[U]$  differences between GRIMs and JRA-55. 100-hPa EPz at (c) 10-day and (d) 20-day ensemble forecast in control runs and JRA-55 are shown as solid and dotted lines, respectively.

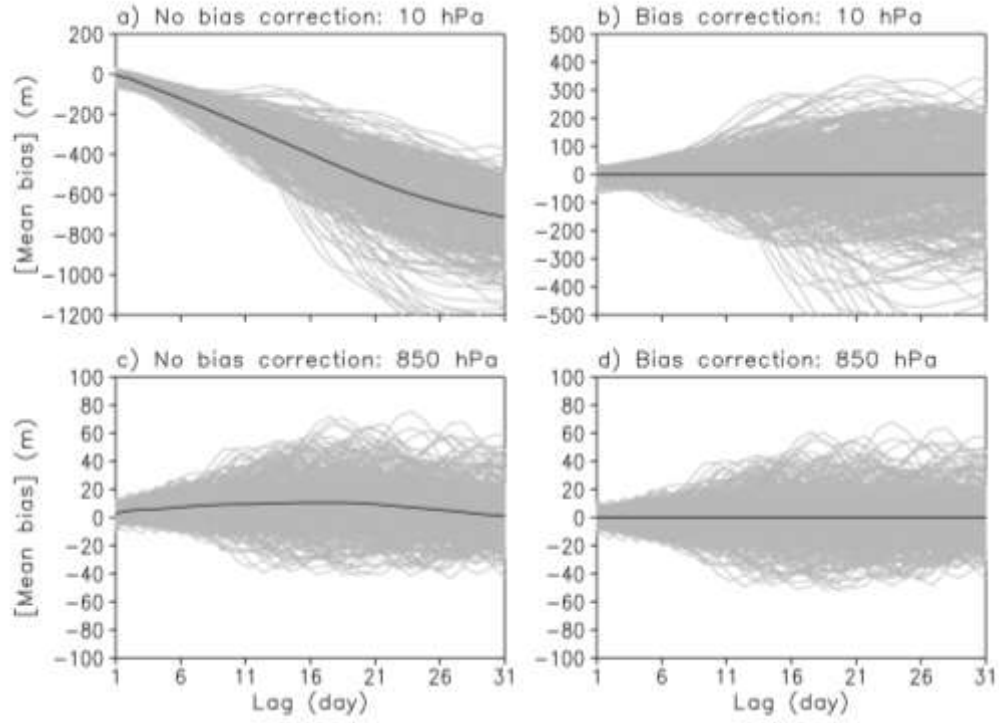


Figure 22. Area mean biases over 35-90°N (a, c) without and (b, d) with the bias correction for all simulations. The top and bottom panels show 10-hPa and 850-hPa geopotential height biases, respectively.



## 5.2. SSW prediction

The SSW prediction skill and the nature of the prediction error are evaluated primarily for two representative cases, the 2008 and 1989 SSW events. As summarized in Table 3, these events are the worst- and best-predicted events among the 18 SSW events. Both the 1989 and 1985 SSW events show the lowest MSSS prediction skill (10 days). The 1985 SSW event is briefly discussed later.

The temporal evolutions of U10 for the 2008 and 1989 SSW events are illustrated in Figs. 23a,b. As expected, significant decelerations are observed 15 days before the SSW onset (black vertical lines). Such deceleration is well predicted for the 2008 SSW event (Fig. 23a). All initializations, except for the  $\tau=21$  and  $\tau=24$  forecasts (dark purple and blue), show wind reversals. In contrast, the U10 evolution of the 1989 SSW event is poorly predicted when the model is initialized two to three weeks before the onset (blue and purple lines in Fig. 23b).

The MSSS shows consistent results with those of the U10 prediction (Figs. 23c,d). Most initializations reliably predict the polar vortex weakening during the 2008 SSW event (positive MSSS in Fig. 23c). The outlier is detected only in the  $\tau=24$  forecast. The prediction of the 1989 SSW event, however, shows a dramatic MSSS separation. The successful forecasts (yellow and red) are clearly separated from the unsuccessful forecasts (green and purple in Fig. 23d). The sharp decrease

in MSSS is particularly evident in the  $\tau=11$  forecast (cross mark in Fig. 23d).

Figures 23e,f present the two-dimensional version of Figs. 23c,d. These Figures concisely reveal the time evolution of the MSSS for each forecast (y-axis) as a function of the calendar date (x-axis). For all forecasts ( $\tau=0$  to 25) of the 2008 SSW event, the MSSS slowly decreases to 0.5 within 10-15 forecast days (red shading in Fig. 23e). The MSSS values in the  $\tau=13$  to 25 forecasts are mostly positive for the whole forecast period ( $j=0$  to 30; x-axis). These values become negative only in the middle of March in the  $\tau=3$  to 14 forecasts (blue shading in Fig. 23e). Since a negative MSSS appears after the onset, it does not affect the SSW prediction skill.

For the 1989 SSW event, the MSSS typically becomes negative three days before the SSW onset in the  $\tau=11$  to 23 forecasts (Fig. 23f). In contrast, a positive MSSS is maintained for all forecast days when the model is initialized immediately before the onset ( $\tau=0$  to 10). This result is consistent with the time scale of the SSW event. The breakdown of the polar vortex is typically maintained for one month (e.g., Baldwin and Dunkerton 2001). As such, the model initialized at or just before the SSW onset can maintain the stratospheric circulation for a much longer time than those in the  $\tau=10$  to 20 forecasts.

The prediction skill based on  $\text{MSSS} \geq 0$  is longer than that based on wind

reversal (see also Table 5). This result is related to the threshold problem of the wind reversal metric. As addressed earlier, the skill becomes low if the predicted U10 does not reach zero even if the model reasonably captures the wind deceleration and vortex breaking. This result indicates that the MSSS metric is more useful than the wind reversal metric when the spatial change in the polar vortex is considered.

Figure 24 quantifies the sources of the model prediction errors in terms of the normalized MSE, which are its zonal-mean and eddy components. By definition (see Eq. 1), the sum of the MSSS (Figs. 23e,f) and the normalized MSE (Figs. 24a,b) is one. As such, the meaning of the blue shading in Fig. 24 is opposite to that in Fig. 23. The normalized MSE can be explained by the combination of the zonal-mean and eddy errors (Figs. 24c-f). The 2008 SSW event is more sensitive to the zonal-mean errors than to the eddy errors, especially from 2 March to 15 March (Fig. 24c), with a minor contribution from eddy errors (Fig. 24e). The opposite result, however, is found for the 1989 SSW event. The eddy errors around the onset are relatively larger than the zonal-mean errors (compare Figs. 24d and 24f). Although large zonal-mean errors are detected after the onset in the  $\tau=24$  and  $\tau=25$  forecasts, they do not determine the prediction skill of the 1989 SSW event.

The eddy errors of the 1989 SSW prediction (Fig. 24f) are further decomposed into the eddy-phase and eddy-amplitude components as shown in

Figs. 25a,c. Although the eddy-phase errors are slightly more important than the eddy-amplitude errors after the onset (compare Figs. 25a and 25c), the eddy-amplitude errors play a more important role in determining the SSW prediction skill around the onset especially in the  $\tau=15$  to 22 forecasts (see the blue and yellow shading around the SSW onset in Fig. 25c). These errors are followed by the eddy-phase errors (blue shading in Fig. 25a). This result suggests that the poor prediction of the 1989 SSW event is primarily caused by the misrepresentation (more precisely underestimation) of the wave amplitude in the stratosphere.

It is not surprising to find that most eddy errors result from planetary-scale eddies (Figs. 25b and 25d) as synoptic-scale waves do not propagate into the winter stratosphere. Note that the  $k \geq 3$  eddy errors are mostly negligible (not shown). Figures 25b,d further reveal the relative importance of the  $k=1$  and  $k=2$  components. The  $k=2$  component causes errors immediately before the SSW onset (light blue shading around the onset in Fig. 25d), and the  $k=1$  errors are dominant after the onset. Here, it is noteworthy that the pattern of the  $k=1$  errors is similar to that of the eddy-phase errors (Figs. 25a,d), whereas  $k=2$  errors are mostly related to the eddy-amplitude errors (Figs. 25c,d). This result implies that the eddy-amplitude errors, which are the main factors determining the prediction skill, are associated with  $k=2$  wave prediction.

Although not shown, another poorly-predicted case, the 1985 SSW event, is

also evaluated. Eddy errors, especially eddy-phase errors, are dominant in this event. This result is somewhat different from that of the 1989 SSW prediction error. This difference indicates that the details of the eddy errors could vary from one case to another.

For the 1989 SSW event, the MSSS evolution dramatically changes from the last unsuccessful forecast ( $\tau=11$ ) to the first successful forecast ( $\tau=10$ ) (Fig. 23d). The same result is also found in the 1985 SSW prediction. This dramatic separation strongly suggests that the success of SSW prediction is not the result of model nature, such as model drift, but is likely caused by substantial changes in wave activities between the forecasts. This finding could be related to resolving the upward wave propagation because the SSW events are normally driven by them. Figure 26a shows the temporal-evolving vertical component of the three-dimensional wave activity flux (Takaya and Nakamura 2002) at 100 hPa averaged in the zonal direction ( $[Fz100]$ ). This property is physically identical to the vertical component of the Eliassen-Palm flux. It is observed that the vertical wave propagation, which is responsible for the 1989 SSW event, is amplified from 25 days before (27 January in Fig. 26a) to 5 days after the onset (26 February in Fig. 26a). The  $\tau=0$  to 9 forecasts (red to light green) well predicts this  $[Fz100]$  evolution (black). Although slightly underestimated, the  $\tau=10$  forecast (open circle) reasonably captures a maximum  $[Fz100]$  around 18 February, but the  $\tau=11$  forecast

(cross) significantly underestimates this wave propagation. Half of the wave amplitude is observed in the  $\tau=11$  forecast around the onset compared to that in the  $\tau=10$  forecast (Fig. 26a).

Figure 26b presents Fig. 26a without zonal mean in the reanalysis data (black) and the differences between the  $\tau=11$  and  $\tau=10$  forecasts (shading). The wave forcing is pronounced over North America to western Europe, especially during the 10 days before the SSW onset (see also Fig. 26c for the spatial distribution of the 10-day mean Fz100). This regional wave activity, which causes the vortex-split SSW event, is substantially underestimated in the  $\tau=11$  forecast (blue in Fig. 26b). This predicted Fz100 is approximately 30% smaller than that of the  $\tau=10$  forecast in the North Atlantic. The underestimation of wave activity where the wave propagation is amplified could be related to the large eddy-amplitude errors in the 1989 SSW event.

On the other hand, the 1985 SSW event is driven by vertically propagating waves not only in North America but also in eastern Eurasia (not shown). These wave propagations over both regions are well predicted when the model is initialized 10 days before the onset (the first successful prediction). However, the waves over North America are significantly underestimated in the  $\tau=11$  forecast (the last unsuccessful prediction). This result could lead to a large eddy-phase error (i.e., misrepresentation of  $k=2$  wave activity), resulting in an inaccurate prediction

of the vortex-split 1985 SSW event in the  $\tau=11$  forecast. It is still unclear why the model fails to predict the lower stratospheric wave activities around North America in both the 1989 and 1985 SSW events. This issue deserves further analysis.

The case study reveals that an estimate of the eddy component is important to the success of SSW prediction. To test the robustness of this finding, the same analysis is repeated for the six most and least skillful cases. As shown in Table 3, the top six prediction cases consist of four vortex-displacement and two vortex-split SSW events (events 5, 8, 10, 11, 14, and 16 in Table 3), and the bottom six prediction cases are composed of two vortex-displacement and four vortex-split events (events 3, 4, 7, 9, 15, and 17 in Table 3).

Figures 27a,b summarize the relative contributions of the zonal-mean and eddy errors in each SSW prediction. All variables are averaged for five days before the SSW onset. Here, the light blue marks indicate relatively short-term forecasts (small  $\tau$ ), while dark purple marks indicate long-term forecasts (large  $\tau$ ). For instance, a solid dark purple circle in Fig. 27a denotes the prediction for the 10th SSW event (23 January 1987), initialized at 25 days before the onset ( $\tau=25$ ). By taking the square root of a variable of interest, the distance from the origin to each mark is proportional to the normalized MSE (Figs. 27a,b) or the normalized MSE\* (Figs. 27c-f).

By definition, the overall MSE of the top six cases is smaller than that of the bottom six cases in the long-term forecasts (compare the distance from the origin to the dark purple in Figs. 27a,b). In both the top six and bottom six cases, the eddy errors are generally larger than the zonal-mean errors regardless of the forecast lead time (see most marks above the diagonal in Figs. 27a,b). The only exception is the 17th SSW event in 2009 (solid diamond in Fig. 27b), which shows larger zonal-mean errors in the  $\tau=20$  to 25 forecasts, but the eddy errors are still comparable to those of other events. This finding indicates that the total errors, the sum of the zonal-mean and eddy errors, in the 2009 SSW event are exceptionally larger than other events. It could be related to the fact that this event is particularly strong among the recent SSW events (Kuttipurath and Nikulin 2012).

Figures 27c,d show the relative importance of eddy-phase and eddy-amplitude errors. In the top six cases, eddy errors are dominated by eddy-phase errors. This result is also true in the bottom six cases at relatively short forecast lead times ( $\tau < 15$ ). The eddy-amplitude errors, however, rapidly increase with increasing forecast lead time in the bottom six cases. Except for the 4th and 9th SSW events, the eddy-amplitude errors become comparable or larger than the eddy-phase errors in most  $\tau > 20$  forecasts (Fig. 27d). This result indicates that the different compositions of the eddy errors between the top six and bottom six cases are mainly explained by rapidly developing eddy-amplitude errors in the long-



term forecast. It is also noteworthy that, unlike the top six cases, the details of eddy errors are dependent on the SSW events selected in the bottom six cases (see the widespread distribution in Fig. 27d). This result is consistent with that of the case study for the 1989 and 1985 SSW events.

The SSW event is typically driven by  $k=1$  and  $k=2$  wave activities (e.g., Charlton and Polvani 2007). Figure 27e shows that  $k=1$  errors are typically larger than  $k=2$  errors in the top six cases. However, there is no clear separation in the bottom six cases (Fig. 27f). Some events, such as the 3rd and 15th SSW events, show larger  $k=1$  than  $k=2$  components, while the opposite is observed in the 4th, 7th, and 17th SSW events. The SSW events with larger  $k=2$  than  $k=1$  error are often (but not always) identified as the vortex-split SSW events. The two SSW events with large  $k=1$  errors are vortex-displacement SSW events (see Table 3). These results indicate that the nature of eddy errors may depend on the SSW type in the bottom six cases. However, such a relationship does not hold in the top six cases.

The above result indicates that the SSW prediction skill of poorly-predicted SSW events could be improved by better predicting the zonal structure of planetary-scale waves (i.e., eddy-phase error). A more realistic prediction of the  $k=1$  wave is needed, although the  $k=2$  wave is non-negligible or even more important than the  $k=1$  wave in the selected SSW events, especially for the split

SSW events.

The vertical structure of the MSSS is further examined in this subsection for the 2008 and 1989 SSW events. As representative forecasts, the  $\tau=10$  and  $\tau=23$  forecasts are shown in Fig 6. These forecasts correspond to the first successful predictions of the 2008 and 1989 SSW events. The stratospheric prediction limit is not much larger than the tropospheric prediction limit in the  $\tau=10$  forecast of the 2008 SSW events (green line in Fig. 28a), but the 10-hPa to 30-hPa prediction limits in the 1989 SSW event are clearly larger than those at other lower levels (green line in Fig. 28b). Although not shown, the comparable prediction limit in the 2008 SSW event at whole vertical levels is related to the bias correction. Without conducting bias correction, larger prediction limits in the stratosphere are also detected in the 2008 SSW event. The clear differences between the 2008 and 1989 SSW events are observed at the low troposphere. The near-surface prediction limit in the 2008 SSW event is approximately 24 days, while it is approximately 14 days in the 1989 SSW event (compare green lines in Figs. 28a,b). The MSSS differences between the two events are shown in Fig. 28c. The largest difference in the MSSS is observed 10 days after the onset in the stratosphere. This MSSS difference in the stratosphere coincides with the tropospheric difference.

The MSSS difference between the two events is more evident in the  $\tau=23$  forecasts than in the  $\tau=10$  forecasts (Figs. 28d-f). As anticipated from Fig. 23, the

stratospheric prediction limit of the 2008 SSW event is much larger than that of the 1989 SSW event. For instance, the 10-hPa prediction limit for the 2008 SSW event (29 days) is approximately 1.53 times larger than that for the 1989 SSW event (19 days). Such difference is also found in the troposphere, especially after the onset (Fig. 28f). This result may imply that the tropospheric prediction is influenced by the success of stratospheric prediction. It is noted that the difference between the 2008 and 1989 SSW predictions is not evident immediately before the SSW onset.

By considering all available forecasts, we further investigate whether the tropospheric prediction limit is improved when the SSW event is successfully predicted. All forecasts are subdivided into HIT and MISS cases. The HIT cases are the initializations with the successful prediction of the SSW event. For instance, for the 1989 SSW event, which is predicted a maximum of 10 days in advance, the  $\tau=0$  to 10 forecasts (a total of 11 forecasts) are classified as HIT cases, and the other 15 forecasts ( $\tau=11$  to 25 forecasts) are MISS cases. The 292 HIT and 176 MISS cases are identified for all 18 SSW events.

Figure 29 shows the vertical structure of the MSSS for HIT cases, MISS cases, and their differences. The HIT cases exhibit an extended stratospheric prediction limit of more than 30 days, while the MISS cases exhibit a poor prediction limit of approximately 18 days in the stratosphere. A statistically significant skill

difference between HIT and MISS starts to appear at 12 forecast days ( $j=12$ ; Fig. 29c). Although small, a skill difference is also found in the troposphere. The 500-hPa prediction skill of HIT cases (12.3 days) is larger than that of MISS cases (approximately 11.0 days) in Fig. 29. This difference is likely related to the stratosphere-troposphere downward coupling during SSW events (Sigmond et al. 2013; Tripathi et al. 2015b; Domeisen et al. 2019), indicating that the tropospheric prediction limit could be improved by better predicting SSW events.

The error decomposition, presented in Figs. 24 and 25, is further applied to all pressure levels to find the main factors determining the skill difference in Fig. 29. Figure 30 indicates the zonal-mean and eddy components of a normalized MSE. Although the zonal-mean errors show significant differences between HIT and MISS cases (Fig. 30c), they appear only after 20 forecast days ( $j=20$ ) and are mostly confined to the stratosphere. The MSE differences in the lower stratosphere and the troposphere are primarily determined by eddy errors (Fig. 30f). This result is to some extent anticipated because  $MSE^*$  is generally much larger than  $[MSE]$  (compare the first and second rows of Fig. 30).

The  $MSE^*$  difference shown in Fig. 30f is mainly due to planetary-scale eddy errors. The planetary-scale eddy errors are important not only in the stratosphere but also in the troposphere (Figs. 30f,i). The synoptic-scale  $MSE^*$  does not show any significant difference between HIT and MISS cases until 20 forecast days (not

shown). Although further analyses are needed, this result is consistent with that of Martineau and Son (2015), who highlighted a critical role of planetary-scale waves in the vertical coupling associated with SSW events.

Marshall and Scaife (2010) and Taguchi (2016, 2018) indicated that vortex-split SSW events are typically challenging to predict. Their findings are revisited here by grouping SSW events into vortex-displacement and vortex-split events (Table 3). The overall results are summarized in Table 5. The prediction skill of the vortex-displacement SSW events (16.6 days) is slightly longer than that of vortex-split SSW events (13.9 days). Although these results are consistent with those of previous studies, the difference is not statistically significant because of the large variability among the events. Note that the skill difference increases when wind reversal is considered. Based on the wind reversal metric, the prediction skill of the vortex-displacement SSW events (11.7 days) is twice larger than that of the vortex-split SSW events (6.2 days). This result indicates that the skill difference between the two SSW types, reported in the previous studies, may be sensitive to the evaluation metric. When the SSW type is specifically separated into four types as following CPC19, the skill difference is more evident before (Table 6). For instance, DD and DS types (about 16 days), which have  $k=1$  type precondition, tend to show larger prediction skills than that of SS type (about 11 days). Here, SD type is excluded to explain it because of sample size. The above result suggests

that the morphology of the preconditioning polar vortex is more important than that of the evolving polar vortex in the SSW prediction.

Is the SSW prediction skill sensitive to a background state? Both ENSO and QBO have been widely reported to modulate the SSW frequency by changing planetary-scale wave activities. The SSW events are reliably predicted with a maximum lead time of 15.3 days during El Niño winters, and 14.7 days during La Niña winters (Table 5). The prediction skill during the westerly QBO winters and the easterly QBO winters are 14.4 and 16.0 days, respectively. These results may indicate that SSW events under a weak polar vortex state, such as those during El Niño and EQBO, are slightly better predicted than others. This is especially true during EQBO when both wind-reversal and MSSS metrics show higher SSW prediction skills than during WQBO. However, such an improved prediction skill during El Niño and EQBO winters is not statistically significant. It is concluded that the vortex morphology and stratospheric mean state marginally influence the deterministic SSW prediction skill.

Table 5. Mean and standard deviation of SSW prediction skills (unit: day). The numbers in parenthesis denote the number of SSW events for each SSW type and the background state.

	All (18)	SSW type		ENSO		QBO	
		D (9)	S (9)	EN (6)	LN (9)	WQBO (9)	EQBO (9)
Wind reversal	9.0±4.3	11.7±3.7	6.2±2.8	7.3±4.1	9.4±4.6	6.0±3.3	10.9±4.1
MSSS	15.2±3.6	16.6±3.7	13.9±3.1	15.3±2.1	14.7±4.4	14.4±3.0	16.0±4.0

Table 6. Same as Table 5 but for four SSW types.

	All (18)	SSW type			
		DD (9)	DS (5)	SS (3)	SD (1)
MSSS	15.2±3.6	16.3±3.8	16.6±1.6	10.7±0.9	12.0±0.0

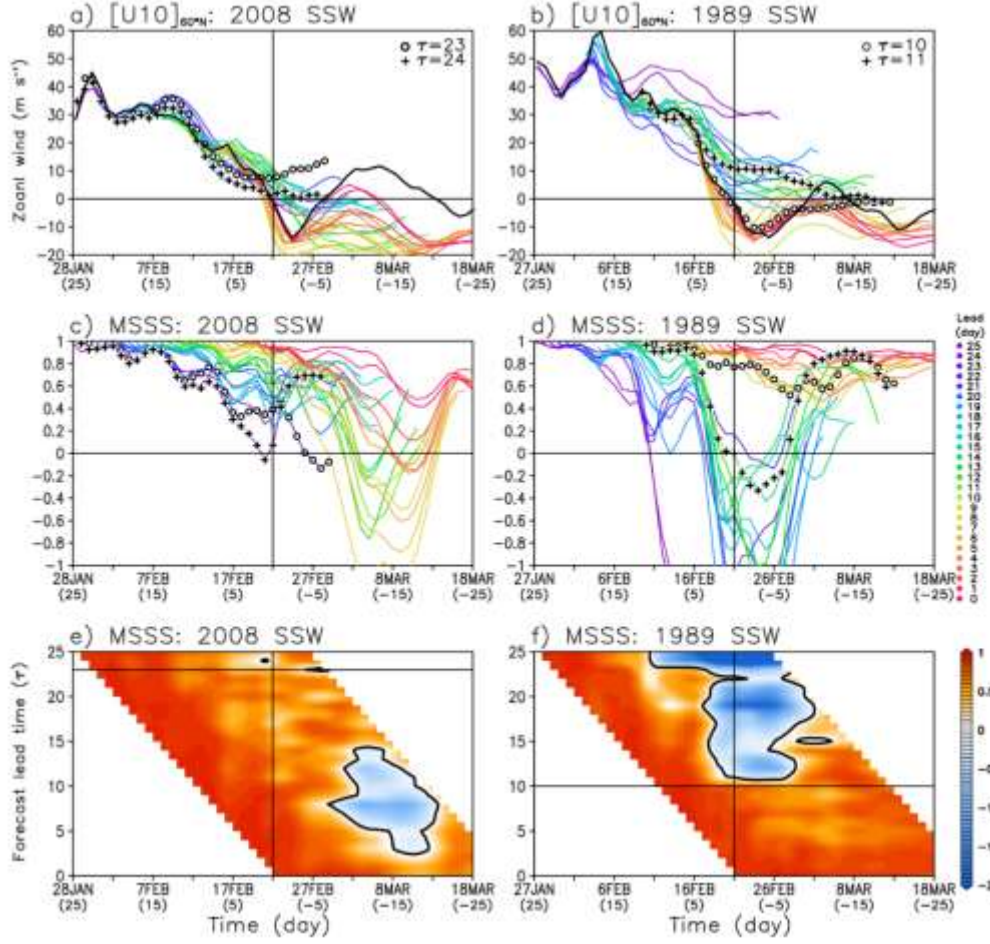


Figure 23. Time evolution of (a) 10-hPa zonal-mean zonal wind at 60°N ( $[U10]$ ) and (c) MSSS of 10-hPa geopotential height over 35°N-90°N for the 2008 SSW event. The forecasts at different lead times are denoted with different colors (see the labels on the right of the middle panel). The observed  $[U10]$  is shown in thick black lines in (a). Note that MSSS for the maximum lead time of successful forecast is denoted with open circles, while that for the minimum lead time for the unsuccessful forecast is denoted with crosses. (e) Two-dimensional MSSS with a prediction skill in a horizontal line. The thick contour indicates the zero line of MSSS. (b,d,f) Same as (a,c,e) but for the 1989 SSW event. In all panels, the vertical lines denote the SSW onset.



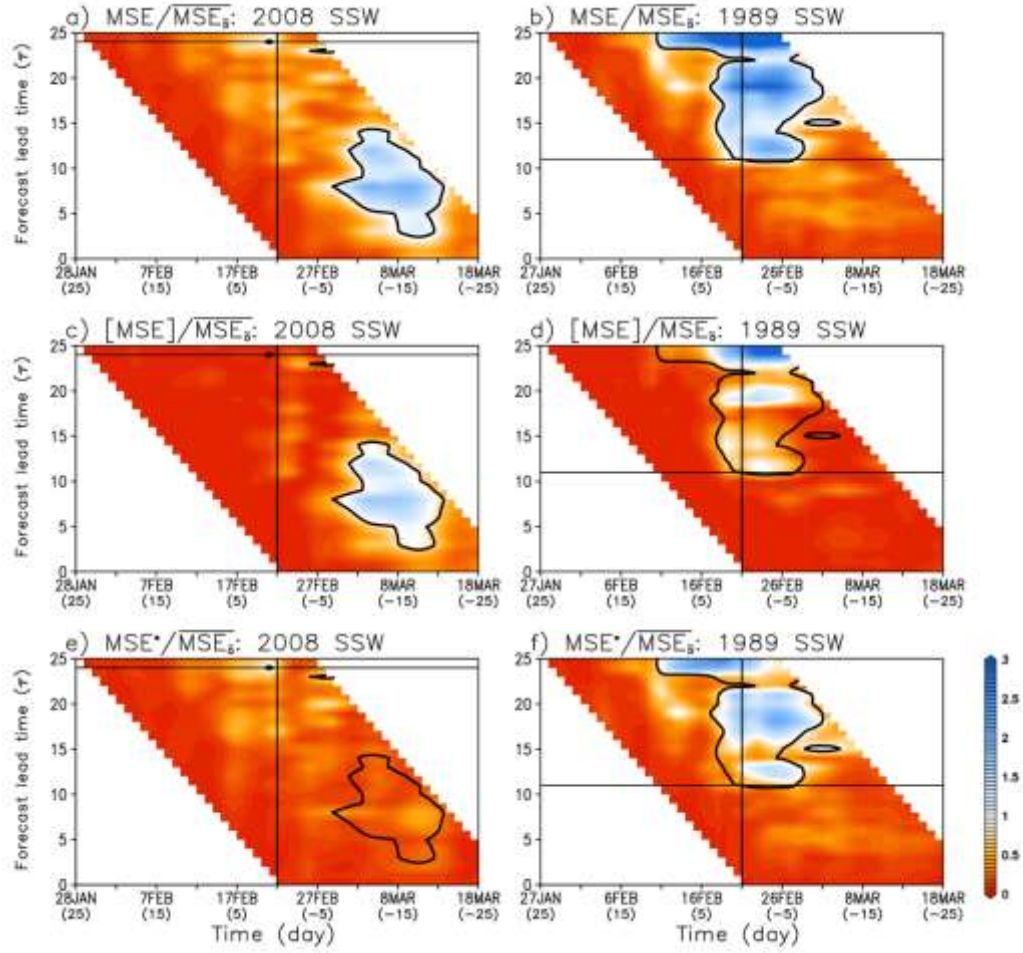


Figure 24. (a) MSE normalized by  $\overline{\text{MSE}_0}$  for the 2008 SSW event and (c,e) its zonal-mean and eddy components. In all panels, a solid black contour indicates the line of  $\text{MSE}/\overline{\text{MSE}_0} = 1$ , corresponding to  $\text{MSSS} = 0$ . (b,d,f) Same as (a,c,e) but for the 1989 SSW event.

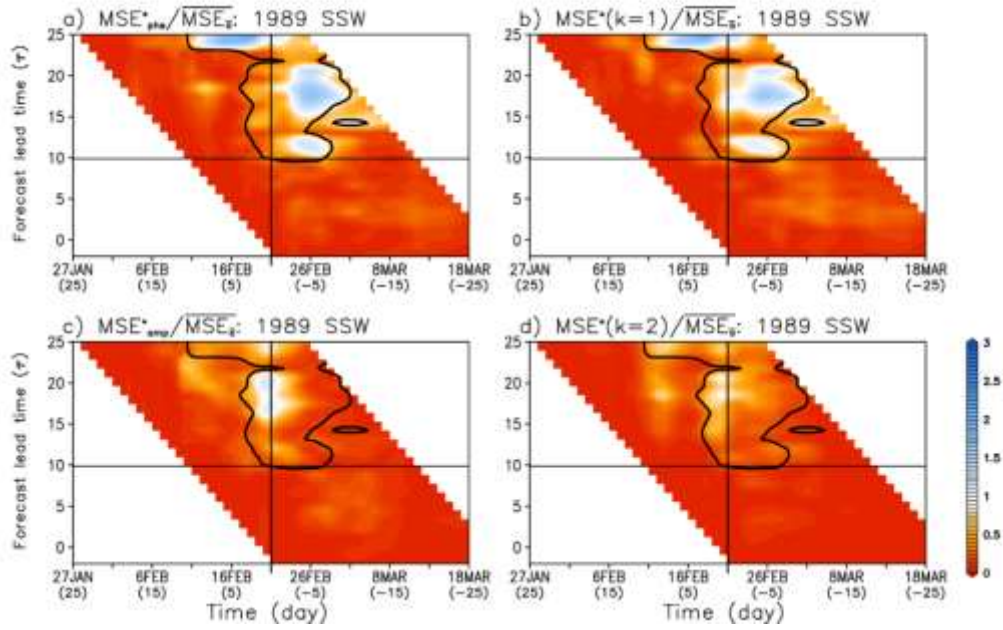


Figure 25. Same as Fig. 24f, but for the eddy-phase and eddy-amplitude errors and (b,d) for the eddy errors by the zonal-wavenumber one and two.

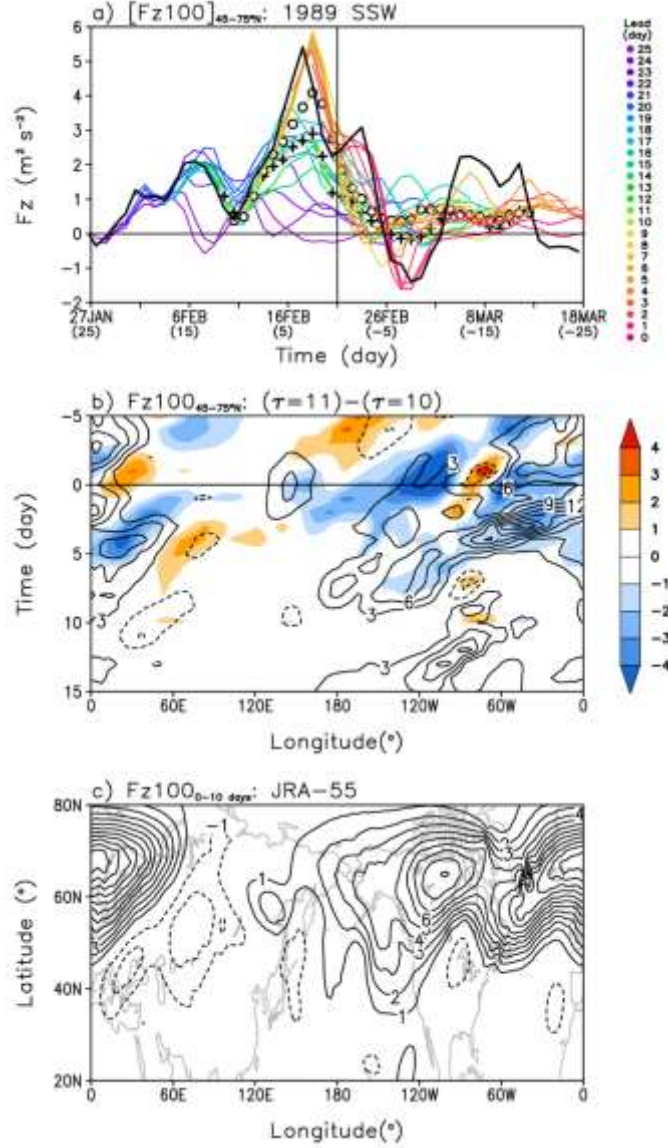


Figure 26. (a) Vertical component of 3-D wave activity flux at 100 hPa (Fz100) averaged over 45°N-75°N during the 1989 SSW event. Colored lines and symbols are the same as Fig. 23b (i.e., open circle and cross for  $\tau=10$  and  $\tau=11$  forecasts, respectively). (b) Fz100 averaged over 45°N-75°N, and (c) 10-days averaged Fz100 right before the onset from JRA-55. The shading in (b) denotes the Fz100 differences between  $\tau=11$  and  $\tau=10$  forecasts.

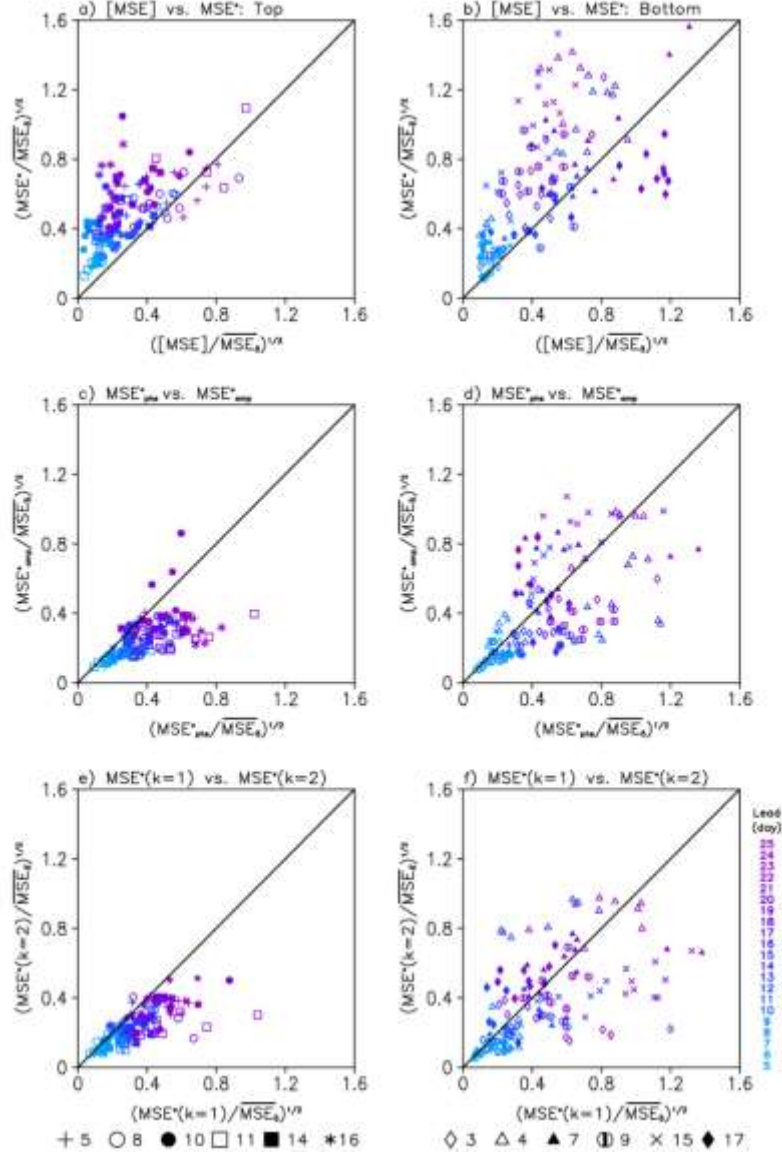


Figure 27. Relationship between (a) the zonal-mean and eddy errors, (c) the eddy-phase and eddy-amplitude errors, and (e) the zonal-wavenumber one and two for the top six SSW events. Event number, indicated in different symbols, corresponds to the one in Table 3. (b,d,f) Same as (a,c,e) but for the bottom six SSW events. The forecasts at different lead times are denoted in purple and blue. See the Figure legend.

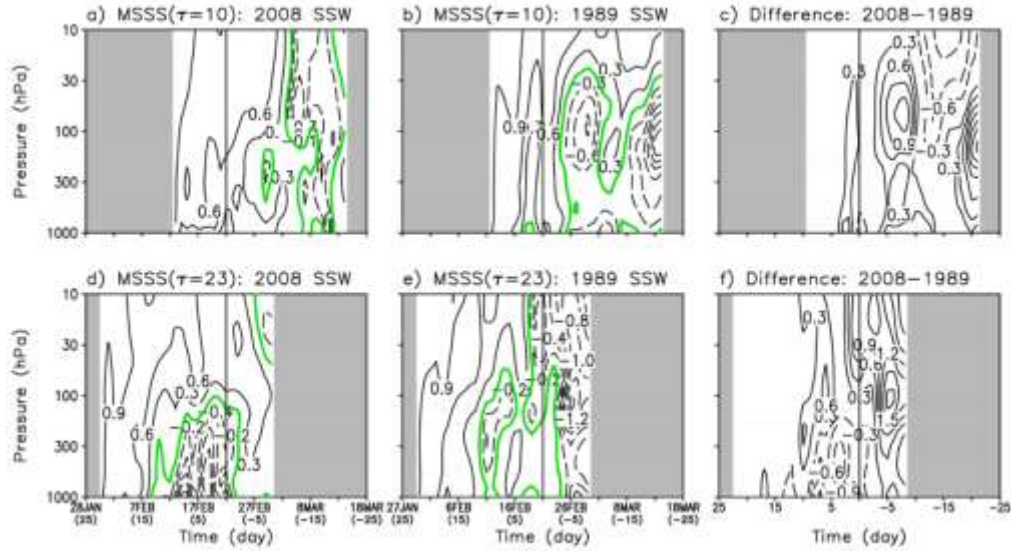


Figure 28. (a,d) Vertical structure of MSSS in  $\tau=10$  and  $\tau=23$  forecasts with a function of forecast day (j) for the 2008 SSW event, (b,e) for the 1989 SSW event, and (c,f) their differences. The green line denotes MSSS=0. The missing values are shaded in gray. The vertical lines denote the SSW onset.

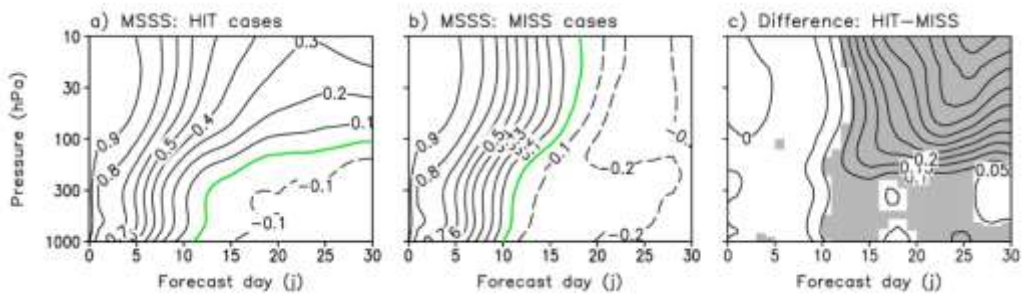


Figure 29. Vertical structure of MSSS as a function of forecast day (j) for (a) the successful (HIT) and (b) unsuccessful SSW predictions (MISS). Their difference is shown in (c). Green lines in (a,b) MSSS=0, and the shading in (c) denotes the value that is statistically significant at the 95% confidence level.

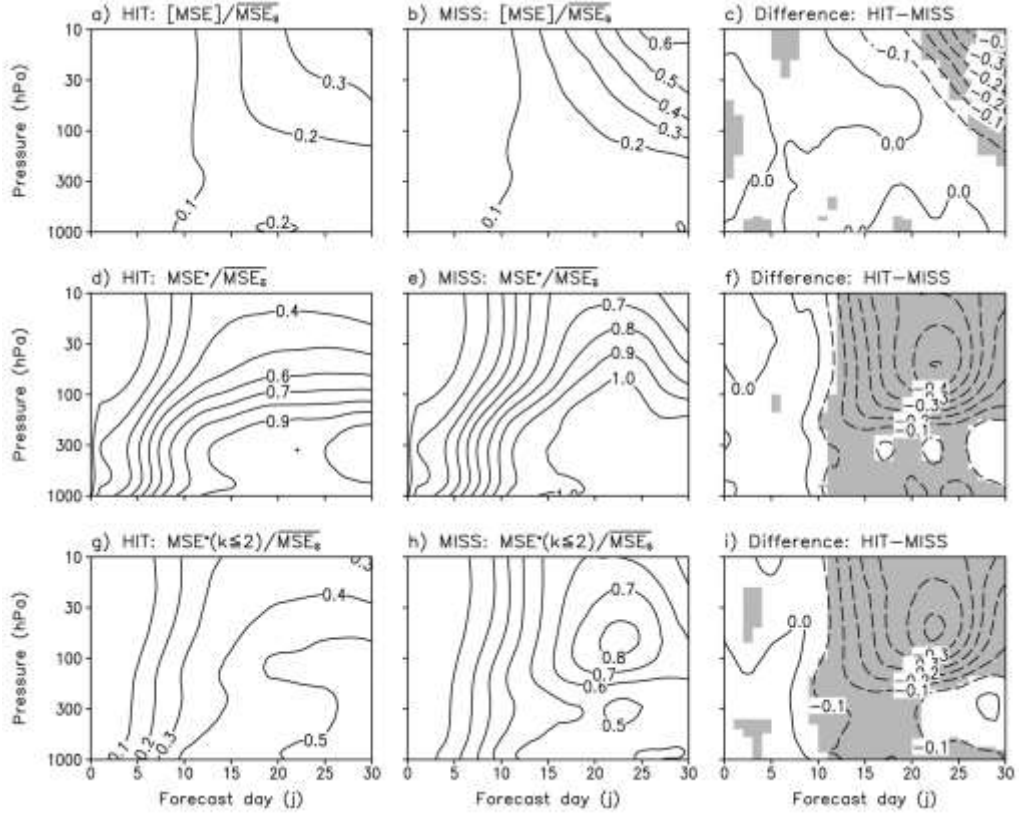


Figure 30. Same as Fig. 29, but for the MSE decomposition into (a-c) the zonal-mean and (d-f) eddy components. The eddy components by (g-i) zonal wavenumber one and two.



## 6. Summary and discussion

This study examines the role of the tropical SST variability in the SSW event and its predictability. Part 1 revisits the ENSO-SSW relationship and investigates the main source determining its decadal change in the NH. In part 2, the SH SSW event in 2019, the second event in the observation history, is examined, and the cause of this event is revealed by using the global forecast model. Lastly, the prediction skills of the NH SSW events for 18 events are evaluated in part 3.

This study finds the ENSO-SSW relationship found in the literature is limited to only U60 SSW definition but no other definitions. These definitions, covering the polar vortex variability at high latitude, show the linear ENSO-SSW relationship, which is the frequent SSW events only during El Niño winters not in other winters. The sensitivity of the ENSO-SSW relationship is due to the threshold problem of wind reversal definition and the choice of latitude. A recent modeling study paves our result (Polvani et al. 2017).

The ENSO-SSW relationship is recently broken (e.g., Hu et al. 2017), but the exact causes are still obscure. To clarify this, we investigate the possible factors to modulate the SSW frequency on the decadal timescale. Primarily, the impact of satellite data assimilation is investigated because the decadal changes in the ENSO-SSW relationship is observed during the satellite era. However, any

difference in the ENSO-SSW relationship between JRA-55 and JRA-55C is not found. The PDO is another possible factor to control SSW frequency because Woo et al. (2015) suggested a weak hint of PDO modulation in SSW frequency. This study consistently finds more frequent SSW events during the positive PDO winters than other winters. Because PDO has the decadal changes, the recent increase of La Niña-winter SSW events is possibly related to the PDO-SSW relationship. However, we cannot find any significant correlation between positive PDO and La Niña winters. This indicates that the PDO-SSW relationship does not affect the recently-broken ENSO-SSW relationship. To discover the exact cause of the nonstationary ENSO-SSW relationship, other factors, such as QBO, are further investigated.

The role of ENSO in the SH SSW event is also investigated in this study. Because of the small sample size, the 2019 SSW event in SH is only considered. To find the key driver leading to the 2019 SSW event in the SH, GRIMs is used with six different experiments. The predictability of this event in GRIMs is in a range of inter-model spread among the nine S2S models. This indicates that GRIMs is a reliable model to capture the polar vortex weakening and related wave activities during the 2019 SSW event. Including a control experiment, six different experiments are conducted in this study. Three experiments (ColdSST, ColdInd, and ColdPac) are directly related to prescribing cold SST condition in August. The



NoQBO experiment is conducted by linearly removing the August QBO effect in the initial conditions. The last experiment (ColdSST+NoQBO) is performed to examine the combined effect of SST and QBO in SSW prediction.

Both zonal-mean and zonally-asymmetric geopotential height is relatively well predicted when the observed Pacific SST is prescribed (CTR, ColdInd, and NoQBO; the best prediction group). On the other hand, other experiments (ColdSST, ColdPac, and ColdSST+NoQBO; the worst prediction group) entirely underestimate the polar vortex weakening. As expected, the prediction of the polar vortex weakening is related to the estimation of wave activities from the troposphere. The amplified wave activities over two regions, the Pacific and Indian Oceans, are observed during the 2019 SSW event. All experiments consistently predict the Indian Ocean wave activities, whereas these over the Pacific Ocean differ from one experiment to another. Notably, the Pacific wave activities are well represented by the best prediction group. However, the worst prediction group totally fails to predict them. This difference in the predicted wave activities is dictated by the prediction of constructive linear interference for a vertically westward tilt of geopotential height. More precisely, the anomalous Pacific high in the troposphere, which shows a constructive linear interference with climatological  $Z$ , is well captured by the experiments with the observed Pacific SST. However, this is not found in other experiments with reduced Pacific SST,

La Niña-like experiment. Our findings suggest that the Pacific SST plays a key driver of the 2019 SSW event by mediating the Pacific tropospheric wave activities. This is a contrast result to the 2002 SSW event in the SH, which is mainly modulated by the stratospheric condition.

In Part 3, the prediction skills of the SSW events are evaluated by using GRIMs. Unlike previous studies based on small numbers of SSW events, a total of 18 mid-winter SSW events are examined. Specifically, the spatial distribution of the 10-hPa geopotential height is evaluated by computing MSSS in the northern extratropics. The GRIMs can predict the SSW events on average with a maximum lead time of 15.2 days. However, the spread in the prediction skill among the events is quite large, ranging from 10 to 23 days. The two-week prediction skill and its large variability among the SSW events ( $15.2 \pm 3.6$ ) are consistent with those in a previous study (e.g., Tripathi et al. 2015a). The decomposition of model errors into the zonal-mean and eddy errors reveals that such a large spread in the prediction skill mostly results from the eddy components. Although the importance of eddies in SSW prediction has been partly discussed in Taguchi (2016), the present study more directly relates the decomposed eddy errors to the SSW prediction skill. The eddy-phase errors, related to the misrepresentation of planetary-scale wave activities, play important roles in determining the prediction skill of the relatively well-predicted SSW events. Poorly-predicted SSW events

are associated with both eddy-amplitude and eddy-phase errors. The former error is typically dominant, but the latter error is sometimes important in the selected SSW events.

The SSW prediction skill is weakly sensitive to the SSW type and background state. The vortex-displacement SSW events are better predicted than the vortex-split SSW events (e.g., Taguchi 2016). Likewise, the SSW events during easterly QBO winters are slightly better predicted than those during westerly QBO winters. However, their skill differences are not statistically significant. This is also true in those during different ENSO winters.

## References

- Baldwin, M. P., and T. J. Dunkerton, 1998: Quasi-biennial modulation of the Southern Hemisphere stratospheric polar vortex. *Geophys. Res. Lett.*, **25**, 3343–3346, doi: 10.1029/98gl02445.
- Baldwin, M. P., and T. J. Dunkerton, 2001: Stratospheric harbingers of anomalous weather regimes. *Science*, **294**, 581-584, doi:10.1126/science.1063315.
- Baldwin, M. P., T. Hirooka, A. O'Neill, and S. Yoden, 2003: Major stratospheric warming in the Southern Hemisphere in 2002: Dynamical aspects of the ozone hole split. *SPARC Newsletter*, **20**, 24-26.
- Black, R. X., and B. A. McDaniel, 2004: Diagnostic case studies of the Northern Annular Mode. *J. Climate*, **17**, 67-80, doi:10.1175/1520-0442(2004)017<3990:DCSOTN>2.0.CO;2.
- Butler, A. H., and L. M. Polvani, 2011: El Niño, La Niña, and stratospheric sudden warmings: A reevaluation in light of the observational record. *Geophys. Res. Lett.*, **38**, L13807, doi:10.1029/2011GL048084.
- Butler, A. H., L. M. Polvani, and C. Deser, 2014: Separating the stratospheric and tropospheric pathways of El Niño–Southern Oscillation teleconnections. *Environ. Res. Lett.*, **9**, 024014, doi:10.1088/1748-9326/9/2/024014.
- Butler, A. H., D. J. Seidel, S. C. Hardiman, N. Butchart, T. Birner, and A. Match, 2015: Defining sudden stratospheric warmings. *Bull. Amer. Meteor. Soc.*, **96**, 1913-1928, doi:10.1175/BAMS-D-13-00173.1.
- Calvo, N., R. García-Herrera, and R. R. Garcia, 2008: The ENSO signal in the

- stratosphere. *Ann. N. Y. Acad. Sci.*, **1146**, 16-31, doi:10.1196/annals.1446.008.
- Charlton, A. J., and L. M. Polvani, 2007: A new look at stratospheric sudden warmings. Part I: Climatology and modeling benchmarks. *J. Climate*, **20**, 449-469, doi:10.1175/JCLI3996.1.
- Charlton-Perez, and Coauthors, 2013: On the lack of stratospheric dynamical variability in lo-top versions of the CMIP5 models. *J. Geophys. Res.*, **118**, 2494-2505, doi:10.1002/jgrd.50125.
- Cohen, J. M., Barlow, P. J. Kushner, and K. Saito, 2007: Stratosphere-troposphere coupling and links with Eurasian land surface variability. *J. Climate*, **20**, 5335-5343, doi:10.1175/2007JCLI1725.1.
- Choi, H., B.-M. Kim, and W. Choi, 2019: Type classification of sudden stratospheric warming based on pre- and postwarming periods. *J. Climate*, **32**, 2349– 2367, doi:10.1175/JCLI-D-18-0223.1.
- Domeisen, D. I., C. I. Garfinkel, and A. H. Butler, 2019: The teleconnection of El Niño Southern Oscillation to the stratosphere. *Reviews of Geophys.*, **57**, 5-47, doi:10.1029/2018RG00596.
- Esler, J. G., L. M. Polvani, and R. K. Scott, 2006: The Antarctic sudden stratospheric warming of 2002: A self-tuned resonance? *Geophys. Res. Lett.*, **33**, L12804, doi:10.1029/2006GL026034.
- Garfinkel, C. I., A. H. Butler, D. W. Waugh, M. M. Hurwitz, and L. M. Polvani, 2012: Why might stratospheric sudden warmings occur with similar frequency in El Niño and La Niña winters? *J. Geophys. Res.*, **117**, D19106, doi:10.1029/2012JD017777.

- Goddard, L., and Coauthors, 2013: A verification framework for interannual-to-decadal predictions experiments. *Climate Dyn.*, **40**, 245-272, doi:10.1007/s00382-012-1481-2.
- Hendon, H. H., and Coauthors, 2019: Rare forecasted climate event under way in the Southern Hemisphere. *Nature*, **573**, 495, doi:10.1038/d41586-019-02858-0.
- Hong, S.-Y., and Coauthors, 2013: The global/regional integrated model system (GRIMs). *Asia-Pac. J. Atmos. Sci.*, **49**, 219-243, doi: 10.1007/s13143-013-0023-0.
- Horel, J. D., and J. M. Wallace, 1981: Planetary-scale atmospheric phenomena associated with the Southern Oscillation. *Mon. Wea. Rev.*, **109**, 813-829, doi:10.1175/1520-0493(1981)109<0813:PSAPAW>2.0.CO;2.
- Hoskins, B., 2013: The potential for skill across the range of the seamless weather-climate prediction problem: a stimulus for our science. *Q. J. R. Meteorol. Soc.*, **139**, 573-584, doi:10.1002/qj.1991.
- Huang, B., and Coauthors, 2017: Extended reconstructed sea surface temperature version 5 (ERSSTv5): Upgrades, validations, and intercomparisons. *J. Climate*, **30**, 8179-8205, doi:10.1175/JCLI-D-16-0836.1.
- Hurwitz, M. M., P. A. Newman, L. D. Oman, and A. M. Molod, 2011: Response of the Antarctic stratosphere to two types of El Niño events. *J. Atmos. Sci.*, **68**, 812–822, doi:10.1175/2011JAS3606.1.
- Ichimaru, T., S. Noguchi, T. Hirooka, and H. Mukougawa, 2016: Predictability changes of stratospheric circulations in Northern Hemisphere winter. *J.*

- Meteorol. Soc. Japan*, **94**, 7-24, doi:10.2151/jmsj.2016-001.
- Kim, B.-M., S.-W. Son, S.-K. Min, J.-H. Jeong, S.-J. Kim, X. Zhang, T. Shim, and J.-H. Yoon, 2014: Weakening of the stratospheric polar vortex by Arctic sea-ice loss. *Nat. Commun.*, **4**, 4646, doi:10.1038/ncomms5646.
- Kim, J., S.-W. Son, E. P. Gerber, and H.-S. Park, 2017: Defining sudden stratospheric warmings in models: Accounting for biases in model climatologies. *J. Climate*, **30**, 5529-5546, doi:10.1175/JCLI-D-16-0465.1.
- Kobayashi, C., H. Endo, Y. Ota, S. Kobayashi, H. Onoda, Y. Harada, K. Onogi, and H. Kamahori, 2014: Preliminary results of the JRA-55C, an atmospheric reanalysis assimilating conventional observations only. *SOLA*, **10**, 78-82, doi:10.2151/sloa.2014-016.
- Kobayashi, S., and Coauthors, 2015: The JRA-55 reanalysis: General specifications and basic characteristics. *J. Meteor. Soc. Japan*, **93**, 5-48, doi: 10.2151/jmsj.2015-001.
- Koo, M.-S., and S.-Y. Hong, 2013: Double Fourier series dynamical core with hybrid sigma-pressure vertical coordinate. *Tellus A: Dynamic Meteorology and Oceanography*, **65**, 19851, doi: 10.3402/tellusa.v65i0. 19851.
- Kuroda, Y. (2018). On the origin of the solar cycle modulation of the southern annular mode. *J. Geophys. Res.*, **123**, 1959-1969, doi:10.1002/2017JD027091.
- Lim, E. P., H. H. Hendon, and D. W. J. Thompson, 2018: Seasonal evolution of stratosphere-troposphere coupling in the southern hemisphere and implications for the predictability of surface climate. *J. Geophys. Res.*, **123**,

- 12002–12016, doi:10.1029/2018jd0293.
- Lim, E. P., and Coauthors, 2019: Australian hot and dry extremes induced by weakenings of the stratospheric polar vortex. *Nat. Geosci.*, **12**, 896–901, doi: 10.1038/s41561-019-0456-x.
- Lim, E.-P., and Coauthors, 2020a: The 2019 Antarctic sudden stratospheric warming. *SPARC Newsletter*, **54**, 10-13.
- Lim, E.-P., and Coauthors, 2020b: The 2019 Southern Hemisphere polar stratospheric warming and its impacts. Submitt. to *Bull. Amer. Meteor. Soc.*.
- Manzini, E., M. A. Giorgetta, M. Esch, L. Kornblueh, and E. Roeckner, 2006: The Influence of sea surface temperatures on the Northern winter stratosphere: Ensemble simulations with the MAECHAM5 Model. *J. Climate*, **19**, 3863-3881, doi:10.1175/JCLI3826.1.
- Marshall, A.G., and A. A. Scaife, 2010: Improved predictability of stratospheric sudden warming events in an atmospheric general circulation model with enhanced stratospheric resolution. *J. Geophys. Res.*, **115**, D16114, doi:10.1029/2009JD012643.
- Martineau, P., and S.-W. Son, 2015: Onset of circulation anomalies during stratospheric vortex weakening events: The role of planetary-scale waves. *J. Climate*, **28**, 7347-7370, doi:10.1175/JCLI-D-14-00478.1.
- Matsuno, T., 1971: A dynamical model of the stratospheric sudden warming. *J. Atmos. Sci.*, **28**, 1479-1494, doi: 10.1175/1520-0469(1971)028<1479:ADMOTS>2.0.CO;2.
- Mukougawa, H., and T. Hirooka, 2004: Predictability of stratospheric sudden



- warming: A case study for 1998/99 winter. *Mon. Wea. Rev.*, **132**, 1764-1776, doi:10.1175/1520-0493(2004)132<1764:POSSWA>2.0.CO;2.
- Naujokat, B., 1986: An update of the observed quasi-biennial oscillation of the stratospheric winds over the tropics. *J. Atmos. Sci.*, **43**, 1873-1877, doi:10.1175/1520-0469(1986)043<1873:AUTOQ>2.0.CO;2.
- Nishii, K., and H. Nakamura, 2004: Tropospheric influence on the diminished Antarctic ozone hole in September 2002. *Geophys. Res. Lett.*, **31**, L16103, doi:10.1029/2004GL019532.
- Palmeiro, F. M., D. Barriopedro, R. García-Herrera, and N. Calvo, 2015: Comparing sudden stratospheric warming definitions in reanalysis data. *J. Climate*, **28**, 6823-6840, doi:10.1175/JCLI-D-15-0004.1.
- Poli, P., and Coauthors, 2013: The data assimilation system and initial performance evaluation of the ECMWF pilot reanalysis of the 20th-century assimilating surface observations only (ERA-20C). *ECMWF ERA Rep.*, **14**, 59pp.
- Polvani, L. M., and D. W. Waugh, 2004: Upward wave activity flux as a precursor to extreme stratospheric events and subsequent anomalous surface weather regimes. *J. Climate*, **17**, 548–3554, doi:10.1175/1520-0442(2004)017,3548:UWAFAA.2.0.CO;2.
- Polvani L. M., L. Sun, A. H. Butler, J. H. Richter, and C. Deser, 2017: Distinguishing stratospheric sudden warming from ENSO as key drivers of wintertime climate variability over the North Atlantic and Eurasia. *J. Climate*, **30**, 1959-1969, doi:10.1175/JCLI-D-16-0277.1.
- Rao, J., C. I. Garfinkel, I. P. White, and C. Schwartz, 2020: The Southern

- Hemisphere sudden stratospheric warming in September 2019 and its predictions in S2S models. *J. Geophys. Res.*, doi:10.1002/essoar.10502478.1.
- Renwick, J. A., and M. J. Revell, 1999: Blocking over the South Pacific and Rossby wave propagation. *Mon. Wea. Rev.*, **127**, 2233-2247, doi:10.1175/1520-0493(1999)127<2233:BOTSPA>2.0.CO;2.
- Saji, N. H., B. N. Goswami, P. N. Vinayachandran, and T. Yamagata, 1999: A dipole mode in the tropical Indian Ocean. *Nature*, **401**, 360-363, doi:10.1038/43854.
- Shen, X., L. Wang, and S. Osprey, 2020: Tropospheric forcing of the 2019 Antarctic sudden stratospheric warming. *Geophys. Res. Lett.*, **47**, e2020GL089343, doi:10.1029/2020GL089343.
- Sigmond, M., J. F. Scinocca, V. V. Kharin, and T. G. Shepherd, 2013: Enhanced seasonal forecast skill following stratospheric sudden warmings. *Nat. Geosci.*, **6**, 98-102, doi: 10.1038/ngeo1698.
- Son, S.-W., H. Kim, K. Song, S.-W. Kim, P. Martineau, Y.-K. Hyun, and Y. Kim, 2020: Extratropical prediction skill of the subseasonal-to-seasonal (S2S) prediction models. *J. Geophys. Res.*, **125**, e2019JD031273, doi:10.1029/2019JD031273.
- Song, K., and S.-W. Son, 2018: Revisiting the ENSO-SSW relationship. *J. Climate*, **31**, 2133-2143, doi:10.1175/JCLI-D-17-0078.1.
- Song, K., S.-W. Son, A. Charlton-Perez, 2020: Deterministic prediction of stratospheric sudden warming events in the Global/Regional Integrated Model system (GRIMs), *Climate Dyn.*, **55**, 1209-1123. doi:10.1007/s00382-

020-05320-4.

- Stan, C., and D. M. Straus, 2009: Stratospheric predictability and sudden stratospheric warming events. *J. Geophys. Res.*, **114**, D12103, doi:10.1029/2008JD011277.
- Smith, T. M., R. W. Reynolds, T. C. Peterson, and J. Lawrimore, 2008: Improvements NOAAs historical merged land-ocean temp Analysis, 1880-2006. *J. Climate*, **21**, 2283-2296, doi:10.1175/2007JCLI2100.1.
- Smith, K. L., and P. J. Kushner, 2012: Linear interference and the initiation of extratropical stratosphere-troposphere interactions. *J. Geophys. Res.*, **117**, D13107, doi:10.1029/2012JD017587.
- Taguchi, M., and D. L. Hartmann, 2006: Increased occurrence of stratospheric sudden warmings during El Niño as simulated by WACCM. *J. Climate*, **19**, 324-332, doi:10.1175/JCLI3655.1.
- Taguchi, M., 2015: Changes in frequency of major stratospheric sudden warmings with El Niño/Southern Oscillation and Quasi-Biennial Oscillation. *J. Meteor. Soc. Japan*, **93**, 99-115, doi:10.2151/jmsj.2015-007.
- Taguchi, M., 2016: Connection of predictability of major stratospheric sudden warmings to polar vortex geometry. *Atmos. Sci. Lett.*, **17**, 33-38, doi:10.1002/asl.595.
- Taguchi, M., 2018: Comparison of subseasonal-to-seasonal model forecasts for major stratospheric sudden warmings. *J. Geophys. Res.*, **123**, 10231-10247, doi:10.1029/2018JD028755.
- Takaya, K, and H. Nakamura, 2002: A formulation of a phase-independent wave-

- activity flux for stationary and migratory quasigeostrophic eddies on a zonally varying basic flow. *J. Atmos. Sci.*, **58**, 608-627, doi:10.1175/1520-0469(2001)058<0608:AFOAPI>2.0.CO;2.
- Tripathi, O. P., and Coauthors, 2015a: The predictability of the extratropical stratosphere on monthly time-scales and its impact on the skill of tropospheric forecasts. *Q. J. R. Meteorol. Soc.*, **141**, 987-1003, doi:10.1002/qj.2432.
- Tripathi, O. P., A. Charlton-Perez, M. Sigmond, and F. Vitart, 2015b: Enhanced long-range forecast skill in boreal winter following stratospheric strong vortex conditions. *Environ. Res. Lett.*, **10**, 104007, doi:10.1088/1748-9326/10/10/104007.
- Tung, K. K. and R. S. Lindzen, 1979: A Theory of Stationary Long Waves. Part I: A Simple Theory of Blocking. *Mon. Wea. Rev.*, **107**, 714–734, doi:10.1175/1520-0493(1979)107<0714:ATOSLW>2.0.CO;2.
- van Loon, H., and K. Labitzke, 1987: The Southern Oscillation. Part V: The anomalies in the lower stratosphere of the Northern Hemisphere in winter and a comparison with the Quasi-Biennial Oscillation. *Mon. Wea. Rev.*, **115**, 357-369, doi:10.1175/1520-0493(1987)115<0357:TSOPVT>2.0.CO;2.
- Vitart, F., C. and Coauthors, 2017: The subseasonal to seasonal (S2S) prediction project database. *Bull. Amer. Meteor. Soc.*, **98**, 163–173, doi:10.1175/BAMS-D-16-0017.1.
- Wang, G., H. H. Hendon, J. M. Arblaster, E.-P. Lim, S. Abhik, and P. van Rensch, 2019: Compounding tropical and stratospheric forcing of the record low Antarctic sea-ice in 2016. *Nat. Commun.*, **10**, 13, doi:10.1038/s41467-018.

- Waugh, D. W., A.H. Sobel, and L.M. Polvani, 2017: What Is the Polar Vortex and How Does It Influence Weather?. *Bull. Amer. Meteor. Soc.*, **98**, 37–44, doi:10.1175/BAMS-D-15-00212.1
- Woo, S., M.-K. Sung, S.-W. Son, and J.-S. Kug, 2015: Connection between weak stratospheric vortex events and the Pacific Decadal Oscillation. *Climate Dyn.*, **45**, 3481–3492, doi:10.1007/s00382-015-2551-z.
- Yamazaki, Y., and Coauthors, 2020: September 2019 Antarctic sudden stratospheric warming: Quasi-6-day wave burst and ionospheric effects. *Geophys. Res. Lett.*, **47**, e2019GL086577, doi:10.1029/2019GL086577.

## 국문초록

본 연구에서는 남반구 및 북반구에서 발생한 성층권 돌연승온 사례가 엘니뇨 남방진동에 어떤 영향을 받는지 살펴보았다. 먼저 북반구 돌연승온의 경우 기존 연구와는 달리 엘니뇨 겨울철에만 돌연승온 발생빈도가 증가하는 것을 확인할 수 있었다. 기존 연구 결과는 특정 돌연승온 정의에 대해서만 라니냐 겨울철에도 돌연승온이 증가했기 때문인 것으로 확인되었다. 또한 라니냐 겨울철 시기의 돌연승온의 경우 정의에 대한 민감도뿐만 아니라 시기에 대해서도 민감함을 보였다. 특히, 약 20년 주기의 장기변동성을 보이는 등 돌연승온과 일관된 관계를 보이지 못하였다. 남반구 돌연승온은 역대 2번만 관측될 정도로 매우 드문 현상에 해당한다. 특히 2019년 9월 가장 강한 돌연승온이 확인되면서, 해당 돌연승온이 왜 발생했는지를 확인하고자 하였다. 계절내-계절 시간규모 예측 모형에서 성층권 초기장 및 해수면 온도를 바꿔 주어 주요 인자에 대해 논의하였다. 결과적으로 적도 태평양 해수면 온도(혹은 엘니뇨/남방진동)를 낮췄을 때 유의미한 돌연승온 예측성능 차이를 보였다. 추가적으로 북반구 돌연승온 사례 예측성능 검정을 통해 돌연승온 예측성능을 검정하고, 이러한 예측성능이 준2년주기진동 혹은 엘니뇨/남방진동 등 경년변동성에 영향을 받는지 확인하였다. 경년변동성 차이에 따른 유의미한 예측성능 차이는 확인할 수 없었으며, 이는 엘니뇨/남방진동 위상 차이는 돌연승온 발생에 영향을 주지만 예측성능에는 영향을 못 미쳤음을 시사한다.

주요어: 성층권 돌연승온, 엘니뇨/남방진동, 계절내-계절 예측성

학 번: 2016-30115

## 감사의 글

부산에서 학부를 마치고 서울로 올라온 지 어느덧 만 7년이 지났습니다. 제가 보내온 어느 학생 생활보다도 긴 학교생활이었는데, 무엇을 하고 보냈는지 모를 만큼 빠르게 지나버렸네요. 특히 박사학위 기간 동안은 참 길다고 느꼈는데, 지나고 나니 또 그렇게 길지 않았던 것 같기도 하고 그렇습니다.

졸업을 앞둔 이 시점에서 지난 7년은 어땠나 되돌아켜보니, 많다면 많은 일이 있었고 별거 아니라면 별거 아닌 일들의 연속이었던 것 같습니다. 가장 기억에 남는 순간들을 꺼내려고 보니, 그 기억들 속에는 항상 연구실 사람들 중 한명이 있었거나 지도 교수님의 지원이 있어야 가능했던 일이거나 둘 중 하나였네요. 그렇게 되돌아켜 보니, 학교에서 같이 지냈던 이들이 있었기 때문에 학위를 받을 수 있었던 것 같습니다. 그런 날들을 있게 해준 모든 분들에게 감사의 글을 남깁니다.

무엇보다 학위 받는 것에 있어 가장 큰 역할을 했다면, 역시 지도교수님이신 손석우 교수님을 가장 먼저 꼽고 싶습니다. 입학하고 싶다고 부산에서 올라온 저를 편견 없이 받아 주셨고, 하나도 모르던 저를 그래도 사람 구실 할 정도로 지도해주신 것만해도 대단한 일을 하셨다고 생각합니다. 특히, 학위 끝까지 마무리할 수 있게 이끌어 주신 것 감사합니다.

그리고 학위에 직접적인 도움을 주신 박사학위 심사위원 분들께도



감사인사 드리고 싶습니다. 먼저, 위원장이신 최우갑 교수님. 학위 과정에서 주신 연구적인 조언도 정말 많은 도움이 되었지만, 특히 연구외에도 교수님 수업에서 역학적인 지식을 많이 배울 수 있었습니다. 지도 교수님 다음으로 제 역학 지식의 기초를 쌓는데 많은 도움을 주신 분이라는 것만 알아주셨으면 좋겠습니다:)

그리고 위원으로 도움을 주신 김백민 교수님과 김주완 교수님께도 감사인사 드리려고 합니다. 학위 위원 이전부터, 언제든 흔쾌히 연구 조언을 해주셨고, 연구자가 갖춰야할 태도 등 제가 조금 더 나은 연구자가 될 수 있도록 진심 어린 조언을 해주셨습니다. 제가 매번 표현은 다 못했지만, 하나하나 다 기억하고 감사한 마음으로 간직하고 있습니다.

마지막으로 영국 저 멀리서 도움을 주신 Charlton-Perez 교수님께 감사인사 드립니다. 2016년 처음 워크샵에서 만난 이후로 한결 같은 모습으로 연구미팅 응해주신 것 뿐만 아니라, 바쁘신 와중에 영국 레딩에 방문 연구 과정에서 시간 내주신 것도 정말 감사드립니다. 특히, 제가 평소에 보지 못하는 다른 관점의 연구 방향을 지적해주신 것 항상 기억하고있습니다.

연구실 분들이 없었다면 박사학위도 없었지 않았을까 생각합니다. 연구실 초창기부터 지금까지 정말 많은 사람들과 함께했고, 모두가 다 기억에 남고 고마운 존재입니다. 특히, 시작을 함께한 분들이 정말 오래 기억에 남을 것 같아요. 이미 졸업한 유나누나부터 대학원 동기나 다름없는

명일, 혜진누나, 그리고 먼저 좋은 곳 찾아 떠난 영은이까지, 타지에 혼자 올라와 힘들었을지도 몰랐을 2014년을 이 분들 덕분에 따뜻하게 웃으면서 보낼 수 있었던 것 같습니다. 특히나, 연구실 동기인 명일누나랑 혜진누나는 그때부터 지금까지, 때로는 술친구처럼 든든한 지원자였고, 때로는 인생선배로써 제가 더 성숙할 수 있게 진짜 많이 도와줬었네요. 많이 고마워요! 그리고 옆자리 서연아. 듬직한 후배이면서 챙겨주게되는 동생이기도하고, 미안하면서도 고마워하는거 알지? 그리고 후배(?)이지만 형, 누나인 재영이형, 헤라누나, 창현이형, 지영누님, 그리고 진경누나. 그렇게 잘 챙겨준 선배는 아니었던 것 같아서 좀 죄송하네요. 그런데도 같이 연구실 잘 꾸려주셔서 감사합니다:) 직접적으로 연구실 생활을 같이하지 않았지만, 연구나 연구외적으로도 많은 도움 주셨던, 김준수 박사님, 최정 박사님, 노준우 박사님, 한지영 박사님 감사드립니다! 대학원 시작의 끝을 함께해주시고, GRIMs라는 모형을 접할 수 있게 도와주신 구명서 박사님께도 늘 감사하다는 인사 남깁니다.

그리고 짧다면 짧고 길다면 긴 시간 같이한 승윤이, 찬일이, 준석이. 쏘대 선배 밑에서 연구실 일 처리해준다고 고생 많았다. 친구인지 형인지도 모르게 많이 놀리기도 했는데, 다 잘 받아준 것도 고맙게 생각하고있어. 미국에 있을 준석이는 마지막 인사 제대로 못하고 가서 많이 아쉽네! 그리고 예준이, 현석이, 영주도 연구실 이런저런 일들 같이 처리해준 거 다 기억하고 있고, 그 부분 고맙게 생각하고있다는 것도 알아줬으면 해! 앞으로

들어오는 신입생 동찬이랑 예은이 잘 챙겨주고.

연구실 못지 않게 7년간 정말 친구처럼 옆에서 즐거운 추억 만들어주고, 지지해준 악꿏분들. 여러분들도 정말로 고맙습니다. 류지형, 희동이, 재연이형, 형오, 민규, 상욱이형, 심찬이 앞으로 계속 봐야지요. 글로 쓰지않아도 제 마음 잘 알거라 생각합니다:) 어디에 있든 항상 연결되어 있는 거 알죠?

그 외에도 서울 생활 적응하는데 여러 방면에서 도움을 주었던 대학원 선배님들 다들 감사드립니다. 대학원 올 수 있게 직접 도움주신, 영찬이형부터 대학원 적응하면서 친해진 아름누나, 서연누나, 지현누나 다들 고맙습니다. 그리고 궁금한 거 있을 때 거리낌 없이 대답해준 승언이형, 이제는 교수님 되신 이현호 교수님, 다른 방이지만 언제나 반갑게 인사해주신 의종이형, 우석이형, 훈영이형, 다솔이형, 진우형, 민희누나까지 평소 표현은 못해도 모두들 감사하게 생각하고있습니다. 그리고 같은 연구실 사용하면서 신세 한탄 많이 들어주신 채윤누나, 정화누나에게도 이 기회를 빌려서 감사인사 남깁니다. 그리고 다른 학교지만, 학위 시작과 끝을 같이한 강민지 박사님. 학위 축하드리고, 동지 한명 있어서 든든했다!

연고도 친구도 없는 부산에서 학창시절 추억 같이 만들어준 학부 선/후배에게도 늦게나마 감사인사 남깁니다. 주말에 허심청에서 인생 이야기하던 게 엇그제 같은데, 어느새 10년이 지났습니다. 혁햄, 재원햄, 성빈햄. 자주 안부전하는 그런 착한 후배는 아니지만, 늘 잊지않고 모두의

안녕을 바라고 있다는 것 잊지 않아주셨으면 좋겠어요:) 그리고, 돌아돌아 옆동네로 와서 학위 중인 소임이도 건강챙기면서 학위 마무리할 수 있었으면 좋겠다! 이제는 동생보다 친구 같은 혜정이랑 보름이, 한솔이, 도연이까지 학부때부터 지금까지 너희들 덕분에 좋은 경험하고 좋은 추억 쌓을 수 있었던 것 같다. 평소에 쑥쓰러워서 잘 이야기 못했지만, 이 기회에 고맙다는 인사 남겨.

인사말 남기는데 가족을 빼놓을 수 없을 것 같아요. 일찍 타지 생활을 시작하면서 인생의 절반 가량만 가족들이랑 한 지붕 아래서 보냈던 것 같네요. 송사장님, 윤여사님에게 자랑스러운 아들일 수도 있겠지만, 한편으로는 못난 아들일 수도 있겠다는 생각합니다. 공부한다고 오랜 기간 걱정 끼치고, 자기 맘대로 인생사는 이기적인 아들이기도 한데, 처음부터 끝까지 항상 지지해 주셔서 감사합니다. 앞으로 효도하면서 걱정안끼치는 그런 아들이 될 수 있을지 확신할 수 없지만, 남한테 피해 안주고 제 밥벌이는 할 수 있는 그런 아들은 되겠습니다. 그리고 친형인 강인이형. 언제 봐도 반가우면서 지겹고, 마음에 안들기도하고 들기도하고 묘한 관계이지만 그게 형인가봐. 아프지 말고 앞으로도 건강하고 싶은 것 하고 살길 바라!

모두 언급할 수 없겠지만, 친척들 꼭 언급하고 싶습니다. 30년 넘게 공부만 해서 맨날 받기만 하고, 마음 한번 제대로 표현하지 못했었는데, 결국 결실을 드디어 맺었습니다. 큰아버지, 큰어머니, 그리고 둘째큰아버지,

둘째큰어머니, 작은아버지랑, 작은어머니까지 언제나 예쁘게 봐주시고 공부하는 것 응원해주셔서 감사합니다. 그리고 친척 형, 누나들도 공부한다는 동생 끝까지 지지해줘서 고마워!

마지막으로 앞으로 제 남은 평생을 함께할 동반자 용진이에게 고맙다는 인사를 전하고 글 마무리하려고 합니다. 같이 지내온 기간 동안 많은 일이 있었고 공부한다고 고생도 많이 했는데, 그렇게 이야기하던 순간이 온 것 같네. 둘다 많이 고생했고, 앞으로 지난 날들보다 몇 배는 더 행복한 날들만 맞이했으면 좋겠다! 끝까지 옆에서 지지해주고, 서로의 버팀목이 될 수 있었던 건 서로에게 행운이 아니었을까 생각해. 앞으로 많이많이 행복하자!